VI WORKSHOP ON LIDAR MEASUREMENTS IN LATIN AMERICA

September 26th - October 1st

La Paz, Bolivia

ISSN - 1562 - 3823

REVISTA BOLIVIANA DE FISICA

NÚMERO 20s DIC. 2011 • LA PAZ - BOLIVIA

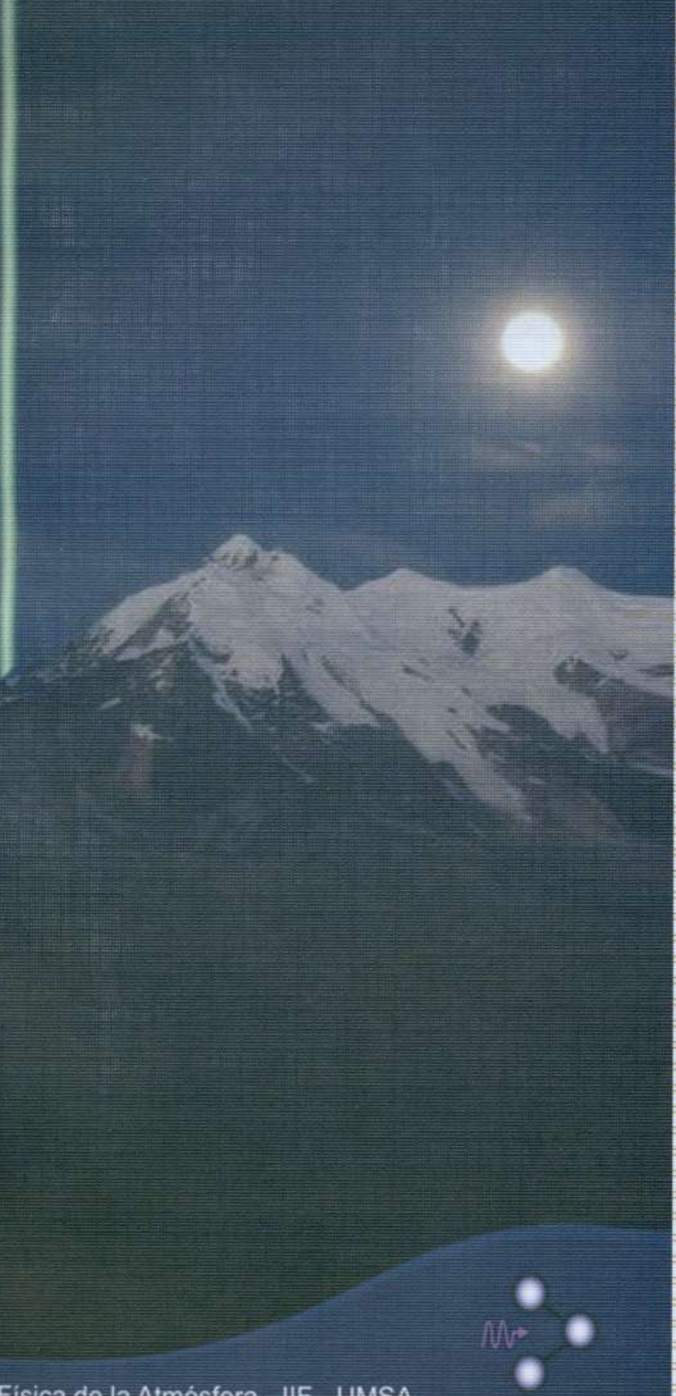

INSTITUTO DE INVESTIGACIONES FISICAS
SOCIEDAD BOLIVIANA DE FISICA
CARRERA DE FISICA - UMSA

Laboratorio de Física de la Atmósfera - IIF - UMSA

REVISTA BOLIVIANA DE FÍSICA
Ésta es una revista de la Unión Iberoamericana de Sociedades de Física

Casilla 8635, La Paz – Bolivia. Tel.: (591-2) 2792999, Fax: (591-2) 2792622

ORGANIZING COMMITTEES

Local Organizing Committee (LOC):

Francesco Zaratti (Chair),
Ricardo N. Forno (Co-chair),
Marcos F. Andrade, Luis A. Blacutt,
René Gutiérrez, Wilfredo Tavera,
Fernando Calderón, Fernando Velarde,
Fabricio Ávila, Juan Calle,
Leslie Fanola, Decker Guzman,
Oscar Lazcano, Valeria Mardoñez,
Marcelo Peñalosa, Manuel Roca,
Marcelo Vargas, Peter Zabala, Cristian Conitzer,
David Whiteman (GSFC-NASA, USA)

International Organizing Committee (IOC):

Eduardo Landulfo (Chair) IPEN, Brazil
Francesco Zaratti (Co-Chair) LFA-UMSA, Bolivia
Juan Carlos Antuña GOAC, Cuba
Errico Armandillo ESA-EU
Barclay Clemesha INPE, Brazil
Angel de Frutos U. de Valladolid, España
Gelsomina Pappalardo IMAA, Italia
Alan Robock Rudgers University, USA
Eduardo Quel CEILAP, Argentina
Alvaro Bastidas UNALMED, Colombia
Upendra Singh LaRC-NASA, USA
David N. Whiteman GSFC-NASA, USA

ISSN 1562-3823

Revista Boliviana de Física

Publicación de
INSTITUTO DE INVESTIGACIONES FÍSICAS
CARRERA DE FÍSICA
UNIVERSIDAD MAYOR DE SAN ANDRÉS
Y
SOCIEDAD BOLIVIANA DE FÍSICA

NÚMERO 20s
DICIEMBRE DE 2011

Revista Boliviana de Física

ISSN 1562-3823
Indexada en: SciELO, Latindex, Periódica
http://biblioweb.dgsca.unam.mx/latindex

Publicación del Instituto de Investigaciones Físicas, la Carrera de Física de la Universidad Mayor de San Andrés y de la Sociedad Boliviana de Física.
Casilla 8635, La Paz, Bolivia.

Diseño: A. Ticona
Dirección: Carrera de Física, Campus Universitario, Calle 27, Cota Cota, La Paz.
Tel: (591 2) 2792999; FAX: (591 2) 2792622.

Portada: Poster del “VI WORKSHOP ON LIDAR MEASUREMENTS IN LATIN AMERICA”

Formato LaTeX2ε. Tipo de fuente utilizada: newcentury

IMPRESO EN BOLIVIA — PRINTED IN BOLIVIA

CONTENIDO

I. PRESENTACIONES

CONTENIDO

II. POSTERS

REVISTA BOLIVIANA DE FÍSICA 20s, 1-3, 2011
ISSN 1562-3823. INDEXADA EN: SCIELO, LATINDEX, PERIÓDICA

One year of Cloud Optical Depth measurements with sunphotometer in Camagüey, Cuba.

Boris Barja(1), Yasmine Benouna(2), Carlos Toledano(2), Juan Carlos Antuña(1), Victoria Cachorro(2), Carlos Hernández(1), Ángel de Frutos(2) and René Estevan(1).
(1)Atmospheric Optics Group of Camagüey,
Carretera a Nuevitas km 7 ½ Camagüey, CUBA
Tel: +53 32262397, e-mail: bbarja@gmail.com
(2) Atmospheric Optics Group, University of Valladolid,
Valladolid, Spain

SUMMARY

One year of Cloud Optical Depth (COD) measurements obtained with the radiometer (sunphotometer Cimel CE – 318) are presented. As the first step a validation method is proposed in order to confirm the cloud in the measurement. This method is based in the cloud information derived from the actinometrical observations and radar data. In the second step of the work, the statistical results from the one year of the COD measurements in Camagüey are analyzed. The results show the high quality of COD measurements at Camagüey. The analysis of the COD frequency shows one peak close to 15. Similar behavior occurs each month. The mean COD average value for the entire period is 27.2, with a standard deviation of 17.3. The mean monthly minimum and maximum value of COD occur in December and May, respectively. The diurnal cycle of the mean hourly COD values shows an increase in the afternoon hours. In the afternoon the number of cases measured decrease. The preliminary results shown in this paper constitute the first report of such measurements in the country.

Key words: Cloud optical depth (COD), sunphotometer, Camagüey, Cuba.

INTRODUCTION

Clouds are a key point in the climatic system. They interact with the solar and terrestrial radiation and in turn are essential in the determination of the atmospheric radiation budget. The intensity of these processes is related with the optical and microphysical properties of the clouds. Thus, the study of the cloud optical properties is very important in order to understand their behavior and their climatic effect. These properties are identified by the optical depth (COD), singe scattering albedo (ω), and the asymmetric factor (g) of the cloud drops. Cloud optical depth (COD) is a fundamental value in the determination of the radiative energy balance in the Earth. Nevertheless, this property is very difficult to measure with ground remote sensing technique using the traditional methods. Better representation of the COD in the atmospheric general circulation and climatic models is a challenge in the atmospheric sciences. By those reasons it is necessary the increase of the COD measurement sites and the exactitude of the measurement.

There are two principal operational networks with the primary objective of the measurements of the cloud characteristics from the ground: the first one is of the Atmospheric Radiation Measurement Program (ARM) (Stokes and Schwartz, 1994), the second one is the network for measurement of clouds (Cloudnet) (Illingworth *et al.*, 2007). But the number of the measurement sites of these networks is limited in order to obtain ground based global scale measurements.

Aerosol Robotic Network (AERONET) is designed for the measurements of the optical and microphysical properties of the aerosols (Holben et al., 1998). AEROENT have more than 250 measurement sites over the world with sun radiometers that make sun direct irradiances and sky radiance measurements. When the cloud is in the instrument field of view the measurement is not useful for the aerosols properties determination. Then it is possible to set the sunphotometer to the 'cloud mode' (Chiu *et al.*, 2010), completing a set of the radiance measurements in the zenith to obtain COD values.

In the Atmospheric Optics Group of Camagüey (GOAC) a sunphotometer CIMEL CE-138 was installed. This instrument is part of the collaboration between the Atmospheric Optics Group (GOA) from Valladolid University, Spain and GOAC. Aerosols and clouds measurements with sunphotometer began in October 2008 and June 2010, respectively.

The objective of the present work is to evaluate in a first approach the strength of the COD measurements from the sunphotometer. The question to answer is: Does the COD sunphotometer measurement match the actinometric cloud reports? Reported cloud information in the hourly actinometric measurements is used in the validation algorithm. The second objective of the work is to obtain a preliminary COD statistics for non precipitating clouds during the first year of measurements at Camagüey.

INSTRUMENT AND METHODS

The data employed in the present work is from the sunphotometer Cimel CE-318 installed in Camagüey (21.42º N, 77.84º W, 128 m asl), Cuba. AERONET employed this radiometer for the measurement of sun direct irradiance and sky radiance with a field of view of 1.2º in the wavelengths of 340 nm, 380 nm, 440 nm, 675 nm 870 nm, y 1020 nm. (Holben *et al.* 1998).

When the cloud is in the instrument field of view the measurement is not useful for the aerosols properties determination. Chiu *et al.* (2010) proposed recently the use of these conditions to make 10 radiance measurements in the zenith in each wavelength, named 'cloud mode'. This is based in the suggestion of the use of two wavelength measurements in the red and near infrared spectrum to retrieve COD values over the vegetated surface (Chiu *et al.*, 2010).

The method for the COD determination employed in AERONET is explained in details by Chiu et al., (2010). Nevertheless some points are given here. There is no one to one relationship between zenith radiances and COD. So, two wavelengths radiance measurements (470 nm and 879 nm) are employed to reduce the ambiguity. With the radiance in these two wavelengths, some radiative transfer calculations, and satellite data the COD value is obtained (Chiu *et al.,* 2010). The reported COD value is the average of the 10 instantaneous values. The dataset used in the present study is from June 2010 to May 2011, with 2277 values.
An algorithm is proposed to 'evaluate' the COD measurements. This approach is intended to determine the 'correct' COD measurements. The evidences of this 'correctness' is obtained from the reports on clouds in the hourly actinometric observations.

The characteristics of the cloudiness used in the algorithm are: the solar disk state (SDS), covered sky fraction by cloud (SFT), covered sky fraction by low cloud types (SFL), atmospheric phenomena occurring at the time of observation (PHEN), cloud types present in the sky (CLDT), cloud types present in the zenith direction (CLDZ). The factors PHEN, CLDT, CLDZ and SDS are described in Table 1. Note that the actinometric measurements are made in the direction of the Sun and radiometric observations are in the zenith direction. The covered sky fractions are evaluated in base to 10 parts.

Table 1. Parameter codification for atmospheric phenomena (PHEN), cloud types (CLDT and CLDZ) and solar disk stateSDS.

PHEN	Description	CLDT	Description
0	Not present	0	Not present
1	Dew	1	Cumulus (Cu)
2	Haze	2	Stratocumulus (Sc)
3	Fog	3	Stratus (St)
4	Mist	4	Cumulonimbus (Cb)
5	Heavy shower	5	Altocumulus (Ac)
6	Rain	6	Altostratus (As)
7	Storm with precipitation	7	Nimbostratus (Ns)
8	Storm without precipitation	8	Cirrus (Ci)
9	Smoke	9	Cirrostratus (Cs)
		10	Cirrocumulus (Cc)

SDS	**Description**
0	clear solar disk
1	Solar disk can be seen through the cloud with clear defined outline
2	Solar disk can be seen through the cloud with unclear defined outline
3	Solar disk cannot be seen through the cloud
4	Solar disk is obstructed by an object

The steps of the algorithm are described below:

1. Evaluate the direct coincident actinometric report with COD measurement, by times difference (Δt) of 10 minutes.
2. If the first step is satisfied the cloudiness characteristics are evaluated.
    - 2.1. If SDS is different of 1, the sunphotometer can be decided to enter in the `cloud mode´. But it does not mean that there are clouds in the zenith. Thus it is necessary to evaluate the SFT, SDL, CLDT and CLDZ..
        - 2.1.1. For the SDS from 2 to 4.
            - 2.1.1.1. If SFT is between 1 and 3 and the COD measurement time is between 15:00 GMT and 19:00 GMT, the COD is selected as 'correct'.
            - 2.1.1.2. If SFT is between 4 and 10 and the SFL is equal to SFT, the COD is selected as 'correct'.
    - 2.2. Always the COD values are compared with CLDT and CLDZ to evaluate the correspondence of the value.
3. If the first step is not satisfied, it is necessary to compare cloudiness characteristics from the actinometric observations before and after the COD measurement time.
    - 3.1. If the cloudiness characteristics indicative of the presence of cloud (CLDT>5, CLDZ>0, SFL>4, PHEN>4) are similar in both actinometric observations, the COD is selected as 'correct'.
    - 3.2. CLDT and CLDZ are compared in both actinometric observations to evaluate the COD value with the limits shown in the point 2.2.

A set of COD values is obtained with the COD selected as 'correct'. The features of the COD true values are analyzed for the complete period from June 2010 to May 2011, as well as in monthly and hourly basis.

RESULTS AND DISCUSIONS

The set of original COD measurements in the period consists of 2277 values. After applying the 'evaluation' algorithm 2250 COD values are selected as 'correct', representing the 98.8 % of the cases. Only 25 cases were rejected and 2 cases can not be compared because the actinometric measurements were not conducted. The rejected cases were related with low values of COD and the absence of cloud in the zenith. It can be seen the agreement between the sunphotometer COD measurements and the actinometric reports of clouds.

The extreme values of COD, values lower than 3 and higher than 90, are discarded from the dataset, following the criteria of Chiu *et al.,* (2010). A total 1797 COD values are selected after the application of this criteria, representing a 79.9 % of the 'correct' values. This dataset is used for the statistical analysis. The mean value of COD is 27.2, with a standard deviation of 17.3.

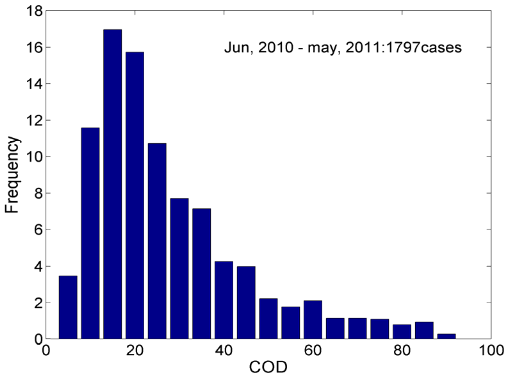

Figure 1. COD frequency distribution for the period from June 2010 to May 2011, in Camagüey

In the Figure 1 the COD frequency distribution is shown with an interval of 5 units of COD. The maximum frequency of 17 % is found in the interval centered at 15. The COD frequency values increase from COD value 3 to the maximum in 15 and then the values decrease for higher values of COD. This result shows a similar frequency distribution than the report from Chiu *et al.,* (2010) for three years of data from November, 2004 to June, 2008 at the ARM measurement site of Oklahoma in the United States of America. The authors show for Oklahoma maximum frequency of 24 % at COD value near to 23. Also, they show the increase of the frequency from minimum values of COD to 23 and then the frequency values decrease for higher values of COD (Chiu *et al.,* 2010). The results for Camagüey and Oklahoma sites show similar behavior of the COD, with different magnitude values. The data sets for both sites have some differences, based in the extent of the datasets and different geographical location.

Figure 2 shows the behavior of the monthly mean of COD values and the number of cases in each month for the measurement period. The COD monthly mean maximum value of 34.2 is in the month of May, 2011. The minimum value of COD of 19.8 is in December, 2010. The number of cases reaches their maximum of 274 and minimum of 99 in October, 2010 and February, 2011, respectively. This result shows May with the maximum monthly mean value

The mean COD daily behavior is shown in the Figure 3. The COD hourly mean values increase with the hour during the day. Maximum value of COD hourly mean value is 34.2 at the 22 GMT; the minimum value of 17.2 is at 13 GMT. This result is in relation with the development of the cloudiness during the day. The number of cases has a maximum of 282 at 18 GMT. In the first and last hour there are the minimum values of number of cases. At these times in some months of the year there are no measurements with the sunphotometer.

CONCLUSIONS

This is the first report on cloud optical depth ground measured in our country. The COD frequency distribution shows a maximum at the interval centered in 15. The frequency distribution of COD agrees with other reports. There is a monthly COD maximum of 34.2 in May. Nevertheless, the maximum value of the number of cases occurs in October. Monthly and hourly mean values of COD show the concordance with the natural behavior of the clouds in our region.

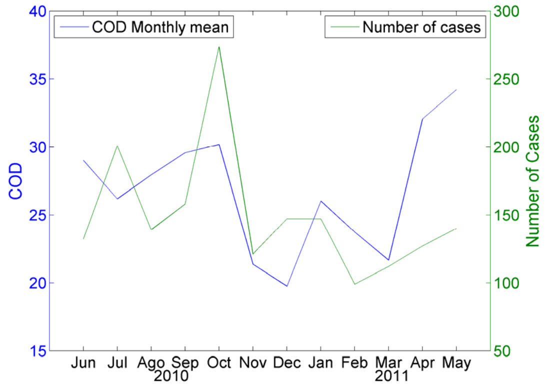

Figure 2. COD Monthly means for the period from June 2010 to May 2011.

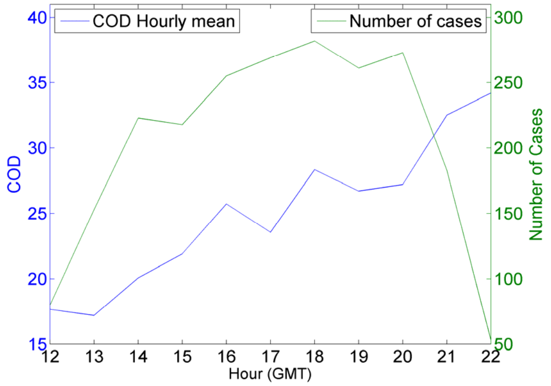

Figure 3. COD Hourly means for the period from June 2010 to May 2011.

REFERENCES

Chiu, J. C., C. - H. Huang, A. Marshak, I. Slutsker, D. M. Giles, B. N. Holben, Y. Knyazikhin, and W. J. Wiscombe (2010), Cloud optical depth retrievals from the Aerosol Robotic Network (AERONET) cloud mode observations, *J. Geophys. Res.*, **115**, D14202, doi:10.1029/2009JD013121.

Holben, B. N., Eck, T. F., Slutsker, I., Tanré, D., Buis, J. P., Setzer, A., Vermote, E. F., Reagan, J. A., Kaufman, Y. J., Nakajima, T., Lavenu, F., Jankowiak, I., and Smirnov, A. (1998), AERONET: A federated instrument network and data archive for aerosol characterization, *Remote Sens. Environ*., **66**, 1–16.

Illingworth, A. J., et al. (2007), Cloudnet: Continuous evaluation of cloud profiles in seven operational models using ground-based observations, Bull. Am. Meteorol. Soc., 88, 883–898.

Stokes, G. M., and S. E. Schwartz (1994), The Atmospheric Radiation Measurement (ARM) Program: Programmatic background and design of the cloud and radiation test bed, *Bull. Am. Meteorol. Soc*., 75, 1201–1221.

REVISTA BOLIVIANA DE FÍSICA 20s, 4-6, 2011
ISSN 1562-3823. INDEXADA EN: SCIELO, LATINDEX, PERIÓDICA

Optimized data-gluing method for mixed analog/photon-counting lidar signals

Diego Lange(1,2), Dhiraj Kumar(1,2), Francesc Rocadenbosch(1,2), Michaël Sicard(1,2), Adolfo Comerón(1)
(1)Remote Sensing Laboratory (RSLab), Dept. of Signal Theory and Communications (TSC), Universitat Politècnica de Catalunya (UPC), Barcelona, Spain.
(2)Institut d'Estudis Espacials de Catalunya (IEEC) - Centre de Recerca de l'Aeronàutica i de l'Espai (CRAE), Universitat Politècnica de Catalunya (UPC), Barcelona, Spain.
Tel: (+34)934016849, Fax: (+34)934017200, E-mail: roca@tsc.upc.edu

SUMMARY

In atmospheric LIDAR (Light Detection and Ranging) remote sensing, the dynamic range of the return power signals can span up to five orders of magnitude. Modern acquisition systems such as those based on Licel^{TM} transient recorders combine a dual acquisition mode in which the return signal is recorded simultaneously in both analog (analog-to-digital (AD) conversion) and photon-counting (PC) modes. Although both data records can be analyzed separately, their combination obtained through gluing gives the advantage of the high linearity of the AD conversion for high light-level signals (especially in the near range) and the high sensitivity of the PC mode for low light-level signals (in the far range).

Recently, eruptions of volcanoes such as Eyjafjalla (Iceland) in 2010, Grímsvötn (Iceland Puyehue (Argentina) Nabro (Eritrea) and Mount Lokon (Indonesia) in 2011 have yielded emergency situations with a strong economical cost due to human evacuation and/or air traffic interruption. Volcanic aerosols are first injected in the troposphere and often reach the stratosphere where they can reside for several years. The mixed analog/photo-counting acquisition approach is particularly suitable for the detection of volcanic aerosols in both the troposphere (near/mid range) and the stratosphere (far range).

In this line, a case study showing volcanic aerosols from the Nabro volcano (Eritrea, 2011) in the stratosphere and simultaneously Saharan dust in the troposphere over the multi-spectral Barcelona lidar station during the period 27 June – 1 July 2011 is presented. The benefits of the proposed gluing technique will be shown through the comparison of analog, PC, and glued backscatter-coefficient time series.

Existing gluing algorithms solve the fitting coefficients by matching both analog and PC data over a predefined spatial range (or equivalently, over a predefined upper and lower counting rate) depending on which kind of photodetector (usually a photomultiplier) is being used. In this work, an enhanced data-gluing formulation is presented. The method automatically finds the spatial range where both analog and PC signals are more similar based on Euclidian distance minimization over piece-wise range intervals along the whole acquisition spatial range.

Key words: Lidar, volcanic eruptions, tropospheric and stratospheric aerosols, gluing.

1. INTRODUCTION

Today, an important research line in the field of signal processing of atmospheric-lidar signals is the pre-processing and multi-spectral inversion of atmospheric elastic/Raman signals, and in co-operation with passive sensors (WMO GAW, 2007; Ansmann et al., 1992). Key data products range from simple range-corrected atmospheric quick-looks to the retrieval of aerosol microphysical parameters (Böckmann, 2001).

In Europe, EARLINET is the ground-based atmospheric lidar observation network at continental scale (Matthias et al., 2004; Böckmann et al., 2004; Pappalardo et al., 2004). In the RSLAB (Remote Sensing Laboratory), an important effort within EARLINET has been the development of a scanning 2+1 elastic/Raman lidar system (1997-2007) and the ongoing development of the 3+2+1 multi-spectral (UV-VIS-NIR) lidar system since 2003 (Kumar et al., 2006). The acquisition system in reception is based on Licel^{TM} TR40-80 transient recorders, which provide simultaneous analog/PC acquisition of lidar signals by combining a 40-Msps, 12-bit ADC with a 250-MHz photon counter. Licel transient recorders have a parallel analog and PC detection chain. The combination (i.e., gluing) of both analog and PC signals gives the high linearity of the analog signal for strong signals and the high sensitivity of the photon counting for weak optical signals (Licel, 2007). Thus, the dynamic range of clean-data glued lidar signals can reach up to 5 orders of magnitude. To glue both signals, the PC channel must also be dead-time corrected (Whiteman, 2003; Hamamatsu, 1998).

2. ENHANCED GLUING ALGORITHM

The basic gluing algorithm proposed by Licel^{TM} (2007) combines analog- and PC-recorded signals in a *fixed* fitting range interval $[R_A, R_B]$, where both analog and PC signals are valid and have a high signal to noise ratio. Licel's gluing algorithm minimizes the error norm between the dead-time-corrected photon-counted (PC) signal, $\overrightarrow{V_{pc}}$, and a scaled and offset version of the analog signal, $\overrightarrow{V_a}$, for the solving parameters *a* (scaling) and *b* (offset) in the fitting interval $[R_A, R_B]$. That is,

$$\min\left\{\left\|\varepsilon_I\right\|^2\right\}_{a,b} = \min\left\{\left\|\overrightarrow{V_{pc}} - \left(a\overrightarrow{V_a} + b\right)\right\|^2\right\}_{a,b} \quad I \in \left[R_A, R_B\right], \quad (1)$$

where the error vector is defined as

$$\overrightarrow{\varepsilon_I} = \overrightarrow{V_{pc}} - \left(a\overrightarrow{V_a} + b\right), \quad (2)$$

with $\overrightarrow{V'_a} = a\overrightarrow{V_a} + b$, the scaled-and-offset analog signal.

For a typical mini-PMT the fitting interval corresponds to the range interval where the PC signal is in the 0.5-to-10-MHz region. In Eq.(1) the residual error norm $\left\|\overrightarrow{\varepsilon_I}\right\|^2$ is an indicator of the quality of the fitting. Besides, $\left\|a\overrightarrow{V_a}\right\| >> b$ so that the scaling parameter a is the dominant parameter in the residual.

The enhanced gluing method proposes a fine-tuning automatic-search algorithm to find the best fitting range interval I ensuring minimum residual error norm. Towards this goal a two-step procedure is followed:

1) First, the central point of the best fitting range interval, I_i, is obtained. To do that, the modified form of Eq.(1) above,

$$\min\left\{\left\|\overrightarrow{\varepsilon_{I_i}}\right\|^2\right\}_{a_i,b_i} = \min\left\{\left\|\overrightarrow{V_{pc}} - \left(a_i\overrightarrow{V_a} + b_i\right)\right\|^2\right\}_{a_i,b_i} \quad in\ I_i \quad (3)$$

is solved for $\overrightarrow{x_i} = \left(a_i, b_i\right) \leftrightarrow I_i$ along successive adjacent fitting range intervals $I_i \in \left(R_A^i, R_B^i\right)$ of constant length (ΔR = 100m) centered at the range R_i. In practice, R_i is incremented in steps of ΔR along the measurement range. When the scaling parameter a_i is plotted as function of the central range of the fitting interval, R_i, a parabolic behaviour is obtained. The parabolic behaviour of the error norm is in accordance with the foundations of maximum-likelihood classical estimation methods (Barlow, 1989). The minimum of the parabola, yields the sough-after central point, R_{opt}, of the best fitting interval along the measurement range.

2) Once R_{opt} has been determined, the end points of the best fitting range interval, R_A^{opt} and R_B^{opt} (i.e., left and right to the central point R_{opt}) are computed from the intercept points between the error parabola and a threshold level 1% above the minimum of the parabola (i.e., $a_\gamma = 1.01 a_{opt}$, in Fig. 2). The 1% criterion has been determined by experiment and yields a typical fitting length, $R_B^{opt} - R_A^{opt}$, of about 1.5 km, which is approximately the same fitting length as in the basic gluing algorithm of Eq.(1).

Because $\left\|a_i\overrightarrow{V_a}\right\| >> b_i$ also holds for Eq. (3), the error norm, $\left\|\overrightarrow{\varepsilon_{I_{opt}}}\right\|^2$ is also minimum when so is the scaling parameter a_i, thus guaranteeing an optimal fitting.

3. CONCLUDING RESULTS

Saharan dust intrusion episodes are frequent in the Iberian Peninsula (Pérez et al., 2006) and occur at low-troposphere heights. Because of the high intensity of the lidar returns in the near-range range, these dust episodes are nicely recorded by the analog channel and poorly recorded by the PC channel, which saturates due to the large number of counts in the near-range. The opposite situation occurs when monitoring volcanic eruptions (Guerrero et al., 2010), which inject volcanic aerosols up in the stratosphere. At such heights, the lidar returns are too faint to be properly recorded within the sensitivity of the analog channel (only a few ADC levels are "moved" and with a very poor signal-to-noise ratio (SNR)).

In Fig, 1, the analog signal is very noisy at the high range around 17 km so that volcanic aerosols cannot be distinguished from noise. PC signal fails to display aerosol layers below about 3 km. In contrast, the glued quick look of Fig. 2 and Fig. 3 evidences with a good signal-to-noise ratio both Saharan dust layers in the 0-4 km subplot (low range) and volcanic aerosols in the 15-18 km subplot (high range).

4. ACKNOWLEDGMENTS

This work was supported by the European Union under the project ACTRIS (Aerosols, clouds, and Trace gases Research Infrastructure Network) ref. nº FP7- INFRA-2010-1.1.16, the European Space Agency under the project 21487/08/NL/HE, the Spanish Ministry of Science and Innovation (MICINN) and FEDER (European Regional Development) funds under the project TEC2009-09106 and Complementary Actions CGL2009-08031-E/CLI ("Charmex") and CGL2008-01330-E/CLI.

MAEC – AECID (Spanish Ministry of Foreign Affairs and Cooperation) and Generalitat Catalunya/AGAUR are respectively thanked for Mr. D. Lange's and Mr. D. Kumar's pre-doctoral fellowships.

5. REFERENCES

Ansmann A., Wandinger U., Riebesell M., Weitkamp C., and Michaelis W., "Independent measurement of extinction and backscatter profiles in cirrus clouds by using a combined Raman elastic-backscatter lidar," *App. Opt.* **31**(33), 7113-7131 (1992).

Barlow R. J., "Estimation," in Statistics: A Guide To The Use Of Statistical Methods In The Physical Sciences (eds. F. Mandl, R. J. Ellison, and D. J. Sandiford) (Wiley, Chichester, England), Chap. 5, pp. 68-96 (1989).

Böckmann C., "Hybrid regularization method for the ill-posed inversion of multiwavelength lidar data in the retrieval of aerosol size distributions," *App. Opt.*, **40**(9), 1329–1342 (2001).

Böckmann C., Wandinger U., Ansmann A., Bösenberg J., Amiridis V., Boselli A., Delaval A., De Tomasi F., Frioud M., Hågård A., Horvat M., Iarlori M., Komguem L., Kreipl S., Larchevêque G., Matthias V., Papayannis A., Pappalardo G., Rocadenbosch F., Rodriguez J.A., Schneider J., Shcherbakov V., Wiegner M., "Aerosol lidar intercomparison in the framework of EARLINET. 2. Aerosol backscatter algorithms", *App. Opt.,* **43**(4), 977-989 (2004).

Guerrero-Rascado J. L., Sicard M., Molero F., Navas-Guzmán F., Preißler J., Kumar D., Bravo-Aranda J. A., Tomás S., Reba M. N., Alados-Arboledas L., Comerón A., Pujadas M., Rocadenbosch F., Wagner F., and Silva A. M., "Monitoring of the Eyjafjalla Volcanic Plume at Four Lidar Stations over the Iberian Peninsula: 6 to 8 May

2010", *IV Reunión Española de Ciencia y Tecnología del aerosol* – RECTA 2010, C15/1-C15/6.

Hamamatsu Photonics, "Photon Counting Using Photomultiplier Tubes," *AN-TPHO9001E02* (Japan, May. 1998).

Kumar D., Sicard M., Tomás S., Muñoz C., Rocadenbosch F., Comerón A., 2006, "Engineering of a water-vapor, Raman, elastic-backscatter lidar at the Technical University of Catalonia (Spain)" in *Proc. SPIE Europe Remote Sensing*, Vol. 6367 SPIE, Sweden, p. 63670U-1/12.

Licel GmbH, "Analysis Example: Gluing Analog and Photon Counting Data", Sect. 9.4 in "Licel Ethernet Controller – Installation and Reference Manual", Oct. 14, (2007).

Matthias V., Bösenberg J., Freudenthaler V., Amodeo A., Balis D., Chaikovsky A., Chourdakis G., Comeron A., Delaval A., De Tomasi F., Eixmann R., Hågård A., Komguem L., Kreipl S., Matthey R., Mattis I., Rizi V., Rodriguez J.A., Simeonov V., Wang X., "Aerosol lidar inter-comparison in the framework of the EARLINET project. 1 – Instruments", *App. Opt.,* **43**(4), 961-976 (2004).

Pappalardo G., Amodeo A., Pandolfi M., Wandinger U., Ansmann A., Bosenberg J., Matthias V., Amiridis V., De Tomasi F., Frioud M., Iarlori M., Komguem L., Papayannis A., Rocadenbosch F., Wang X., "Aerosol lidar intercomparison in the framework of the EARLINET project. 3 - Raman lidar algorithm for aerosol extinction, backscatter and lidar ratio", *App. Opt.,* **43**(28), 5370-5385 (2004).

Pérez C., Nickovic S., Baldasano J. M., Sicard M., Rocadenbosch F., and Cachorro V. E., "A long Saharan dust event over the western Mediterranean: Lidar, Sun photometer observations, and regional dust modeling", *Journal of Geophysical Research*, Vol. 111, D15214 (1-16) (2006).

Whiteman N. David, "Examination of the traditional Raman lidar technique I. Evaluating the temperature dependent lidar equations", *App. Opt.* **42**(15), 2571-2592 (2003).

WMO GAW, 2007, Plan for the implementation of the GAW Aerosol Lidar Observation Network (GALION) (Hamburg, Germany, 27-29 March 2007) (*WMO TD nº 1443*).

6. FIGURES

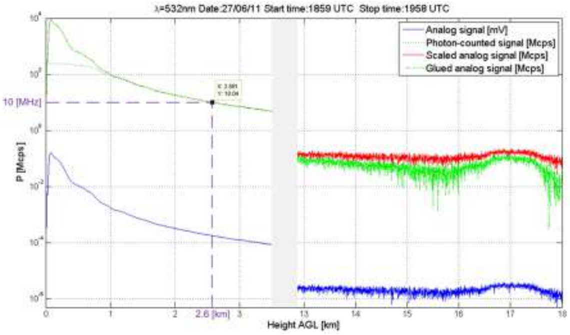

Figure 1. Comparison among analog, PC, and glued signals. (Blue) Analog raw signal, $\overrightarrow{V_a}$. (Red) Scaled-and-offset analog signal, $\overrightarrow{V_a'} = a\overrightarrow{V_a} + b$. (Black dotted) PC signal. (Green) Glued analog-PC signal. Note that below 2.6km (corresponding to a 10-MHz count in the PC channel) the glued signal follows the analog signal while above this range it follows the PC signal.

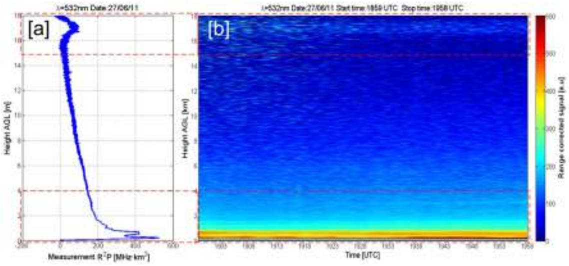

Figure 2. Time series monitoring the evolution of a vertical profile of volcanic aerosols in the stratosphere (about 17km) and several Saharan dust layers in the troposphere (below 3.5km), 532nm channel. (a) Range-corrected profile for the glued signal. (b) Glued signal time series.

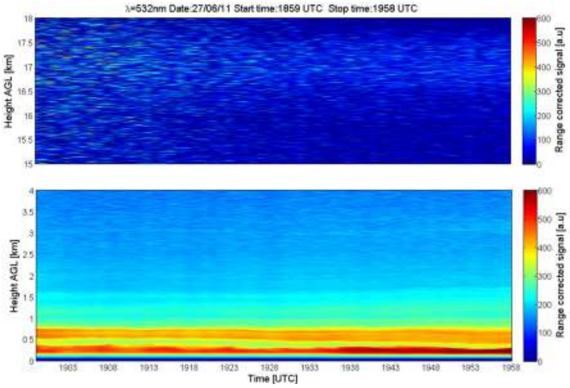

Figure 3. Glued signals zoomed in the low range (0-4 km) and in the far range (15-18 km).

REVISTA BOLIVIANA DE FÍSICA 20s, 7-9, 2011
ISSN 1562-3823. INDEXADA EN: SCIELO, LATINDEX, PERIÓDICA

Construcción de un Lidar Monoestático coaxial de retrodispersión elástica en México para el monitoreo ambiental.

Reynoso Lara E., Dávila Pintle J.A., Nanco Hernández P., Rendón Marín M.
Fac. de Cs. De la Electrónica, Benemérita Universidad Autónoma de Puebla, México.
E-mail: ereynoso@ece.buap.mx
Serrano Muñoz G., Ramírez Ramírz G., Lima Coyotecatl E.
Fac. de Cs. de la Electrónica, Benemérita Universidad Autónoma de Puebla, México.

RESUMEN

La contaminación atmosférica es un problema delicado de importancia a nivel mundial, especialmente en México D.F. y sus principales metrópolis. Actualmente, factores tales como sobrepoblación, industrias, medios de transporte, quema de combustibles la han incrementado de manera alarmante, provocando una gran concentración de gases invernadero (dióxido de carbono, metano, óxido nitroso y clorofluorocarbonos) en la atmósfera, de tal manera que se han creado planes de contingencia ambiental; como un ejemplo el programa de hoy no circulan automóviles cuyas placas tengan una particular terminación numérica. Debido a esto se ha tenido la necesidad de un constante monitoreo de la calidad del aire de diferentes ciudades. Lamentablemente en México no se ha desarrollado y/o explotado técnicas de monitoreo a través de luz, en especial de luz laser *(Lidar)*. En este trabajo se muestran las características principales de la construcción de un Lidar de retrodispersión elástica, con una fuente Laser pulsada de Nd:YAG en 1064 y 532nm. El rango de repetición de los pulsos es de 1-10 Hz con energías de 100 a 350mJ y duraciones de hasta 20ns en el modo de operación de Q-conmutada. El sistema de recolección de energía es un telescopio Newtoniano con una longitud focal de 121cm y un espejo primario de 20cm. El telescopio está montado sobre una base Dobsoniana que le permite girar en el plano horizontal (azimut) y en el plano vertical (zenit) para cambiar de altitud. El detector es un fotomultiplicador de la marca Hamamatsu con un rango espectral que va desde 400 a 1200nm. Para evitar el fenómeno de la compresión; es decir, regiones en donde no hay un perfecto traslape de las áreas del campo de visión del telescopio y la del haz laser, se decidió construir una configuración monoestática coaxial.

Key words: Dispersión elástica, monoestático coaxial.

INTRODUCTION

La contaminación atmosférica es un problema delicado de importancia a nivel mundial. Actualmente, factores tales como sobrepoblación, industrias, medios de transporte, quema de combustibles, etcétera; la han incrementado de manera alarmante, provocando una gran concentración de gases invernadero (dióxido de carbono, metano, óxido nitroso y clorofluorocarbonos) en la atmósfera, propiciando que los rayos solares queden atrapados en ella y de esta forma se produzca el calentamiento global.

Por otra parte, otro factor que afecta en gran medida a nuestro planeta es la acumulación de aerosoles en la atmósfera debido a que absorben o dispersan la radiación solar y evitan que ésta alcance la superficie terrestre generando el enfriamiento de la Tierra, que a su vez reduce la evaporación de la humedad de los suelos e incrementa la producción de nubes que persisten durante más tiempo sin producir lluvias.

Ante esta problemática, se han desarrollado diferentes métodos de monitoreo ambiental como son los convencionales que involucran la recolección de muestras de partículas suspendidas en la atmósfera para su análisis consecutivo en laboratorios ó métodos espectroscópicos de percepción remota que utilizan procedimientos ópticos para identificar las absorciones de las moléculas en varios rangos del espectro electromagnético con la finalidad de tener un control para evitar los constantes cambios que sufre la Tierra.

Uno de los métodos de interés más novedosos y efectivos para el monitoreo ambiental es la implementación de las técnicas LIDAR [1] que se utiliza principalmente para calcular: Perfiles de temperatura, humedad, presión, densidad de elementos, velocidades, etc. [2-5].

De acuerdo a su estudio y análisis la técnica LIDAR ofrece grandes beneficios en cuanto al monitoreo de la concentración de gases, aerosoles, átomos metálicos e iones en las diferentes capas de la atmósfera así como también a la determinación de los parámetros atmosféricos mencionados anteriormente gracias a su alta resolución espacial y temporal; además, detecta y proporciona información precisa acerca de la formación de fenómenos meteorológicos (huracanes, erupciones volcánicas, incendios forestales, etc.) ocasionados por aerosoles, a si mismo es aplicable en investigaciones oceánicas y militares.

En este trabajo se presenta un resumen de los criterios y detalles teórico-técnicos para el desarrollo de un sistema Lidar de retrodispersión elástica, monoestático coaxial.

DISEÑO DEL SISTEMA

Un sistema Lidar se puede implementar con dos tipos de configuraciones: La Biestática y la Monoestática. Consecuentemente, la configuración Monoestática se subdivide en dos categorías: arreglo Coaxial y arreglo Biaxial. La configuración empleada en este sistema es la monoestática coaxial debido a que esta configuración permite que el transmisor y el receptor tengan el mismo eje óptico.

En la Configuración Monoestática tanto el receptor como el transmisor se encuentran alineados en el mismo lugar, de manera que formen un solo arreglo. La determinación precisa del rango se establece por fuentes de luz pulsadas en el orden de nanosegundos. En un arreglo Coaxial el eje del haz laser coincide con el eje óptico del receptor. La función resultante de la combinación de estos efectos geométricos es llamada función de traslape del campo visual del receptor con el haz del láser.

El sistema Lidar en general se puede subdividir en tres subsistemas: Transmisor, Receptor y etapa de Detección y/o grabado. La fuente del Transmisor es un láser pulsado Nd:YAG con su línea fundamental 1064nm y con un cristal KTP de forma externa estamos generado su segunda armónica (Second Harmonic Generation, SHG) en 532 nm, la razón de repetición de los pulsos es del orden de 1-10 Hz con 350 mJ de energía por pulso en el modo de Q-conmutada y una duración de 15ns. El laser de Nd:YAG tiene dos formas de funcionamiento el de corrida libre y Q-conmutada, de estas dos formas se pueden obtener pulsos de diferente duración, lo cual es importante para el tamaño de la capa (bin range) de la atmósfera a monitorear. Las Figuras 1, 2 y 3 muestran la caracterización de los anchos de pulso en los diferentes tipos de funcionamiento y con distinta longitud de onda.

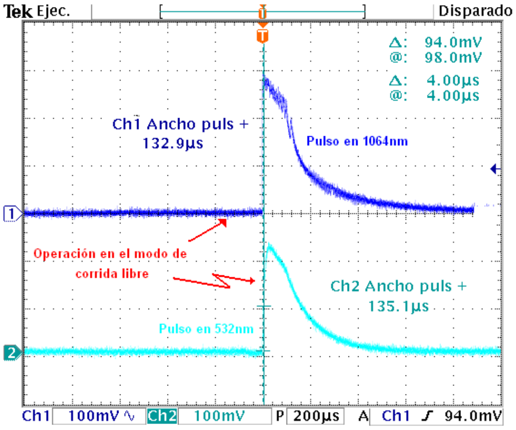

Figura 1. Características de los pulsos en 1064 y 532nm en el modo de corrida libre.

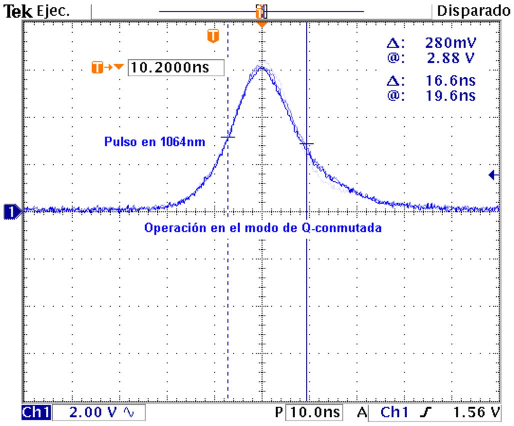

Figura 2. Características de los pulsos en 1064nm en el modo de Q-conmutada.

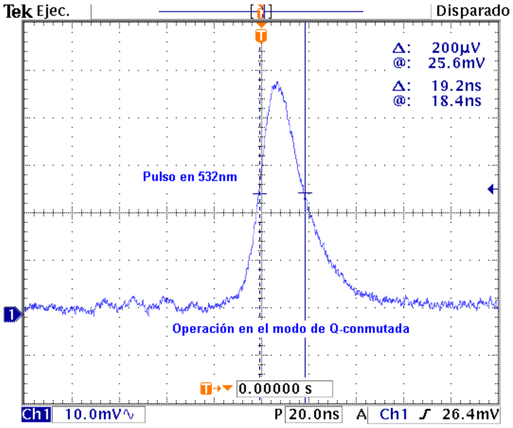

Figura 3. Características de los pulsos en 532nm en el modo de Q-conmutada.

El Receptor tendrá la función de colectar la mayor cantidad de luz retrodispersada por el elemento a monitorear, por lo tanto es común utilizar un telescopio.

En el sistema Lidar implementado se colocó un telescopio reflector Newtoniano de 20cm de diámetro y con un radio de curvatura de su espejo primario de 242cm, por lo tanto tenemos una longitud focal de 121cm y una razón focal de 6.05 la cual nos permitirá colectar la mayor cantidad de luz en un área bastante pequeña adecuada para el área efectiva del detector.

El telescopio está sobre una montura Dobsoniana (altitud-azimut ó altazimutal) que permite girar al telescopio en el plano horizontal (azimut) y en el plano vertical (zenit) para cambiar de altitud. Se decidió una montura Dobson por su sencillez en la implementación, portabilidad y firmeza que ofrece al hacer recorridas del cielo.

El tubo va montado sobre dos rodillos que descansan en dos baleros, que no sólo sirven para mover el telescopio sino también regulan la tensión del eje de altura.

El telescopio cuenta con un subsistema denominado periscopio, que es un instrumento para la observación desde una posición oculta. En su forma sencilla es un tubo con un juego de espejos en los extremos, paralelos y en un ángulo de 45° respecto a la línea que los une.

La función que realiza el periscopio dentro del sistema Lidar es transmitir el haz láser en un mismo eje mediante el arreglo de espejos dentro de las dos áreas (transmisor y receptor), es decir, que se transmita coaxialmente a través del telescopio, por lo tanto para nuestro sistema Lidar utilizamos la configuración monoestática coaxial. Ver Figura 4.

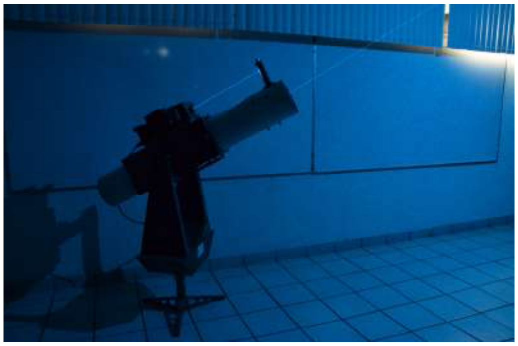

Figura 4. Sistema Lidar monoestático coaxial de retrodispersión elástica.

SIMULACIÓN DEL PROCESO DE TRASLAPE DE AREAS DE LOS CAMPOS DE VISIÓN DEL HAZ LASER Y RECEPTOR.

Esta parte de la simulación tiene por objetivo demostrar el proceso que existe en el traslape de áreas del campo de visión tanto del transmisor (línea azul) como del receptor (línea roja) al variar la separación entre los dos ejes de acuerdo a un rango específico.

El factor de geometría *se define como:*

$$G(R) = \frac{O(R)}{R^2} \qquad (1)$$

esta ecuación incluye la función de traslape $O(R)$, entre el haz del laser y el campo de visión del receptor y el término cuadrático R^{-2} que decrece rápidamente la intensidad de la señal con respecto a la distancia; esto es debido al hecho de que el área del telescopio del receptor forma parte de la superficie de una esfera de radio R que encierra el volumen de dispersión.

Las gráficas de la figura 5 ilustran la simulación numérica dicho proceso de traslape de áreas, tomando en cuenta los valores reales de la divergencia del haz laser y el campo de visión del telescopio receptor.

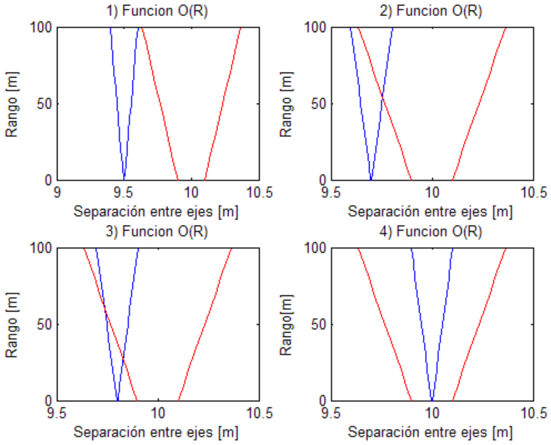

Figura 5. Proceso de Traslape de los campos de visión del telescopio y la divergencia del haz laser, en la gráfica 1) existe una separación de 50 cm entre los dos ejes, la gráfica, en 2) de 30 cm, en 3) de 20 cm, y en 4) el traslape se da desde el origen.

De acuerdo a las gráficas **1), 2) y 3)** de la figura anterior podemos observar que la configuración utilizada es la ***Monoestática Biaxial***. En donde el transmisor se coloca adyacentemente al receptor alcanzando el traslape máximo a diferentes alturas dentro de un rango establecido. Por ejemplo de acuerdo a la figura 5, en la gráfica 1) el traslape inicia a una altura (rango) de 100 m, en la gráfica 2) en 54 m, en 3) en una altura de aproximadamente de 26.5 m y el rango entre el cuál se realiza el monitoreo es de 0 - 100 m.

Finalmente la gráfica **4)** nos muestra la configuración ***Monoestática Coaxial*** en la cual tanto el transmisor y el receptor salen en un mismo eje y el traslape es desde el origen, lo cual beneficia en gran parte a nuestro sistema y a la simulación ya que mediante esta configuración, la función de traslape $O(R)$ vale uno desde la altura ó rango $R = 0$; simplificando bastante la ecuación Lidar en general y su correspondiente simulación mumérica.

CONCLUSIONES

En este trabajo se presentan las características más importantes a tomar en cuenta en el diseño y desarrollo de un sistema Lidar de retrodispersión elástica monoestático coaxial. Se mencionaron las propiedades más importantes del transmisor, el laser de Nd:YAG, así como una muestra de las caracterizaciones a sus pulsos. Se reportaron los parámetros más importantes del receptor, como es el tipo de telescopio a utilizar y sus datos más característicos. En la etapa de detección y grabado se define el tipo de PMT a utilizar y en que modo va a operar (conteo de fotones).

REFERENCIAS

1. Lidar: Range-resolved optical remote sensing of the atmosphere, Claus Weitkamp, Optical Sciences Springer 2005.
2. Applied Optics Vol. 18 No. 23 Dec. 1979
3. Applied Optics Vol. 22 No. 23 Dec. 1983
4. Applied Optics Vol. 42 No. 16 Dec. 2003
5. Applied Optics Vol. 46 No. 36 Dec. 2007

REVISTA BOLIVIANA DE FÍSICA 20s, 10-12, 2011
ISSN 1562-3823. INDEXADA EN: SCIELO, LATINDEX, PERIÓDICA

Medición de los lóbulos frontal y retrodispersión, de seis diferentes líneas, de los laseres de Ar y HeNe al atravesar neblina con diferentes densidades.

Reynoso Lara E., Serrano Muñoz G., Dávila Pintle J.A., Rendón Marín M.
Fac. de Cs. De la Electrónica, Benemérita Universidad Autónoma de Puebla, México.
E-mail: ereynoso@ece.buap.mx
Iturbe Castillo M.D., Treviño Palacios C.G.
Instituto Nacional de Astrofísica, Óptica y Electrónica *(INAOE)*, México.

RESUMEN

En este trabajo se muestran los resultados de las mediciones en laboratorio de los perfiles de intensidad, la razón de depolarización; así como el ensanchamiento de cinco diferentes líneas de un laser de Argón y una a 632nm de un laser de HeNe; al pasar a través de una cámara de neblina de gotas de agua con diferentes densidades. Los resultados obtenidos están en gran concordancia con los obtenidos Ryan y Carswell en [1]. Con la construcción de esta cámara de neblina, se pudo medir el ancho angular del lóbulo de dispersión frontal. Además con la ayuda de un arreglo interferómetrico y un microscopio con un desplazamiento mínimo de una diezmilésima de pulgada, se pudo medir el tamaño de las gotas de agua; se observó que el mejor ajuste para la distribución del tamaño de las gotas, fue con la función gamma generalizada, del tipo propuesta por Deirmendjian [2]. Una vez que se obtuvieron el valor de las constantes, de la función gamma, que mejor ajustaron el histograma de frecuencia se obtuvo el número de densidad de gotas por unidad de volumen. Aunque la mayoría de los estudios realizados, se han centrado en la retrodispersión de la luz por diferentes medios, principalmente nubes; sin embargo, el estudio del lóbulo de dispersión frontal se han podido estudiar con extrema precisión muchos factores, tales como la existencia de simple o múltiple dispersión y la cantidad en que se llevó a cabo. Esto es de gran importancia en la estimación de retornos lidar pues con esta fundamentaciones se puede conocer datos importantes como los coeficientes de extinción y retrodispersión, de partículas contaminantes en la atmosfera y entender el modelo de funcionamiento de la naturaleza.

Key words: Dispersión retro y frontal, razón de depolarización, ensanchamiento del haz.

INTRODUCTION

Aplicaciones recientes de técnicas lidar en la observación de los aerosoles atmosféricos y las nubes ha creado la necesidad de información más precisa sobre los efectos en tales medios de la propagación de haces. La mayoría de los estudios hasta la fecha se han preocupado principalmente con medidas de retro dispersión. Cuando los dispersores son algo más grande que la longitud de onda de la luz incidente, una fracción considerable de la luz se dispersa en un lóbulo estrecho angular en la dirección de avance. En algunas nubes atmosféricas, por ejemplo, la dispersión de adelante hacia atrás puede exceder 1000 a 1 en longitudes de onda visibles. Para las gotas de agua de un diámetro algo mayor que la longitud de onda, la teoría de la difracción se puede utilizar para estimar el medio ancho angular del lóbulo de dispersión hacia adelante. Esto significa que en nubes de la atmósfera que contienen gotas de varias micras de diámetro, el lóbulo frontal es sólo unos pocos grados de ancho en longitudes de onda visibles. Esto es de gran importancia en la estimación de retornos lidar a partir de nubes de espesor óptico altos, puesto que la anchura del haz del lóbulo frontal nos brinda información de cuanta luz es retro dispersada en un campo de visión dado.

MÉTODOS Y RESULTADOS

Como primer paso se trabajó con las mediciones del diámetro de las gotas de agua de neblina artificial. Para hacer mediciones acertadas a tan pequeña escala se obtuvo una medida de referencia con el que se pudiera medir el diámetro de las gotas de agua generada por la neblina creada en laboratorio.

Con un microscopio, modelo TM-11 Titán se midió el tamaño de las células de una cáscara de ajo, teniendo así nuestra mediada de referencia de 10um, posteriormente sobre esta muestra se haría pasar la neblina artificial creada en laboratorio impregnándose sobre esta las gotas de agua de la neblina las cuales se midieron. Por cada muestra obtenida, las gotas de agua de la neblina depositadas sobre las células de cascara de ajo, se colocaron sobre el microscopio, para fotografiarlas para después estudiar la muestra. En computadora mediante un software básico se creó una cuadricula de la medida de la referencia (10um), sobreponiendo sobre las fotografías, pudiendo hacer el conteo de una manera precisa del número de gotas por muestra y el diámetro de cada una de ellas. Un histograma de la distribución del tamaño de las gotas de agua de la neblina se muestra en la figura 1. A partir de este histograma observamos que tiene una distribución asimétrica donde la mejor función que se ajustó a la distribución del tamaño de las gotas de agua fue la función gamma generalizada del tipo propuesta por Deirmendjian.

$$n(r) = ar^b \exp(-cr^d)$$

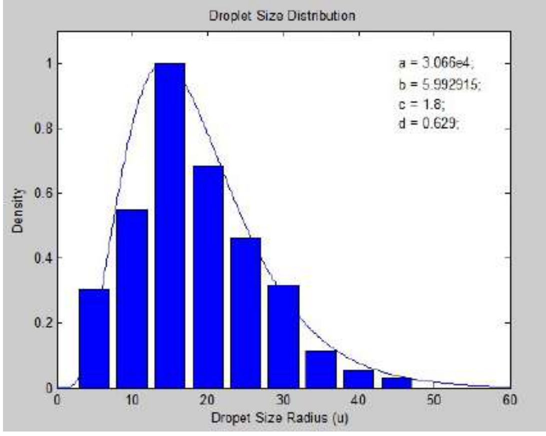

Figura 1. Ajuste de función gamma

Donde las constantes a, b, c, d fueron manipuladas para obtener el mejor ajuste. A partir función gamma generalizada y de los valores propios de sus contantes para su mejor ajuste, se puede obtener la densidad de gotas por unidad de volumen a partir de:

$$N = a\int_{\infty}^{0} r^b \exp(-cr^d)$$

Para medir el coeficiente de extinción de la neblina se utilizó la ley de Beer-Lambert descrita a continuación bajo el siguiente arreglo experimental:

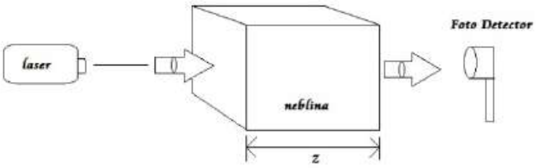

Figura 2. Arreglo experimental para medir el coeficiente de extinción de la neblina.

$$I_0 = I_i e^{-\alpha_{ext} z}$$

dónde:

- I_i e I_0 Son las intensidades de entrada y de salida a la neblina, respectivamente.

Para mantener un flujo constante de la neblina, se construyó una cámara, de material sintra negro, de un metro cúbico, a la cual se le hicieron dos perforaciones en caras opuestas para que el haz de luz atravesara la cámara.

El coeficiente de extinción está dado por la siguiente ecuación.

$$\alpha_{ext} = \alpha_a + \alpha_s$$

dónde:

- α_a Es el coeficiente de atenuación
- α_s Es el coeficiente de dispersión

En nuestro experimento el coeficiente de atenuación lo consideramos igual a cero, por lo tanto el coeficiente de extinción será igual al coeficiente de dispersión, teniendo entonces nuestra ecuación final para el cálculo de este coeficiente.

$$\alpha_{ext} = -\frac{1}{z}\ln\left(\frac{P_0}{P_i}\right)$$

2.1 Cálculo del coeficiente de extinción en laboratorio para diferentes longitudes de onda.

Para hacer un cálculo lo más exacto de coeficiente de extinción se realizaron varias mediciones, al variar las longitudes de onda, la potencia incidente y la densidad de la neblina dentro de la cámara.

Las longitudes de onda utilizadas en nuestro experimento fueron 457, 476, 488, 496, 514 nm de un láser de Argón, además de la línea de 633 nm de un láser HeNe. Para cambiar la potencia incidente de nuestra fuente de luz se utilizaron filtros con una densidad óptica (O.D.) específica, que la relacionaremos con la ecuación de transmitancia $T=10^{-O.D.}$ que determina el porcentaje de luz que travesará estos filtros Para modificar la densidad de la neblina dentro de la cámara, se varían las frecuencias acústicas de un humidificador que es el encargado de generar la neblina a estudiar. En la siguiente gráfica se muestran los resultados obtenidos del coeficiente de extinción para diferentes longitudes de onda.

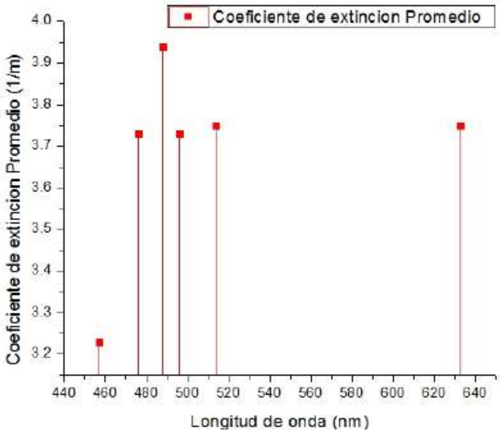

Figura 3. Gráfica de coeficientes de Extinción.

Una vez que se obtuvieron los valores, se calcula el coeficiente de extinción total promedio de nuestro experimento el cual es $\rightarrow \alpha = 3{,}71\text{m}^{-1}$.

2.2 Depolarización en la neblina.

La razón de depolarización es un parámatelo muy conveniente para describir el estado de polarización de un haz de luz, el cual se define como $\delta = \frac{I_2}{I_1}$ donde I_2 es la irradiancia que se obtiene con un polarizador, el cual su eje de transmisión está paralelamente alineado a la dirección de polarización del haz incidente, e I_1 es la irradiancia medida a la salida de un polarizador con su eje de transmisión perpendicular a esta dirección (polarizador cruzado).
El arreglo experimental que se utilizó para medir la razón de depolarización delta, se detalla en la figura 4:

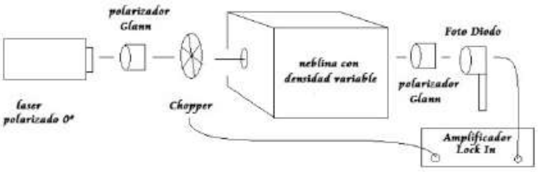

Figura 4. Arreglo experimental para medir depolarización en neblina de gotas de agua.

En este arreglo experimental se utilizó un Amplificador Lock-in para medir las bajas intensidades del polarizador cruzado, la frecuencia de referencia con la cual se modulo es de 100 Hz. La siguiente tabla muestra los resultados obtenidos a la salida del polarizador cruzado con desplazamientos transversales al eje de transmisión del haz, estos resultados solo incluyen dispersión hacia adelante.

fuente de luz (λ=633nm)	
Posición del foto detector	Salida Lock In
1 cm a la derecha	0.305 mv
2 cm a la derecha	0.330 mv
3 cm a la derecha	280 uv
4 cm a la derecha	25 uv
Eje de Transmisión	30.25 mv
1 cm a la izquierda	2.9 mv
2 cm a la izquierda	1.6 mv
3 cm a la izquierda	0.45 mv
4 cm a la izquierda	100 uv

Tabla 1. Datos de la depolarización de la luz

Estos datos se graficaron de manera polar y se ajustaron con la función de fase de Henyey-Greenstein donde g es el parámetro de asimetría (para nuestro caso=0.7) y θ es el ángulo de dispersión.

$$p(\theta) = \frac{1-g^z}{4\pi}(1+g^2-2g\cos\theta)^{-1.5}$$

CONCLUSIONES

Con la ayuda de un microscopio, modelo TM-11 Titán el cual tiene un desplazamiento mínimo de una diezmilésima de pulgada (aprox. dos micras) se pudo medir el tamaño de las gotas de agua de la neblina, observándose que tienen una distribución del tipo de la función gamma generalizada. La cual es útil para sacar la densidad de gotas por unidad de volumen. Se pudo observar que la neblina presenta diferentes coeficientes de extinción en diferentes longitudes de onda, existiendo una diferencia máxima de 0,2 m^{-1} entre las longitudes de onda de 488 y 457 nm. En las longitudes de onda de 476, 496, 514 y 633 nm en promedio el coeficiente de extinción es 3,71 m^{-1}.
Se puede observar en la gráfica de depolarización que conforme se aumenta la distancia transversal la razón de depolarización disminuye debido a que el lóbulo frontal formado es muy estrecho y la abertura de salida de la cámara es de 1cm.

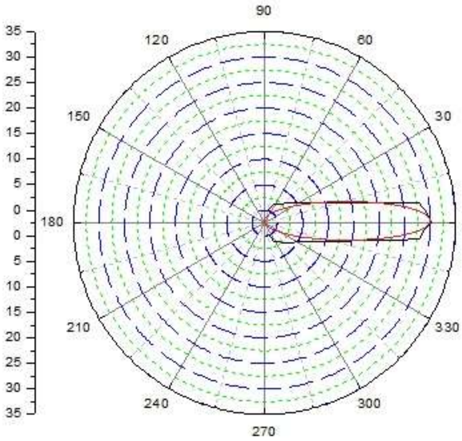

Figura 5. Ajuste de los datos medidos experimentalmente con la función de fase Henyey-Greenstein.

A continuación se muestra una gráfica que muestra la razón de depolarización con respecto a la distancia transversal.

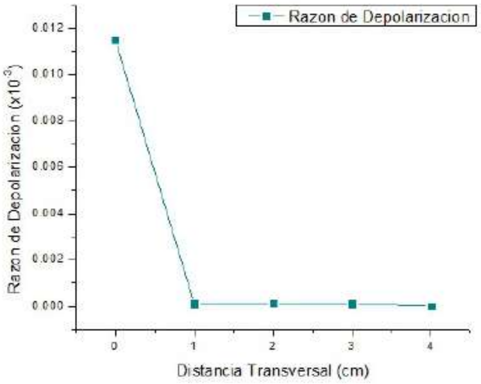

Figura 6. Razón de depolarización

REFERENCIAS

[1] . J.S. Ryan and A.I. Carswell. Optical Society of America. "Laser beam broadening and depolarization in dense fog".900-908. (1977).

[2] . John H. ScofieldA Frequency-Domain Description of a Lock-in Amplifier,Department of Physics, Oberlin College, Oberlin, OH 44074,American Journal of Physics 62 (2) 129-133 (Feb. 1994).

REVISTA BOLIVIANA DE FÍSICA 20s, 13-15, 2011
ISSN 1562-3823. INDEXADA EN: SCIELO, LATINDEX, PERIÓDICA

Systematic Ozone and Solar UV Measurements in the Observatorio Atmosférico de la Patagonia Austral, Argentina

Wolfram, E., Salvador, J., Orte, F, D'Elia, R., Quel, E.
Centro de Investigaciones en Láseres y Aplicaciones (CITEDEF-CONICET),
Villa Martelli, Argentina
Tel: +54-11-47098100 ext 1410, Fax: +54-11-47091006, E-mail: ewolfram@gmail.com
Casiccia, C, Zamorano, F.,
Universidad de Magallanez (UMAG),
Punta Arenas, Chile,
Tel: +56-61-207181
Paes Leme, N.
Instituto Nacional de Pesquisas Espaciais (INPE)
Natal, Brasil

SUMMARY

The depletion of the polar ozone layer is one of the strongest anthropogenic signals in the Earth system. Subpolar regions in the southern part of South America are affected by this phenomenon, covered sometimes by air masses with less ozone than normal with the corresponding UV enhancements at ground surface. Motivated by these atmospheric events, Argentina and Chile with the financial support of JICA has joined scientific efforts to develop UVO$_3$ Patagonia project. It has as main objectives monitoring ozone and UV radiation in Southern Patagonia. The Ozone and RUV laboratory (Chile) and the Lidar Division of CEILAP (Argentina) are the execute laboratories of this project. The Observatorio Atmosférico de la Patagonia Austral (Atmospheric Observatory of Southern Patagonia) is located in South Patagonia (51º 55'S, 69º 14'W), in subpolar region and it is a convenient monitoring site of the atmosphere in the Southern Hemisphere. In this experimental site is operative a differential absorption lidar instrument (DIAL) for the measurement of ozone vertical distribution. This instrument belongs of Network Data for Atmospheric Composition Change (NDACC). The altitude range of the ozone measurement is 14-45 km, which provides the opportunity to monitor the perturbations due to the passage of stratospheric polar air over Río Gallegos. Systematic stratospheric ozone profile measurement has been carried on in this experimental site since 2005. We identified three mayor perturbation of ozone hole over the stratospheric ozone profile in Río Gallegos. Approach of polar vortex during late winter, overpass of ozone hole in middle spring and dilution process during late spring change the shape and content of stratospheric ozone profile and by consequences the solar UV. Solar surface irradiance and total ozone content were measured with a Brewer spectraphotometer and moderate narrow band radiometer GUV-541 deployed in the Río Gallegos experimental site. Depleted ozone columns were measured during ozone hole overpass, and the analysis of unique extreme ozone depletion event in November 2009 is reported and compared with Multisensor Data Reanalysis of TOMS/OMI satellite data.

Key words: Lidar, Ozone, UV radiation, Polar Vortex

INTRODUCTION

Now a day we have strong evidence that human activities link to industrialized process have perturbed the natural balance of atmosphere composition (WMO, 2011). This fact has produced global scale issues like ozone depletion around the globe. The stronger manifestation of this phenomenon is the Antarctic ozone depletion today well known as ozone hole (Farman, 1985). Subpolar regions as the Patagonia in Argentina and Chile, in the southern part of South America are affected by this phenomenon covered sometimes by air masses with less ozone than normal with the corresponding UV enhancements at ground surface.

During the past twenty years, this phenomenon has varied in size and with respect to the minimum total ozone value within the Polar Regions. Dynamical processes into the stratosphere cause changes in the size and shape of the polar vortex, which elongates together with the ozone hole that is contained within the vortex. The daily movement of the vortex combined with this particular shape induces overpasses of the ozone hole over the continental part of South America. In these situations large inhabitant cities like Río Gallegos (51º 55'S, 69º 14'W) are under the influence of the ozone hole or near its border, causing an increase of solar UV radiation at these places [Pazmiño et al, 2005; Wolfram, 2009].

Motivated by these atmospheric events, Argentine, Chilean Japanese and French researchers cooperated to conduct atmospheric studies using remote sensing instrument. These instruments were installed in the Observatorio Atmosférico de la Patagonia Austral, OAPA, (Atmospheric Observatory of Southern Patagonia). In this work, we made a brief introduction to the measurement techniques of ozone and UV radiation held in this remote sensing site, and present, as example, same typical measurement.

METHOD AND RESULTS

Site description

The Observatorio Atmosférico de la Patagonia Austral, OAPA, (Atmospheric Observatory of Southern Patagonia) is part of Lidar Division of CEILAP (CITEDEF-CONICET). It is located in Río Gallegos city in South Patagonia (51º 55'S, 69º 14'W). Since June 2005, a shelter with several lidar instruments developed in collaboration with Service d'Aéronomie (CNRS) was deployed in this Patagonian city, 2600 km far away from Buenos Aires. During 2005 and 2007, with the financial support of JICA (Japanese International Cooperation Agency), was held the SOLAR campaign (www.division-lidar.com.ar) (Wolfram, et al., 2006). The principal objective of this campaign was study the ozone layer when the polar vortex crosses over the continental part of Argentina, in South America.

After SOLAR campaign, different projects were developed with financial support of JICA (Japan International Cooperation Agency) in partnership with researchers from Chile, France and Japan. The main objectives of these projects are focused in the observation of atmospheric parameter with lidar remote sensing techniques, specially the measurement of stratospheric ozone profiles using differential absorption lidar technique. Río Gallegos is located in the surf zone of polar vortex, making very interesting place to observe the evolution and perturbation that ozone hole produces on the stratospheric ozone profile.

The OAPA has currently different instrument devoted with the observation of gases (O_3 and NO_2) and particles (i.e aerosols) in the atmosphere, as much as the solar radiation (UV and visible). Several kinds of techniques are used to monitor ozone, like differential absorption lidar (DIAL) for determination of stratospheric ozone profiles and different radiometers, as SAOZ and Brewer for total ozone column measurements. In this paper we only focused in DIAL ozone products and solar UV index measured with GUV radiometer.

DIAL Instrument

The DIAL technique is a well-established technique for the ozone profile measurement, as is demonstrated by the large number of publications about the subject. The DIAL technique uses XeCl excimer laser emission at 308 nm for absorbed wavelength and the 355 nm third harmonic radiation of Nd-YAG laser for the reference wavelength. Both laser pulses are sending sequentially to the atmosphere. Six channels are used for the signal acquisition, four of them for the detection of elastically backscattered signal of the emitted wavelengths (high energy mode for the higher altitude ranges, attenuated energy for the lower ranges) and two corresponding to the first Stokes nitrogen Raman of the emitted wavelengths.

The optical receiving system consists of four parabolic telescopes (f/2) 50 cm diameter. Four quartz optical fibers are placed at the focal points of the telescopes and come together vertically to form the entrance slit of the spectrometer. These transmit the backscatter radiation from the atmosphere to an optical analyzer device, which includes optics for image formation, a chopper to prevent the saturation of the photomultipliers and a spectrometer designed to separate/split the different wavelengths to be detected. A fundamental part of the spectrometer is a Jobin Yvon holographic grating with 3600 lines per millimeter characterized by 40% efficiency in the 150-450 nm spectral range. It separates 5 wavelengths, 4 of which are used for obtaining ozone profiles and the combination of the fifth wavelength (347 nm) with one of the previous ones (332 nm) for obtaining profiles of water vapor in the troposphere. A full description of this DIAL system can be found in Wolfram et al (2008).

GUV radiometer

The multi-channel moderate-bandwidth GUV-541 have proven to be an acceptable solution for monitoring solar UV irradiance, between UV spectroradiometer very expensive and high maintenance, and broadband radiometers that provide only partial information because they cannot distinguish between changes in UV radiation caused by alterations in cloud cover and variations caused by changes in ozone amount. GUV filter radiometers, designed and manufactured by Biospherical Instruments Inc. The instruments provide measurements in five approximately 10 nm wide UV bands centered at 305, 313, 320, 340, and 380 nm.

The synergy of UV irradiance measured with this instrument and radiative transfer model permits to obtain UV related products, like UV index or erythemal irradiance, and cloud optical depth, between other. In this work we present UV index measurement derived from GUV radiometer.

Measurements

The ozone observation with lidar in OAPA are conducted within two different measurements protocols: an intensive period between August and November each year, (later winter - spring time at South Hemisphere), and routine measurement period for the rest of the year. During intensive measurement period which is coincident with the ozone hole development, the stratospheric ozone layer is monitored during 4 hours average time each available clear night.

Total ozone column in Río Gallegos follows a seasonal variation over the year with minimum values around autumn (March-April) and maximum values during spring (September-October). Over this annual variability total ozone column presents great day to day variation. These rapid changes are caused by the approximation and overpass on Río Gallegos of polar air masses that air isolated from middle latitude air by polar vortex.

The fluctuations on total ozone column are clearly appreciated in Figure 1, where total ozone column measured by OMI/AURA instrument (blue line) are plotted from 2005 to 2009. White line is the climatologic monthly mean ozone column using multi sensor reanalysis (MSR) total ozone column from 1987- 2008 time period**.**

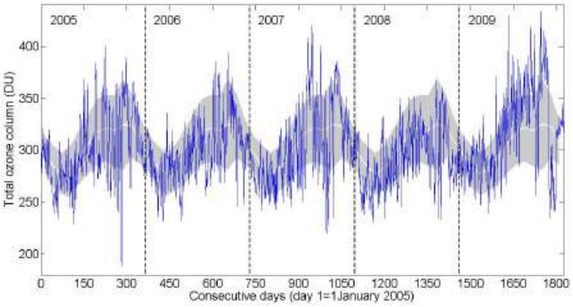

Figure 1. Time evolution of total ozone column over OAPA measured with OMI/NASA instrument (Blue Line). White line is the climatologic monthly mean ozone column using multisensor reanalysis (MSR) total ozone column from

1987- 2008 time period. Gray shadow area corresponds to +/- 1 standard deviation.

Stratospheric ozone profiles are measured with a Differential Absorption Lidar (DIAL). This instrument belongs to NDACC (Network for the Detection of Atmospheric Composition Change). Since 2005 this instrument has been monitoring ozone profiles in the stratosphere. Extreme ozone depletion has been measured as consequence of ozone hole passing over. Also, vortex dilution processes were measured in late spring-early summer.

The 2009 spring was a very special moment, because the polar vortex overpass several time during October, and it was stagnant over continent on November, producing strong perturbation of ozone profile as consequence of ozone hole located over Southern Patagonia. Figure 2 shows the DIAL ozone profile measured for middle November. The strong reduction over 20 km is clearly appreciated in comparison with the climatological profile of Fortuin & Kelder (Fortuin and Kelder, 1998) for this month and this latitude.

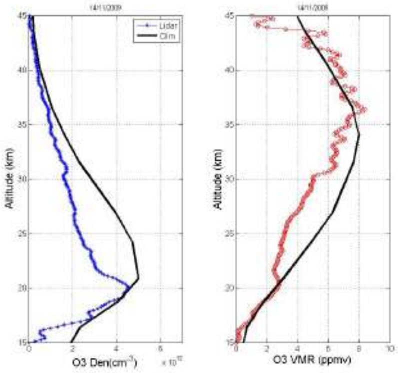

Figure 2. DIAL ozone profile on November 14, 2009. Blue line is the ozone number density (cm-3) (left panel, blue line) and ozone volume mixing ratio (ppmv) (right panel, red circles). For comparison of vertical ozone profile shape change, November climatologic Fortuin & Kelder ozone profile is included (black line).

These events produce strong impact in the solar UV radiation that reach ground surface (UVI). UVI is measured with different radiometers and Brewer spectra photometer (SN 124) of INPE. Particularly on November 15 the UV index reach values as high as 13 despite the cloud cover present in Río Gallegos for this day. It produces an extreme solar sunbathing.

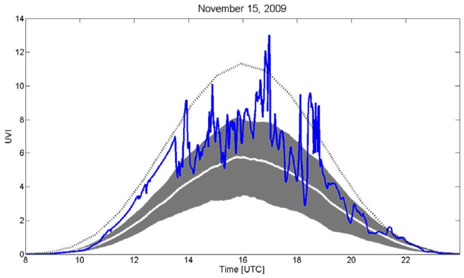

Figure 3. Time evolution of UV Index in Río Gallegos on November 15, 2009. The measurements were obtained with a GUV 541 and they are plotted in blue line. November monthly mean of UVI is showed in white line and the shadow grey area correspond to +/- 1SD. Modeled UVI for Nov. 15 is showed in dotted black line.

CONCLUSIONS

The OAPA is an atmospheric laboratory that performs several kinds of atmospheric measurements in Río Gallegos, Southern Partagonia. Since June 2005 stratospheric ozone profiles and solar UV radiation have been measured between other atmospheric parameters. In this paper we reported one example of differential absorption lidar measurement of stratosphere ozone number density in the 15 - 45 km range for a situation of ozone anomaly. Ozone hole overpass and vortex dilution are identified as examples of reduction and change in stratospheric ozone profiles. Also an extreme solar sunbathing occurred on November 2009 is reported. We identified three mayor perturbation of ozone hole over the stratospheric ozone profile in Río Gallegos. Approach of polar vortex during late winter, overpass of ozone hole in middle spring and dilution process during late spring change the shape and content of stratospheric ozone profile and by consequences the solar UV radiation that reach the surface.

ACKNOWLEDGMENTS

The authors would like to thank JICA (Japan International Cooperation Agency) by financial support of UVO$_3$ Patagonia Project; the CNRS in France for their collaboration in facilitating the shelter and part of the electronic instruments of DIAL.

REFERENCES

Fortuin J.P.F. and H. Kelder, 1998: "An ozone climatology base on ozonesonde and satellite measurements", *J. Geophys. Res.* vol. **103**, 31,709-31,734.

Pazmiño, A., S. Godin-Beekmann, M. Ginzburg, S. Bekki, A. Hauchecorne, R. Piacentini, E. Quel "Impact of Antartic polar vortex occurrences on total ozone and UVB radiation at southern Argentinean and Antarctic stations during 1997-2003 period" *J. of Geophysical Research,* Vol **110**, D03103, 1-13 (2005).

Wolfram E., J Salvador, J. Pallotta, R.D'Elia1, L. Otero, S. Godin-Beeckmann, H. Nakane, E. Quel. Solar Campaign: First Results Of Ozone Profile Measurements At Rio Gallegos, Argentina, *Reviewed and Revised Papers Presented at the 23rd International Laser Radar Conference* Editors Chikao Nagasawa, Nobuo Sugimoto, **Part II** 365-368, (2006).

Wolfram E A, J Salvador, R D'Elia, C Casiccia, N Paes Leme, A Pazmiño, J Porteneuve, S Godin-Beekman, H Nakane and E J Quel, New differential absorption lidar for stratospheric ozone monitoring in Patagonia, South Argentina, *J. Opt. A: Pure Appl. Opt.* **10** (2008) 104021 (7pp). doi:10.1088/1464-4258/10/10/104021, ISBN: 1464-4258

Wolfram, E., J. Salvador, R. D'Elia, E. Quel, UV ground based measurements in Río Gallegos, Argentina.Current Problems in Atmospheric Radiation (IRS), p.1100351-354, 2009

WMO (World Meteorological Organization), Scientific Assessment of Ozone Depletion: 2010, Global Ozone Research and Monitoring Project-Report No. 52, 516 pp., Geneva, Switzerland, 2011.

REVISTA BOLIVIANA DE FÍSICA 20s, 16-18, 2011
ISSN 1562-3823. INDEXADA EN: SCIELO, LATINDEX, PERIÓDICA

Study on aerosol properties over Madrid (Spain) by multiple instrumentation during SPALI10 lidar campaign

F. Molero, A. J. Fernández, M. Pujadas,
Centro de Investigaciones Energéticas, Medioambientales y Tecnológicas (CIEMAT)
Avda Complutense, 22. Madrid, 28040. SPAIN
Tel: +34913466174, Fax: +334913466212, E-mail: f.molero@ciemat.es
M. Sicard, S. Tomás, A. Comerón, D. Lange, D. Kumar, J. Giner, C. Muñoz, F. Rocadenbosch
Department of Signal Theory and Comunications, Remote Sensing Lab., Universitat Politécnica de Catalunya
Jordi Girona 1-3, Barcelona, SPAIN
F. Navas-Guzmán, M.J. Granados, L. Alados-Arboledas, J.A. Bravo-Aranda
Andalusian Center for Environmental Research (CEAMA), University of Granada
Av. del Mediterráneo s/n, 18071, Granada, SPAIN
and **J. Preißler, F. Wagner, J.L. Guerrero-Rascado**
Évora Geophysics Centre (CGE), University of Évora
Rua Romão Ramalho 59, 7000, Évora, PORTUGAL

SUMMARY

Understanding the effect of aerosols upon radiative forcing requires information about vertical profiles. Lidar techniques represent a powerful tool for studies of the vertical structure of the aerosol field. During the SPAin Lidar Intercomparison 2010 (SPALI10) campaign, several multiwavelength Raman lidar systems measured simultaneously in order to assess their performances. Multiwavelength lidars can provide relevant vertically-resolved information on aerosol optical properties because the wavelength dependence of the backscatter and extinction coefficients allows for a more detailed discrimination of aerosol types. Several lidar stations belonging to SPALINET, the Spanish and Portuguese Lidar NETwork and also EARLINET, the European Aerosol Research Lidar NETwork, intercompared during a campaign that took place in Madrid from 18 October to 5 November 2010. The products provided by the lidar systems were compared with ancillary data. At ground level, aerosol size distribution was continuously monitored. Additionally, the column-integrated characterization of the atmospheric aerosol was performed by means of a sun photometer. The extensive dataset obtained during SPALI10 field campaign enables to compare ground-level in-situ measurements with remote sensing techniques to determine vertically-resolved optical and microphysical properties of aerosols. Several relevant features shown in the comparison of the results obtained by the different instruments are discussed in this work.

Key words: Aerosols, lidar, size distributions.

INTRODUCTION

The high variability of tropospheric aerosols both in space and time is one of the main reasons of the high uncertainty of radiative forcing estimates in climate change studies [Forster, 2007]. The aerosol vertical distribution is of crucial importance in radiative transfer calculations. In studying the vertical structure of the aerosol field and its temporal and spatial evolution, lidar techniques represent a powerful tool because of their capability to provide aerosol profiles with high resolution. Multiwavelength lidars can provide additional information on aerosol characterization because the wavelength dependence of the backscatter and extinction coefficients allows for a more detailed discrimination of aerosol types [Müller, 2001]. Several lidar stations belonging to SPALINET, the Spanish and Portuguese Lidar NETwork [Sicard, 2009] and also EARLINET, the European Aerosol Research Lidar NETwork [Bösenberg, 2003] intercompared during SPALI10 (SPAin Lidar Intercomparison 2010) field campaign that took place in Madrid (40.45ºN, 3.73ºW, 663 m asl) from 18 October to 5 November 2010. All network stations routinely perform internal quality checks and participated in intercomparisons both at the instrument and algorithm levels with standardized procedures [Matthias, 2004]. In this work, several relevant features shown in the comparison of vertically-resolved optical properties of aerosols with ground-level in situ data and column-integrated aerosol properties provided by sun-photometer remote sensing techniques, are discussed.

METHOD AND RESULTS

The aim of the campaign was to compare simultaneous lidar measurements from several network stations (Madrid, Granada, Barcelona and Évora) with a reference lidar system from Potenza (Italy) in order to assess their performances measuring the same atmosphere during the same time periods. Simultaneously, an extensive dataset from both ground-level in-situ measurements and remote sensing techniques was collected for characterizing aerosol optical and microphysical properties. All lidar systems were collocated close on a flat terrain, with laser pointing close to the zenith. Several sessions each with some hours of measurement time were scheduled for every day of the campaigns, both at day and night, in order to obtain sufficiently long periods with stable atmospheric conditions and with all lidar systems working properly. The results of the campaign can be considered satisfactory as the campaign allowed to check the performances of the systems and when they were not fully satisfactory, the reasons of the failure were understood and a way to solve them could be defined.

All the intercompared lidar systems use pulsed Nd:YAG laser emitting at 1064, 532 and 355 nm, configured in a monostatic biaxial alignment pointing vertically to the zenith, except for the Évora system, that is tilted 5º to improve cirrus studies. The receiving lines consist of Cassegrain or Newtonian telescopes and wavelength separation units with dichroic mirrors, interferential filters and polarization cubes. From the elastic lidar signal, aerosol backscatter coefficient profiles have been retrieved using the Klett algorithm [Klett, 1981]. The retrieval of backscatter coefficient profiles requires the use of a modeled value for the lidar ratio (i.e., the ratio between aerosol extinction and backscatter coefficient), a value of 50 sr was selected. The column integrated characterization of the atmospheric aerosol was performed by means of an automatic sun tracking photometer Cimel CE-318-4 [Holben, 1998], operated by the Granada team. This instrument makes direct sun irradiance measurements at 340, 380, 440, 670, 870, 940 and 1020 nm. These solar extinction measurements are then used to compute Aerosol Optical Depth (AOD) at each wavelength. The AOD is derived from the total optical depth obtained from direct sun-photometer measurements data. The sky radiance measurements, performed at the almucantar and principal planes at 440, 675, 870, and 1020 nm together with solar direct irradiance measurements at the same wavelengths, were used to retrieve the aerosol single-scattering albedo, phase function, aerosol optical thickness and the volume size distribution (dV(r)/dlnr ($cm^3 cm^{-2}$)) using the radiative transfer code SKYRAD.pack software [Nakajima, 1996]. At ground level, the temporal evolution of particle number concentration for particles with aerodynamic diameter smaller than 10, 2.5 and 1 μm (PM10, PM2.5 and PM1, respectively) were monitored at the experimental site. Dry ambient sub-micrometer size distributions were monitored at the site by using a Scanning Mobility Particle Sizer (TSI SMPS 3936), combining a long Differential Mobility Analyzer (DMA) and a Condensation Particle Counter (CPC model 3775) working in the scanning mode. On a larger particle size range, an Optical Particle Counter (GRIMM 1108) was used. Both instruments allow to obtain a single plot for number distributions between 0.015 to 10 μm by joining their data. Volume distributions (dV/dlog(Dp)) were calculated assuming that aerosol particles were spheres with a radius equal to the centre radius of each bin measured by the instruments.

The meteorological analysis showed a synoptic situation mainly governed by high-pressure systems over the Iberian Peninsula during the first two weeks of the campaign, promoting stagnation. After these days there was a 3-day rain episode ending on 31 October, followed by a period with the Azores high-pressure system dominating over the peninsula, yielding the entry of air masses from the Atlantic. Figure 1 shows aerosol backscatter profiles derived from the Madrid system range-corrected signals, at the three elastic wavelengths, for 21 October (Top panels) and 2 November (Bottom panels) daytime sessions. On 21 October, there was a thermal inversion at 1100 m asl, determined by the inflexion point of the virtual potential temperature profile. The backscatter profiles show two aloft layers, at 1600 and 2100 m asl, probably due to the stagnation conditions. Backscatter-related Ångström exponents obtained between the 532 and 355 nm and 1064 and 532 nm profiles for these layers are different than that of the mixing layer, indicating different aerosol characteristics. Assuming the aerosol source was local, the change in the characteristics might be caused by chemical transformation in the atmosphere of previous days' emitted aerosols. On the 2 Nov, all the aerosol content was comprised in the mixing layer, that reached 2000 m asl. Backscatter-related Ångström exponent obtained between 1064 and 532 nm was constant, with a value of 1.5, in this case due to the cleaning of the atmosphere from day-to-day.

Figure 2 shows the column-integrated volume size distributions provided by the sun-photometer and derived from ground-level measurements, using the lidar profiles to determine the scale height required to make them comparable [Fernández-Gálvez, 2011]. The two techniques measure different quantities; sun-photometer remote sensing is sensitive to the aerosol optical properties of the entire column, while in-situ instruments measure the aerosols at ground-level, which may not be representative of the distributed aerosol in the total boundary layer. The distributions obtained by in-situ instrumentation at surface level (in $\mu m^3\ cm^{-3}$) are converted into columnar distribution ($cm^3\ cm^{-2}$) for comparison with sun-photometer retrievals by means of a scale height provided by the lidar profile. The observed size distributions are typically bimodal, with the first modal radius between <0.015 and 0.4 μm, and the second between 0.5 and >10 μm. Between these modal values generally there is a minimum (inflection point), corresponding to a radius of about 0.4 μm. The agreement between the volume size distribution provided by the inversion code and that measured at ground-level was reasonable, taking into account the assumptions made for the comparison. The presence of a lofted layer with a different type of aerosol, although with very low backscattering values, might influence the comparison, raising concern about the validity of the scale height value employed in the conversion of the surface data

CONCLUSIONS

During the SPALI10 lidar intercomparison campaign at Madrid, the products provided by multiwavelength lidar systems were compared with ancillary instrumentation data. At ground level, aerosol size distribution was continuously monitored between 15 nm and 20 μm by merging two particle counters. Additionally, the column-integrated characterization of the atmospheric aerosol was performed by means of a sun-photometer. The vertically-resolved aerosol optical properties at three wavelengths provide information about the type of aerosol present in the different layers observed. A comparison of columnar versus ground-level measurements of aerosol size distribution was performed. In-situ measurements at ground-level were converted into column-integrated values using the retrieved scale height values provided by lidar profiles. Both techniques yield bimodal aerosol size distribution, with an inflection point around 0.4 μm, with better agreement in the size range between 0.2 and 2 μm, where the inversion algorithm for sun-photometer data is more reliable. Aerosol layer structure detected by the lidar system might explain the discrepancy observed in the absolute values and shape of each mode on the 21 October, when several layers with aerosols with different optical properties were detected aloft. A better agreement is found on the 2 November, when all the aerosol where comprised in the mixing layer, with constant optical properties. Further investigations are ongoing to obtain relevant vertically-resolved aerosol optical properties from multiwavelength Raman lidar systems.

ACKNOWLEDGMENTS

The work was supported by the European Union under project nº 025991 (RICA), by the MICINN under the projects CGL2010-17777, CGL2008-01330-E/CLI & CGL2010-09225-E and by the ESA-CEOS Intercalibration of Ground-Based Spectrometers and Lidars (CEOS-IC-PR01) project.

REFERENCES

Bösenberg, J., et al. (2003) EARLINET: A European Aerosol Research Lidar Network to establish an aerosol climatology, *Rep. 348, Max-Planck Inst. für Meteorol.*, Hamburg, Germany.

Fernández-Gálvez, J. et al. (2011), Aerosol size distribution from inversion of solar radiances and measured at ground-level during SPALI10 campaign, *Proc. of the Global Conference on Global Warming 2011*. 11-14 July, 2011, Lisbon, Portugal

Forster, P. et al. (2007), Changes in atmospheric constituents and in radiative forcing, in *Climate Change 2007: The Physical Science Basis. Contribution of Working Group I to the Fourth Assessment Report of IPCC*, edited by S. Solomon, 129–234, Cambridge Univ. Press. U.K..

Holben, B.N. et al. (1998), AERONET: A federated instrument network and data archive for aerosol characterization, *Remote Sens. Environ*., 66, 1–16

Klett, J.D., (1981), Stable analytic inversion solution for processing Lidar returns", *Appl. Opt*., 20, 211-220

Matthias, V. et al. (2004), Aerosol lidar intercomparison in the framework of the EARLINET project. 1. Instruments *Appl. Opt.*, 43(4), 961–976

Müller, D. et al. (2001), Comprehensive particle characterization from 3-wavelength Raman-lidar observations: Case study, *Appl. Opt.*, 40(27), 4863–4869,

Nakajima, T. et al. (1996), Use of Sky brightness measurements from ground for remote sensing of particulate polydispersions, *Appl. Optics*, 35, 2672-2686

Sicard, M. et al. (2009) Aerosol Lidar Intercomparison in the framework of SPALINET – The Spanish Lidar Network: Methodology and Results *IEEE Trans. Geosci Rem Sens* 47 (10) 3547-3559.

REVISTA BOLIVIANA DE FÍSICA 20s, 19-20, 2011
ISSN 1562-3823. INDEXADA EN: SCIELO, LATINDEX, PERIÓDICA

Evaluation of inversion algorithm sensitivity in stratospheric ozone DIAL profile.

Orte, F., Wolfram, E., Salvador, J., D'Elia, R., Quel, E.
CEILAP (CITEFA-CONICET), Villa Martelli, Argentina. (fellowship of ANPCyT)
Villa Martelli, Argentina
Tel: +54-11-47098100 ext 1410, Fax: +54-11-47091006, E-mail: porte@citedef.gob.ar

SUMMARY

The DIAL system belonging to Observatorio Atmosférico de la Patagonia Austral, Río Gallegos, Argentina has been included in the NDACC since December 2008. One caveat of large networks such as NDACC is the difficulty to report information of similar nature consistently from one research group (or instrument) to another. The inversion algorithm used in the stratospheric ozone DIAL measurements involves different source of systematic and statistic errors. Due to the rapid decrease of the signal-to-noise ratio in the high stratosphere, it is necessary to degrade the vertical resolution of the measurement in order to limit the statistical error at this altitude range, to reasonable values. The final statistical error on the measurement is the result of a compromise between the experimental system characteristics such as the duration of the measurement and the final vertical resolution. The aim of this study is test the DIAL algorithm resolution used to retrieve the ozone profile comparing with the synthetic ozone profile. This synthetic ozone profile is calculated by mean of lidar equation using an ECC sonde profile as input parameter. This ozone profile was measured with an ozonesonde launched in Río Gallegos in March 2011 as part of intercomparison campaign.

Key words: DIAL, vertical resolution, ozone profile.

INTRODUCTION

Use of Differential Absorption Lidar (DIAL) systems is becoming more widespread for monitoring the ozone vertical distribution throughout the world (Sophie Godin et. al., 1999).
In Observatorio Atmosférico de la Patagonia Austral (OAPA) was installed a Lidar system which retrieve ozone profiles in the stratosphere since 2005. In 2008 this lidar joined to the Network for the Detection Composition Change (NDACC) for the long-term monitoring of stratospheric ozone.
To achieve the goals of the NDACC, the ozone profile supplied to the NDACC archive have been extensively checked in intercomparison campaigns. However, uncertainty exists with respect to the interpretation of altitude resolutions reported by various ozone DIAL instruments (Georg Beyerle et.al., 1999).
For a DIAL system, ozone number densities $n_{O3}(z)$ are calculates by

$$n_{O_3}(z) = \frac{1}{\sigma_{on} - \sigma_{off}} \left[\frac{1}{2} \left(\frac{d}{dz} \ln \frac{P_{off}(z)}{P_{on}(z)} \right) \right] - \left[\alpha_{on}(z) - \alpha_{off}(z) \right]$$

where the contribution from aerosols has been neglected; σ_{on} and σ_{off} are the ozone absorption cross section for wavelength λ_{on} and λ_{off} respectively; α_{on} and α_{off} are the extinction coefficient for molecular scattering for the mentioned wavelength; and P_{on} and P_{off} are the lidar signals.
The evaluation of the term d/dz ln $[P_{off}(z)/P_{on}(z)]$ is an essential element of the analysis. Generally, differentiation has the effect of applying a high-pass filter to a signal. In DIAL analysis this fact represents a problem, as the signal counts P at stratospheric altitudes contain high-wave-number noise contributions
Typically, the altitude resolution $\Delta z(z_i)$ of ozone profiles is defined in terms of the derivative filter. Because various filters are used, values of $\Delta z(z_i)$ from different data analyses are generally not comparable.
Here we test the algorithm used in the DIAL system of OAPA to retrieve the vertical ozone variation. To that end we use the synthetic ozone profile measured by ozonesonde like an input to calculate the lidar signal for then obtain the ozone profile from the DIAL algorithm. This profile calculated is compared with the ozonesonde. The lidar signals are calculated without noise.

METHOD AND RESULTS

In a pure molecular atmosphere (i.e. neglected the aerosols) the lidar signal for an altitude z of the atmosphere and for a wavelength can be written like

$$P(z) = k \frac{\beta_{molec}}{z^2} e^{-2\left[\int_{z0}^{z} \beta_{molec} \cdot \frac{8\pi}{3} dz + \int_{z0}^{z} \sigma_{O_3} . n_{O_3} dz \right]}$$

where $\beta_{moléc}$ is the Rayleigh backscatter coefficient; $8\pi/3$ is the ratio between extinction and molecular backscatter; σ_{O3} is the ozone cross section and n_{O3} is the ozone number density. The value of 2 before the exponent indicate that the laser bin pass through the atmosphere two times between z_0 (site altitude) and z. The first term of the exponent counts the extinction of the atmosphere due to scattering of molecules only for a given wavelength while the second term take in account the absorption of ozone at this emitted wavelength. To obtain the synthetic lidar signal for λ_{on} and λ_{off} we need to calculate the backscatter coefficient and the second term of the exponent for both wavelengths. The backscatter coefficient β was calculated from the density of the atmosphere using the pressure and temperature profile measured by a sonde launched in Punta Arenas, Chile, near of OAPA. Knowing the ozone cross section for two interest wavelengths, we can calculate the second term of the exponent from the ozone profile measured by the ozonesonde between 0 and 32 km as input of the DIAL algorithm. This profile was completed with the Fortuin & Kelder(1998) climatology profile.

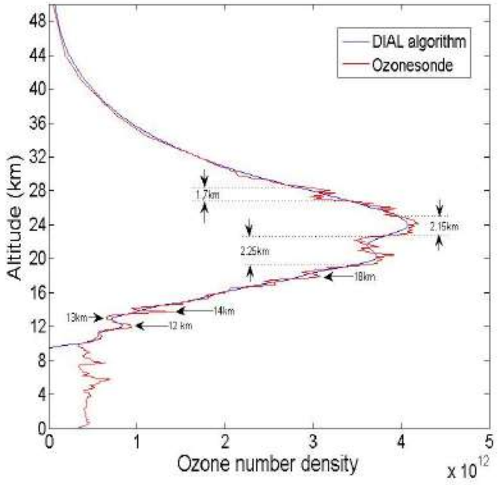

Figure 1. Comparison of both calculated ozone profile from the DIAL algorithm in the OAPA (blue) and the synthetic ozone profile obtained from measured by ozonesonde (red).

Figure 1 shows a comparison between the ozone profile calculated (DIAL algorithm) and ozone profile measured by the ozonesonde which was used as an input to calculate the lidar signals. Although the lidar signals in λ_{on} and λ_{off} (308nm and 355nm respectively) was calculated without noise, the algorithm has an intrinsic resolution. The calculate profile is like the measured one but more smoothed. The highlighted zones show the altitudes where the variations of ozone number density are greater. Around the 12 and 13 km have two local peaks where the resolution (figure 2) is 0.8km. The calculated profile follows the behavior of measured but not reaches the local maximum and minimum of the peak. At 14 km there is other local peak but more narrow. The resolution at this altitude is 0.8km and the wide of the peak is 0.4 km. For this reason is probably that the calculated profile can't "see" this layering. Around 20 km the ozone profile measured by the sonde shows a large variation. The measured profile presents four peaks.

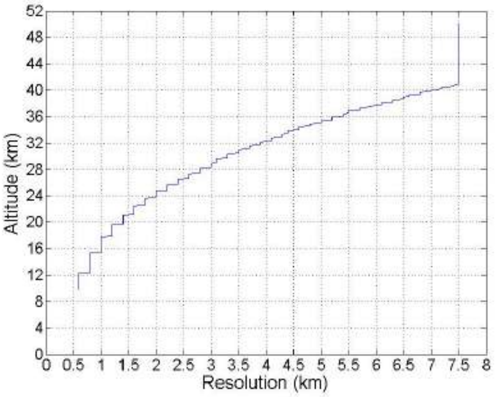

Figure 2. Vertical resolution used in the DIAL algorithm.

The calculate profile follows the ozonesonde but very smooth. Figure 2 shows the resolution increase with the altitude and in that altitude (around 20 km) the calculated profile doesn't follow the thin peaks. Around the 28 km where the resolution is of 3km, the measured profile presents a variation similar to 12 and 13 km. We observe that the DIAL algorithm profile don't follow this trend due that the resolution in this altitude is greater than the resolution at lower altitude.

CONCLUSIONS

We presented a descriptive study of a vertical ozone profile obtained by the DIAL algorithm used in Río Gallegos. This study shows how act the DIAL algorithm smoothing the ozone profile calculated respect of the measured and variations in the shape of ozone profile in same layer is lost. It is important to note that the calculated profile was obtained without noise. In future studies we try to introduce a modeled noise to obtain lidar signals more real.

ACKNOWLEDGMENTS

The authors would like to thank JICA (Japan International Cooperation Agency) by financial support of UVO_3 Patagonia Project; the CNRS in France for their collaboration in facilitating the shelter and part of the electronic instruments of DIAL.

REFERENCES

Fortuin J.P.F. and H. Kelder, 1998: "An ozone climatology base on ozonesonde and satellite measurements", *J. Geophys. Res.* vol. **103**, 31,709-31,734.

S. Godin, A.I. Carswell, D.P. Donovan, H. Claude, W. Steinbrecht, I.S. McDermid, T.M. McGee, M.R. Gross, H. Nakane, D.P. Swart, H.B. Bergwerff, O. Uchino, P. von der Gathen and R. Neuber, Ozone differential absorption lidar algorithm intercomparison. Appl Opt, **38** (1999), pp. 6225–6236.

Georg Beyerle and I. Stuart McDermid, "Altitude Range Resolution of Differential Absorption Lidar Ozone Profiles," Appl. Opt. 38, 924-927 (1999).

REVISTA BOLIVIANA DE FÍSICA 20s, 21-23, 2011
ISSN 1562-3823. INDEXADA EN: SCIELO, LATINDEX, PERIÓDICA

Southern Brazil: analysis of aerosols from different sources through the sensors MODIS and CALIOP

Glauber Lopes Mariano
Professor - Meteorology Department at Universidade Federal de Pelotas
Pelotas-RS, Brazil
Tel: +55 5332757321 , E-mail: glauber.mariano@ufpel.edu.br
Ericka Voss Chagas Mariano
PhD student – National Institute for Space Research – Space Geophysics Division
São José dos Campos-SP, Brazil
E-mail: erickavoss@gmail.com
Renã Moreira
Graduation student - Meteorology Department at Universidade Federal de Pelotas
Pelotas-RS, Brazil
Tel: +55 5332757321, E-mail: rena543@gmail.com

SUMMARY

Aerosols in the atmosphere directly and indirectly influence the climate of a region. However, studies related to the effects of aerosols in some areas are scarce. The southern region of Brazil is located next to major known sources of particulate matter (Brazilian savanna, Amazonia and southeastern Brazil). Thus, it has the peculiarity of having the contribution of the transport of aerosols from other sources with optical characteristics very different from each other, also with the influence of regional aerosols. This paper aims to present a project to analyze the impact of aerosols in the atmosphere over the Southern region using satellite data from Terra/Aqua (MODIS) and CALIPSO (CALIOP sensor) in the period from 2007 to 2010. With the measurements of aerosol optical depth, the atmosphere in the region will be classified into different groups. We also intend to analyze the vertical profile of aerosols and transport patterns of particulate matter from sources close to the study area, the latter with FNL data from NCEP with 1.0 ° of space resolution and time resolution of 6h. Through the preliminary results it is clear that the optical depth of aerosols in the years 2009 and 2010 reached a maximum during the winter period, probably due to fires that occur in a large part of South America

Key words: aerosol, MODIS, southern Brazil, CALIPSO

INTRODUCTION

The atmospheric aerosol consists of solid and liquid particles suspended in the atmosphere and have direct and indirect impacts on climate. The direct influence of aerosols on climate is the ability to absorb or reflect solar radiation, which depends on the chemical properties and particle size, resulting in a heating or cooling of the atmosphere. The indirect effects of aerosols refer to their ability to act as cloud condensation nuclei, changing the properties of clouds (Seinfeld and Pandis, 1998).

The southern region of Brazil, besides the aerosols emitted locally by natural and anthropogenic sources, suffers from the advection of pollutants originated at the major regions of aerosol production (e.g. the Amazon region, central and southeastern Brazil) due to the circulation present in the region (e.g. Freitas et al., 2006) (figure 1). This causes an impact on both the quantity of aerosols in the region and in the net radiation at the surface.

Some preliminary studies in the project scope using data from the MODIS sensor have shown the influence and impact of some types of aerosols in the atmosphere of southern Brazil, highlighting burning aerosols and volcanic ash resulting from the eruption of Puyehue, Chile, in June 2011.

One way to study and evaluate the impacts induced by the aerosols is to analyze its vertical distribution and impact of their presence through variables such as aerosol optical depth (AOD), in addition to the backscatter and absorption coefficients as used in a series of recent studies for the state of São Paulo (Landulfo et al., 2010, Mariano et al., 2010a and Mariano et al., 2010b).

Therefore, it is necessary to deepen the knowledge of the impacts that aerosols originating from local sources and advected from other regions in the Southern Brazil have in the local atmosphere, in order to understand its influence on solar radiation and consequent improvement of meteorological models.

METHOD AND RESULTS

MODIS sensor

The MODIS sensor is onboard the polar orbiting satellites Terra and Aqua launched in 1999 and 2002, respectively. The sensor was the first designed to obtain global observations of aerosols with moderate resolution (between 250m and 1000m depending on the wavelength used).

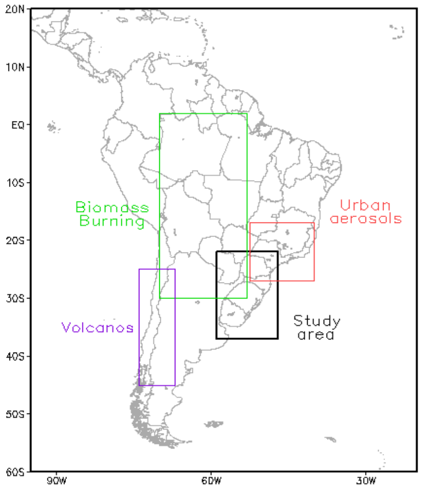

Figure 1. Aerosol type and study area

General and operational characteristics of the sensor can be found at Barnes et al. (1998). It is noteworthy that the same has 36 spectral bands between 0.4 and 14.5 µm, allowing the generation of several products related to aerosol optical depth over the ocean and land with a resolution of 10x10 km (at nadir), and to the size distribution and type of aerosol over the continent.

CALIOP sensor

The satellite Cloud-Aerosol Lidar and Infrared Pathfinder Satellite Observations (CALIPSO) has an on-board LIDAR system operating at two wavelengths (1064 and 532nm), called the Cloud-Aerosol LIDAR with Orthogonal Polarization (CALIOP). The spatial resolution of the sensor depends on the altitude – from the surface to 8.2 km the horizontal resolution is 333 m and 30 m vertically, while between 8.2 and 20.2 km is 1000 m and 60 m, horizontal and vertical resolution, respectively.

DATA AND STUDY REGION

The data used will be from MODIS (TERRA and AQUA satellites) and the CALIOP sensor (CALIPSO satellite) in the period from 2007 to 2010, to analyze the impact of different types of aerosol in the optical depth and backscatter and absorption coefficients.

The MODIS sensor data analyzed in the project consists of the product aerosol level 2 and 3, respectively MOD04 and MOD08. These two levels of data are generated globally every day, offering several properties related to aerosols such as optical depth over ocean/continent and Angstrom exponent over land. The data spatial resolution is 10x10 km (at nadir) for products of level 2 and 1.0 º for level 3.

Concerning the vertical profile of aerosols and some of its optical properties, data from the CALIOP sensor in the so called level 1B and level 2, that provide information of the perpendicular and total backscattering attenuated coefficient at 532 nm and 1064nm, and the extinction coefficient at 532 and 1064 nm and values of Lidar Ratio, will be used.

It is intended to also use the information obtained by the CALIOP sensor on the observed particle type (also called vertical mask), and aerosol subtype. To obtain the synoptic patterns that cause the transport of aerosols of known major sources such as the Amazon Region, Midwest and Southeast regions of Brazil to the Southern Region, the final analysis (FNL) of the National Centers for Environmental Prediction (NCEP) for the same period mentioned above will be used. These analyses have spatial and temporal resolutions of 1x1 degrees and 6 h, respectively, and 26 vertical levels.

Initially, it is intended to separate, by seasons, the optical depth obtained in four different groups for the study area, as shown in Table 1. Thus, 100% refers to the maximum AOD found during the study period, in southern Brazil (black area at Figure 01).

Table 1. Characterization of the atmosphere according to the values of the maximum aerosol optical depth (2007-2010) at 550nm

Atmospheric characterization	Optical Depth at 550nm
Very clear atmosphere	< 20%
Clear atmosphere	20% ≤ AOD < 50%
Polluted atmosphere	50% ≤ AOD < 80%
Very polluted atmosphere	≥ 80%

RESULTS

A preliminary analysis of the aerosol optical depth in the years 2009 and 2010 for São Paulo, Pelotas, Chuí and Foz do Iguaçu can be seen in Figure 2. Note an increase of the values during the winter of the region in both years. Possibly, this increase is due to the entrance of burning plumes that occurred in central Brazil and at the Amazon. It was noticed that the maximum values found during the study period was: 1.2 (São Paulo), 3.2 (Pelotas), 2.4 (Chuí) and 4.2 (Foz do Iguaçu).

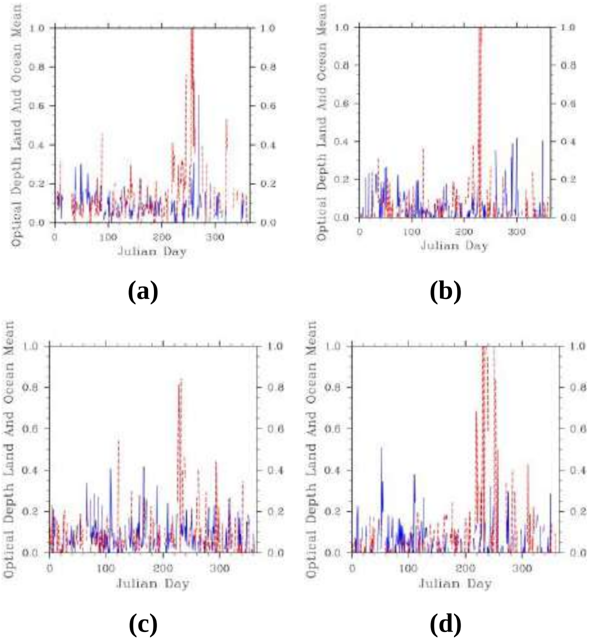

(a) **(b)**

(c) **(d)**

Figure 2. Aerosol optical depth at 2009 (blue) and 2010 (dashed red) to São Paulo(a), Pelotas (b), Chuí (c) and Foz do Iguaçu (d) obtained by the MODIS sensor .

The reason for the apparent low value of optical depth for the city of São Paulo may have been resultant of the choice for the point of extraction of values from the MODIS sensor data. This indicates that one should choose an area representative of São Paulo and then extract the maximum value of this region.

Figure 3 shows three examples of types of aerosols over the southern region of Brazil (being better distinguished between latitudes 28° S and 35° S). It can be noted, over the study area, smoke aerosol (Figure 3a), polluted continental (Figure 3b) and dust and polluted dust (Figure 3c).

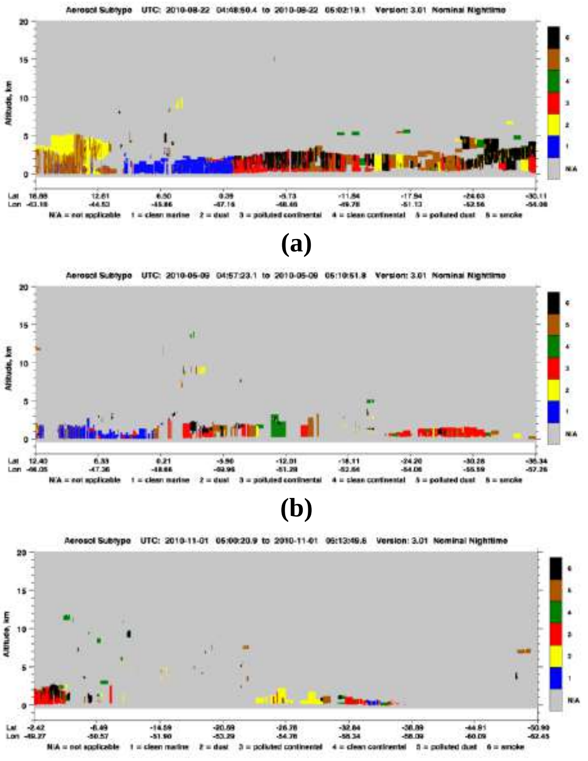

Figure 3. Aerosol Subtype by CALIOP sensor for 08/22/2010(a), 09/05/2010 (b) and 11/01/2010 (c)

CONCLUSIONS

The study area, as well as other regions that are not known large emitters of aerosol lack studies on the spatial-temporal variability of aerosols, not considering the importance of the advection of these aerosols from other regions. It is believed that this work can contribute directly to these issues, especially in the Southern region of Brazil due to the likely influence of several major known sources of aerosols: fires in the Amazon and the Brazilian savanna, anthropogenic aerosols in metropolitan areas of São Paulo, Rio de Janeiro, among others.

The information obtained may also contribute to atmospheric modeling, because of the greater understanding of aerosol-solar radiation interaction on the region, and thus provide a basis for improvement of numerical models for weather forecasts, climate and air quality.

ACKNOWLEDGMENTS

The authors would like to thank the Research Foundation of the State of Rio Grande do Sul (FAPERGS) for the approval of the project for this study. To the post-graduate program in Meteorology at the Federal University of Pelotas and the WLMLA organizing committee for their support for the participation on the event.

REFERENCES

BARNES, W.L., T. S. PAGANO, E V.V. SALOMONSON. Prelaunch characteristics of the Moderate Resolution Imaging Spectroradiometer (MODIS) on EOS-AM1. IEEE Trans. Geosci. Remote Sensing, vol. 36, p. 1088–1100, 1998.

FREITAS, S.R.; LONGO, K.; SILVA DIAS, M.A.; SILVA DIAS, P.L; CHATFIELD, R.; FAZENDA, A.;RODRIGUES, L.F. The Coupled aerosol and tracer transport model to the brasilian developments on the regional atmospheric modeling system: Validation using direct and remote sensing observations. Proceedings of 8 ICSHMO, Foz do Iguaçu, Brazil, April 24-28, p. 101-107, 2006.

LANDULFO, E. ; LOPES, F. J. ; MARIANO, G. L. ; TORRES, A.S. ; JESUS, W.C. ; NAKAEMA, W. M. ; JORGE, M.P.P.M ; MARANI, R.L. . Study of the Properties of Aerosols and the Air Quality Index Using a Backscatter Lidar System and Aeronet Sunphotometer in the City of São Paulo, Brazil. Journal of the Air and Waste Management Association, v. 60, p. 1, 2010.

MARIANO, G.L. ; LOPES, F. J. ; STEFFENS, J. ; MARTINS, M.P.P. ; LANDULFO, E. ; HELD, G. ; ANJOS, S. . Aerosols Monitoring in Rio Claro, Brazil: Using LIDAR and Air Pollution Analyzers. Optica Pura y Aplicada, v. 44, p. 55-64, 2011.

MARIANO, G.L. ; LOPES, F.J.S. ; JORGE, M.P.P.M. ; LANDULFO, E. . Assessment of biomass burnings activity with the synergy of sunphotometric and LIDAR measurements in São Paulo, Brazil. Atmospheric Research (Print), v. 98, p. 486-499, 2010a.

MARIANO, G.L. Efeitos das queimadas na atmosfera do estado de São Paulo – Análise de fontes próximas e distantes através de Lidar. Tese (doutorado em Meteorologia). Instituto Nacional de Pesquisas Espaciais, São José dos Campos-SP, 2010b.

SEINFELD, J.H.; PANDIS, S.N. Atmospheric Chemistry and Physics: From Air Pollution to Climate Change. New York: John Wiley & Sons, Inc., 1360p. 1998.

REVISTA BOLIVIANA DE FÍSICA 20s, 24-26, 2011
ISSN 1562-3823. INDEXADA EN: SCIELO, LATINDEX, PERIÓDICA

Raman Lidar monitors emissions from sugar cane fires in the State of São Paulo: A Pilot-Project integrating Radar, Sodar, Aerosol and Gas observations

G. Held[1], F.J.S. Lopes[2], J.M. Bassan[1], J.T. Nery[3], A.A. Cardoso[4], A.M. Gomes[1], T. Ramires[3], B.R.O. Lima[5], A.G. Allen[4], L.C. da Silva[4], M.L. Souza[4], K.F. de Souza[6], L.R.F. Carvalho[6], R.C. Urban[7], E. Landulfo[2], A.M. de Decco[1], M.L.A.A. Campos[7], M.E.Q. Nassur[7], R.F.P. Nogueira[4]
[1] Instituto de Pesquisas Meteorológicos, UNESP, Bauru, S.P., Brazil
Tel: +55 14 3103-6030, Fax: +55 14 3203-3649, E-nail: gerhard@ipmet.unesp.br
[2] Centro de Lasers e Aplicações, IPEN/CNEN, São Paulo, S.P., Brazil
[3] Campus Experimental de Ourinhos, UNESP, Ourinhos, S.P., Btazil
[4] Instituto de Química, UNESP, Araraquara, S.P., Brazil
[5] Instituto de Geociências, Unicamp, Campinas, S.P., Brazil
[6] Instituto de Química, USP, São Paulo, S.P., Brazil
[7] Departemento de Química, USP, Riberão Preto, S.P., Brazil

SUMMARY

Ourinhos is situated in one of the major sugar cane producing regions in the State of São Paulo, where the manual harvesting is generally preceded by burning the foliage, resulting in large quantities of aerosols being emitted into the atmosphere. A one-month pilot study was executed during August 2010, to characterize the effects of those emissions on the atmosphere, considering the local circulation and the consequences for the region. The plumes were tracked by IPMet´s two S-band Doppler radars, also deploying a large range of meteorological, physical and chemistry instrumentation: a mobile Lidar with Raman channel to observe elevated layers and the type of aerosols, a medium-sized Sodar, as well as 6 Automatic Weather Stations spread through town. Various gases and particulates were also sampled, providing the atmospheric chemistry data base and thus documenting the impact on the region.

This paper highlights a case study on 26 August, when a plume was tracked by TITAN Radar Software from the start of the fire, moving southwards at 14-17 km.h^{-1} with the winds at about 3,5 km above ground level, until it reached Ourinhos 2h15min later, where it was observed by the Raman Lidar and also detected by the aerosol and gas samplers. The high aerosol load of the atmosphere was confirmed by hourly mean values of AOD varying between 0,265 and 0,288 until 07:00 LT, after which they increased to 0,433 by 09:00 LT, as well as hourly mean backscatter profiles. Hourly values of the Lidar Ratio identified the aerosols as biomass burning products, also confirmed through the analysis of gas and aerosol samples simultaneously collected at the Lidar site.

Key words: Raman Lidar, biomass fire plumes, Doppler Radars, Sodar, Aerosol & Gas Sampling

INTRODUCTION

Ourinhos is situated in one of the major sugar cane producing regions in the State of São Paulo, where the sugar cane is harvested from April until November. Sectors of the plantations are generally burnt prior to manual harvesting. This practice results in large quantities of aerosols being emitted into the atmosphere, not only negatively affecting local towns, but also regions much further away (Held *et al.*, 2011). A one-month pilot study was executed during August 2010, to characterize the effects of those emissions on the atmosphere, considering the local circulation and the consequences for the region. In the absence of rain during the dry winter season, the plumes were tracked by IPMet´s two S-band Doppler radars, also deploying meteorological, physical and chemistry instrumentation: a mobile Lidar with Raman channel to observe elevated layers and the type of aerosols, a medium-sized Sodar, as well as 6 Automatic Weather Stations spread through town. Gases and particulates were also sampled, providing the atmospheric chemistry data base and thus documenting the impact on the region.

METHOD AND RESULTS

The region of Ourinhos was chosen, because the local Campus of UNESP (Universidade Estadual Paulista) maintains a network of 6 Automatic Weather Stations (plus one from INMET, the National Meteorological Institute), and it falls within the 100-120 km range of IPMet´s radar in Bauru (Figure 1), facilitating the tracking and quantitative analysis of such plumes in real time.

Figure 1. IPMet's radars with their quantitative range.

Instrumentation

The Lidar, Sodar, radiosonde and air quality monitoring equipment (particulate samplers and active gas monitors) were all installed at the UNESP Campus in Ourinhos on the north-western outskirts of town (448 m above mean sea level - amsl), as well as the Automatic Weather Station (AWS) of INMET.

The mobile bi-axial Raman Lidar system uses a commercial pulsed Nd:YAG laser, operating at a wavelength of 532 nm, with a pulse energy of 130 mJ at 20 Hz PRF. The pulse width is 25 ns, yielding a spatial resolution of 7,5 m. A detailed description of the system is found in Landulfo *et al.* (2010). The system allows the determination of the optical properties of the atmosphere, like Backscatter Coefficient, Coefficient of Extinction (quantification of aerosol loading of the atmosphere) and the Lidar Ratio (indication of types of aerosols).

The vertical range of the Sodar was set at 800 m above ground level (AGL), with a vertical resolution of 10 m and sampling intervals of 60 min averaged every 30 min on a sliding scale. The products generated are horizontal wind speed & direction, vertical wind velocity, as well as by inference the estimated height of the thermal inversion.

IPMet's radars cover the central and western State of São Paulo (Figure 1). Both have a 2° beam width and a quantitative range of 240 km, generating a volume-scan every 7,5 minutes, with a resolution of 250 m radially and 1° in azimuth, recording reflectivities and radial velocities at 16 elevations. However, in order to register and track the *queimadas*, a special scanning cycle was introduced to provide a better vertical resolution up to the anticipated detectable top of the plumes: 10,0°; 8,0°; 6,5°; 5,0°; 4,0°; 3,2°; 2,4°; 1,6°; 0,8°; 0,3°, with each "sweep" (PPI) having 360 rays with 957 range bins each. Two different systems of Software were deployed, *viz.* IRIS (*Interactive Radar Information System*) Analysis, to first generate CAPPIs (*Constant Altitude PPIs*) at 1,5 and 2,0 km amsl in order to identify all *queimadas* within the 240 km range of the radars. Once a *queimada* was identified to pass over the monitoring site, it was tracked by the TITAN (Thunderstorm Identification, Tracking, Analysis and Nowcasting; Dixon and Wiener, 1993) Software to determine its intensity (based on radar reflectivity in dBZ), horizontal and vertical dimensions, and the velocity of approach. The thresholds used for tracking were 10 dBZ with a minimum volume of 2 km^3. It should be noted, that TITAN uses Universal Time (Local Time LT = UT-3h).

Since it is extremely important for the population in the Region to characterize the air quality, some gases (NO$_2$, SO$_2$, O$_3$, Aldehydes) monitored and soluble aerosols sampled in different size fractions, including elementary carbon, during different periods of the day (10:00-16:00 and 20:00-06:00 LT), and also Polycyclic Aromatic Hydrocarbons (HPA). Ion chromatographic analysis would allow the identification of possible sources, especially biomass burning products, like Potassium (K$^+$) and water-soluble organic carbon (WSOC).

Case Study of 25-26 August 2010

Based on a synoptic analysis for the Ourinhos Region, the month of August can be divided into two distinct periods, *viz.*, 01-15 August, when 3 cold fronts crossed the State, causing light rain and very low temperatures especially at the beginning of the month, while during the second half the weather was dominated by a high pressure system, resulting in the temperatures to rise, but with low humidity, favoring the accumulation of pollutants in the regional air. The case study from 25 to 26 August 2010 was characterized by exactly such conditions.

The first echo of a smoke plume was detected by the Bauru radar on 26 August 2010 at 00:08 LT, about 35 km north-north-east of Ourinhos and ca 85 km south-west of the radar, rapidly gaining in area and intensity (≤40 dBZ near its origin). By 00:22 LT, TITAN could already identify its centroid and tracked it until 02:45 LT, when the plume had already spread over Ourinhos. As the plume moved southwards with the northerly winds, the aerosols spread out (dispersed) and the reflectivity dropped gradually until 02:45 LT, but it could still be detected by the radar until 03:46 LT, >20 km south of Ourinhos, using a reflectivity threshold of -6 dBZ.

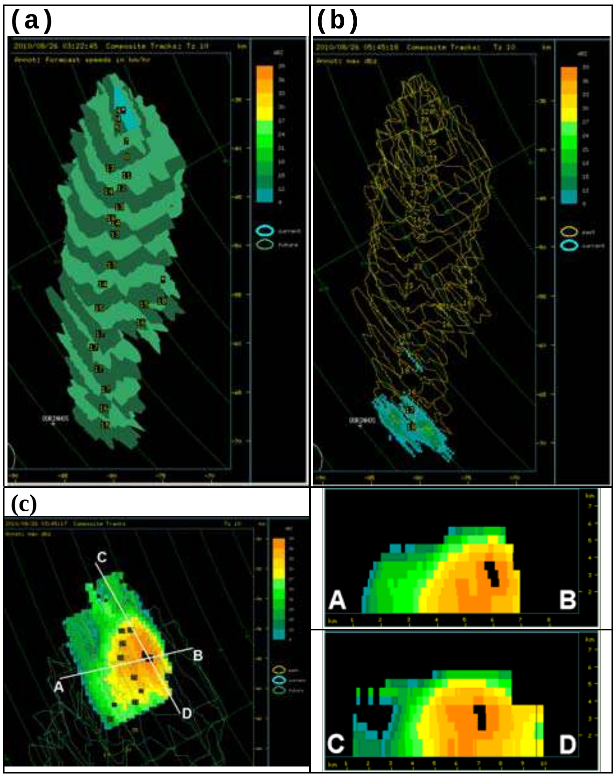

Figure 2: Tracks generated by TITAN on 26 August 2010. The envelopes (10 dBZ reflectivity) show the position of the *queimada* in intervals of 7,5 min (blue = actual time; green = future; yellow = past).

(a) First TITAN centroid of the *queimada* (fire) at 03:22UT (00:22LT; annotation: propagation velocity in km.h^{-1});

(b) The *queimada* reached the Ourinhos area at 05:45UT (02:45LT; annotation: max reflectivity in dBZ);

(c) Max-CAPPI and cross-sections, showing the horizontal and vertical extent along the base lines at 03:45UT.

Although during the night from 25 to 26 August, there were several other *queimadas* active and contributing to the overall aerosol load in the region, this study only concentrates on the history of the above plume, as illustrated by the TITAN-generated images in Figure 2.

Furthermore, it can be deduced from Figure 2a, that while the plume was at low heights at the beginning, it moved very slowly (3-4 km.h^{-1}) since the wind speed in the first few hundred meters was very low (≤5 m.s^{-1}), as observed by the Sodar. It also showed a shift of the wind direction from easterly to northerly winds >300 m AGL. These northerly winds were above the nocturnal surface inversion and are confirmed by the "Skew T x Log P" profiles of the Meso-Eta Model in the layer 900-800 hPa (650–1650 m AGL). The vertical velocity w indicated that downward mixing of the pollutants (aerosols), trapped above the inversion, only commenced at around 09:00 - 09:30 LT, since from 00-06 LT and from 06-09:00 LT the atmosphere was extremely stable below 300 m AGL ($w = \pm 0$ m.s^{-1}).

The Lidar was operating continuously from 25/08/2010 to 27/08/2010, also recording the Raman Channel during the night. Considering the radar images in Figure 2, the *queimada* arrived over the municipal area of Ourinhos between 02:30 and 02:45 LT. Figure 3 visualizes the Lidar observation between 00:00 and 06:00 LT up to a height of 3 km AGL. The arrival of the *queimada* aloft is marked with an arrow. Furthermore, a distinct cut-off at ca 2,6 km AGL is visible, which coincides with the top of the Planetary Boundary Layer, above which a very dry and relative warm and clean air was advected from the west above ca 730 hPa, creating an elevated inversion which blocked further upward mixing. The lowest layer ≤250 m AGL appears clean, being trapped within the surface inversion, which inhibits downward mixing, also confirmed by the Sodar measurements, indicating a very stable layer. Above it, during the first hours of the day, regional remnants of aerosols are observed, until the plume arrived at 02:40 LT between 350 and 600 m AGL, being transported by northerly winds.

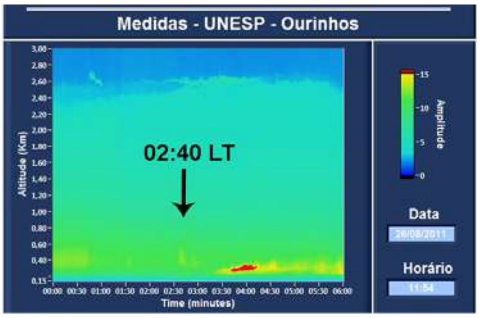

Figure 3. LIDAR signal (arbitrary units) visualized from 00:00-06:00 LT up to 3 km AGL.

A quantitative analysis of the Lidar observations was performed by first integrating the data from the Raman Channel (non-elastic signal at 607 nm) into hourly means until 09:00LT to obtain the Aerosol Optical Depth (AOD). The results confirmed a high aerosol load of the atmosphere, with hourly mean values of AOD varying between 0,265 and 0,288 until 07:00LT, thereafter increasing to 0,433 by 09:00 LT.

Backscatter Profiles at 532 nm were generated for every hourly integrated period, showing an aerosol load up to about 2,6 km AGL. The first Backscatter profiles (00:00-02:59 LT) represent the regional pollution load, while from 03:00 LT onwards, a specific plume (as identified by TITAN, Figure 2) arrived at Ourinhos above the temperature inversion. Thereafter, the Backscatter Signal peak gradually increased from 0,003 to 0,004 km^{-1}.sr^{-1} at 03:40-04:20 LT, with a further increase to 0,0056 km^{-1}.sr^{-1} by 11:00 LT, after which the peak of the Backscatter Signal is decreasing due to turbulent mixing of the atmosphere.

Hourly means of the Lidar Ratio show an increase during the period 02:00-02:59 LT, confirming the arrival of the *queimada* from the north, while an almost 20% increase to 72 sr after 07:00 LT is probably due to downward mixing of the nocturnal *queimadas*, also confirmed by an increase of AOD values from the Raman signal. According to Catrall *et al.* (2005), aerosols originating from biomass burning have LR values between 59 and 70 sr. Omar *et al.* (2009) also suggest LR values of around 70 sr for biomass aerosols. Following these suggested values, the LR calculated for the observations on 26 August 2010 are most likely due to aerosols generated during biomass fires in the region.

CONCLUSIONS

In conclusion, it can be confirmed, that the smoke plume emitted by a sugar cane fire, observed by IPMet´s Bauru radar and tracked with the TITAN Software did reach the municipal area of Ourinhos during the early hours of the morning of 26 August 2010, and was also registered by the Lidar in a layer above 350 m AGL, but was initially prevented from mixing downwards by the very stable atmospheric conditions, as implied by low aerosol concentrations collected during the nocturnal period 22:00 – 06:00 LT. However, the chemical analyses (10:00 – 16:00 LT), as well as the Lidar parameters, pointed at daytime downward mixing of the suspended aerosols, as soon as the stable Boundary Layer conditions were eroded by increasing daytime temperatures. This, in turn, would directly result in a negative impact on the health and well-being of the population in that region. Relatively high background concentrations of aerosols observed at the monitoring site indicate an accumulation of pollutants during prolonged periods of stable atmospheric conditions, being responsible for respiratory problems of the population due to the very fine particulate matter in suspension.

ACKNOWLEDGMENTS

FUNDUNESP is thanked for support to conduct the collection of meteorological and Lidar data during this Pilot Campaign (Processo 00598/10-DFP) and to present the paper. The chemical sampling was done by participants of FAPESP Project "Effects of emissions on current and future rainfall patterns in Southeast Brazil" (Processo No. 2008/58073-5).

REFERENCES

Cattrall C, Reagan J, Thome K and Dubovik O, 2005. Varia-bility of aerosol and spectral lidar and backscatter and extinction ratios of key aerosol types derived from selected Aerosol Robotic Network locations, *Journal of Geophysical Research*, **110**, D10S11.

Dixon M and Wiener G, 1993. TITAN: Thunderstorm Identi-fication, Tracking, Analysis & Nowcasting - A radar-based methodology, *J. Atmos. Oceanic Technol*., **10**, 785-797.

Held G, Landulfo E, Lopes FS, Arteta J, Marecal V and Bassan JM, 2011. Emissions from sugar cane fires in the central & western State of São Paulo and aerosol layers over Metropolitan São Paulo observed by IPEN´s lidar: Is there a connection? *Opt.Pura. Apl.*, **44** (1), 83-91.

Landulfo E, Jorge MP, Held G, Guardani R, Steffens J, Pinto SdAF, Andre IR, Garcia A G, Lopes FJS, Mariano GL, da Costa RF and Rodrigues PF, 2010. Lidar observation campaign of sugar cane fires and industrial emissions in the State of São Paulo, Brazil. *SPIE Digital Library, Proc. SPIE,* Vol. **7832**, 783201 (2010), 8pp; doi: 10.1117/12.866078.

Omar AH, Winker DM, Kittaka C, Vaughan MA, Liu Z, Hu Y, Trepte CR, Rogers RR, Ferrare RA, Lee KP, Kuehn RE and Hostetler CA, 2009. The CALIPSO Automated Aerosol Classification and Lidar Ratio Selection Algorithm, *Journal of Atmospheric and Oceanic Technology*, **26**, 1994-2014.

REVISTA BOLIVIANA DE FÍSICA 20s, 27-29, 2011
ISSN 1562-3823. INDEXADA EN: SCIELO, LATINDEX, PERIÓDICA

Comparison of AOD measurements and forecasts of Saharan dust events at Camagüey, Cuba.

Juan Carlos Antuña(1), Victoria Cachorro(2), René Estevan(1), Ángel de Frutos(2), Boris Barja(1), Yasmine Benouna(2), Benjamín Torres(2), David Fuertes(2), Ramiro González(2),Carlos Toledano(2), George Kallos(3) and Spyrou Christos(3)

(1)Grupo de Óptica Atmosférica de Camagüey, Centro Meteorológico de Camagüey, Camagüey, Cuba
(2)Grupo de Óptica Atmosférica, Universidad de Valladolid, España
(3)Department of Applied Physics, University of Athens, Greece

E-mail: anadelia@caonao.cu

SUMMARY

The SKIRON model AOD forecasts for Saharan dust clouds arriving to Camagüey, Cuba, during July 2009 were evaluated. For such a goal AOD measurements from a surface sunphotometer were used. Additional information from MODIS was also available for the comparison. The results demonstrate the capabilities for developing an alert and tracking system for Saharan dust events across the Atlantic.

Key words: Saharan dust, aerosols, AOD, SKIRON model

INTRODUCTION

Recent studies using state of the art satellite information showed that every year 240 ± 80 Tg of dust are transported from Africa in the latitude band 20°S – 30°N. From that amount 50 ± 15 Tg are deposited in the Amazon basin and 50 ± 25 Tg arrive to the Caribbean (Kaufman et al., 2005). Those enormous amounts of aerosols have an important impact in human activities

The GOAC team, in cooperation with scientists from several institutions is developing a service for alert-tracking the Saharan dust transported over the Atlantic to the Wider Caribbean. The core idea of the service is to provide, to each one of the countries of the Wider Caribbean local notices of the future arrival of Saharan dust to his area combined with updates of the current position of the dust air masses. It will combine existing numerical modelling of the Saharan dust transport with satellite and surface observations. Those sources of information are the SKIRON model AOD forecasts, the derived AOD from MODIS (both from Terra and Aqua) and the derived sun photometer AOD. The purpose of the present comparison is to have a preliminary estimation of the magnitudes of the differences between the AOD sun-photometer measurements at Camagüey and the coincident AOD forecasted by SKIRON in the presence of several Saharan dust events.

DATASETS

The sun photometer CIMEL CE-318 installed at the Camagüey (21.42º N, 77.84º W, 128 meters over sea level) is part of the Iberian Network for Aerosol Measurements (RIMA) which is federated into the Aerosol Robotic Network (AERONET). It was installed as result of a cooperation agreement for joint aerosol research between the University of Valladolid (UVA), Spain, and the Cuban Meteorological Institute (INSMET). The research are conducted by the Grupo de Óptica Atmosférica (GOA-UVA) and the Grupo de Óptica Atmosférica de Camagüey (GOAC-INSMET), formerly the Camagüey Lidar Station. The sun-photometer was operative from October 7th 2008. After the post calibration of the CIMEL # 353 and the reprocessing of the dataset the produced AOD by AERONET Version 2.0 showed very little changes with respect to the Version 1.5.

From the total of 746 instantaneous AOD measurements that passed the quality control and were processed in the Version 1.5 for the entire month of July 2009, only 11 did not passed the quality control required for version 2.0, representing only the 1.5% of the observations reported before. The rest of the AOD values (98.5%) did not changed in the Version 2.0 with respect to the Version 1.5. Table 1 lists the day's data has been discarded in Version 2.0 and its effects respect to Version 1.5.

Table No. 1: Daily distribution and observed effect on the AOD values of discarded observations per day in Version 2.0 with respect to Version 1.5. Period July 1st to 31st 2009.

Day	# Obs.	Observed effect on Version 2.0 AOD
2	1	Daily Mean AOD decrease in 0.0089
3	5	No AOD values for that day
10	2	No AOD values for that day
11	3	Daily Mean AOD decrease in 0.0726

Saharan dust events were measured by first time with the sun-photometer installed at Camagüey, Cuba, in July 2009.

Those had been already studied [*Estevan et al.,* 2011]. We selected that period of time because of the presence of several events in the course of the month

The SKIROM model has been operational for more than 10 years. Recently a new upgraded version has been released (Kallos et al., 2009). For the present comparison we have used the SKIRON griddled (0.1° x 0.1°) daily hourly forecasts of AOD at 500 nm, from July 1^{st} to 31^{st}, 2009. For the purposes of the comparison we selected the AOD values in the area of 0.5º x 0.5º around the Camagüey sunphotometer site. That grid box covers and area of 2874.5 km^2. (ΔX = 51.7 km and ΔY = 55.6 km).

RESULTS AND DISCUSION

Camagüey AOD measurements

The Camagüey AOD dataset (Version 2.0) for July 2009 consists of 735 instantaneous measurements. The data was processed attending to three different criteria:

1. Hourly mean AOD **(H-AODCMG):** For each hour, each day the mean AOD value was calculated, resulting in 239 H-**AODCMG** values.
2. Daily mean AOD **(D-AODCMG):** For each day the mean AOD value was calculated, resulting 29 **D-AODCMG** values.
3. Daily maximum **AOD (DMx-AODCMG):** For each day the maximum AOD value was calculated, resulting in 29 AOD{max} values. Also the time of the occurrence of the **DMx-AODCMG** values were registered.

The figure 1 depicts on the top panel the set of instantaneous measurements for the whole period of study (black dots). In the middle panel appear the hourly mean values. In the bottom daily means and maximum are plotted.

SKIRON forecasts dataset:

Different magnitudes of the AOD were calculated:

1. Hourly mean AOD (**H-AODSK**): Average of the AOD over the selected grid box for each one of the 24 hours each day. (744 values)
2. Hourly maximum AOD (**HMx-AODSK**): Maximum value of the AOD over the selected grid box for each one of the 24 hours each day. (744 values)
3. Daily means AOD (**D-AODSK**): Average of the AOD over the selected grid box and over the 24 hours each day. (31 values)
4. Daily coincident maximum AOD (**DMx-AODSK**): Maximum value of the forecasted AOD over the selected grid box for each one of the 24 hours each day for the same hour the daily maximum AOD at Camagüey was registered. (31 VALUES)

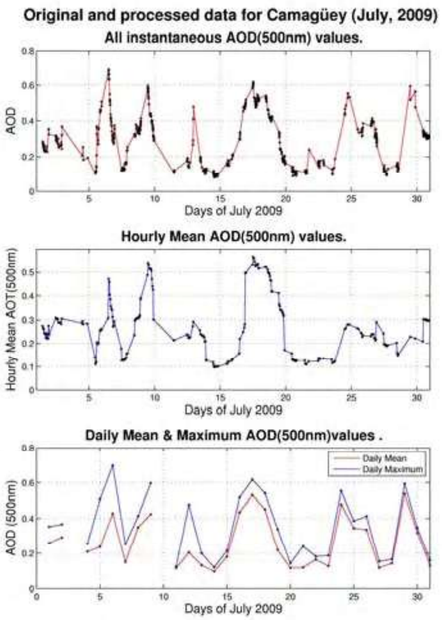

Figure 1. Results of the processing of AOD sun-photometer measurements at Camagüey.

Comparison

The figure 2 shows the differences between the hourly mean AOD measured at Camagüey (**H-AODCMG**) by sunphotometer and the hourly mean AOD (**H-AODSK**) forecasted by SKIRON. The last values were selected considering the values nearest in time to the hour the sunphotometer measurement was conducted (239 pair of values). Those differences are depicted in blue. For illustrative purposes the values of **H-AODCMG** are also plotted (green).

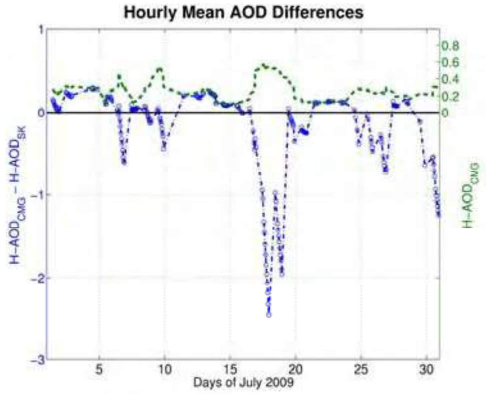

Figure 2: Hourly mean AOD differences.

The higher differences in figure 2 are associated with the maximum values of the AOD registered by sunphotometer at Camagüey caused by Saharan aerosols, all then negatives. This is a consequence of the Saharan aerosols AOD values forecasted by SKIRON being higher than the measured ones. In the cases of the lower AOD values measured, in absence of Saharan aerosols, the differences are mainly positive, revealing that in that case the AOD values forecasted by SKIRON being lower than the measured ones. In several cases the forecasted AOD values are very little, almost zero, producing differences of the same magnitude than the measured AOD. This feature is produced by the fact that SKIRON do not takes into account the background aerosols (and its corresponding AOD) produced by local sources.

Figure 3 shows the difference between the daily mean AOD measured (**D-AODCMG**) and the daily mean AOD forecasted by SKIRON (**D-AODSK**). In general there is a decrease of the differences, with less negative cases, but the main features discussed in figure 2 remain.

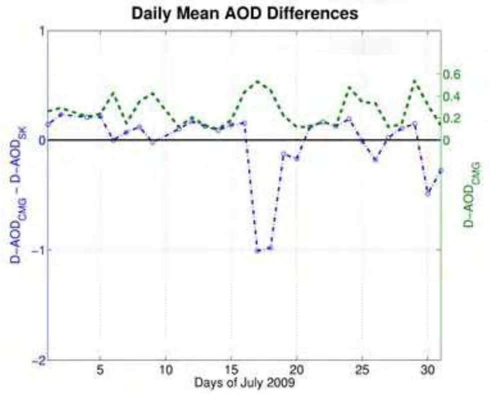

Figure 3: Daily mean AOD differences.

Figure 4 shows the difference between the measured daily maximum AOD (**DMx-AODCMG**) and the forecasted daily maximum AOD (**HMx-AODSK**). It resembles almost the same behavior that the hourly mean AOD differences in figure 2.

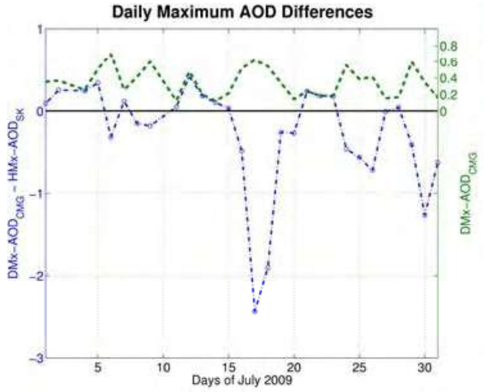

Figure 4: Daily maximum AOD differences.

In figure 5 is shown the plot of the differences between the daily maximum AOD measured (**DMx-AODCMG**) and the forecasted daily maximum AOD at the same hour the maximum AOD was registered (**DMx-AODSK**). The differences are in the same order of magnitude than the **DMx-AODCMG**, due to the fact that the **DMx-AODSK** has very low values.

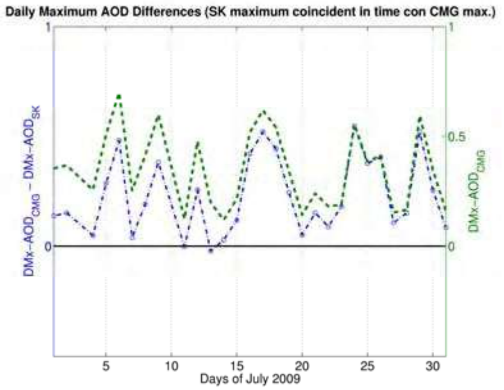

Figure 5: Daily maximum AOD differences. Forecasted AOD maximum determined at the same hour than the maximum measured AOD.

CONCLUSIONS

From the former results several preliminary conclusions have been obtained. The daily average values of the sunphotometer measured and modeled forecasted AOD show the better agreement, but still notable differences are present. The lack of background aerosols AOD in the forecast produces additional differences in the absence of Saharan dust. In the case of the long range transport of Saharan aerosols the forecasted AOD values are higher than the measured ones.

Current work is in progress to improve the comparisons and to conduct also comparisons with coincident MODIS AOD observations.

REFERENCES

Estevan, R., J. C. Antuña, B. Barja, V. E. Cachorro, Á. M. de Frutos, A. Berjón, C. Toledano, B. Torres, R. Rodrígo, T. A. Hernández y C. E. Hernández, 2011: Preliminary results of aerosols measurements with sun photometer at Camagüey, Cuba. Opt. Pura Apl., 44 (1), 99-106.

Kallos, G. C. Spyrou, M. Astitha, C. Mitsakou, S. Solomos, J. Kushta, I. Pytharoulis, P. Katsafados, E. Mavromatidis, N. Papantoniou and G. Vlastou, 2009: Ten-year operational dust forecasting - Recent model development and future plans. IOP Conf. Series: Earth and Environmental Science, 7, 012012, doi:10.1088/1755-1307/7/1/012012.

Kaufman, Y. J., Koren, I., Remer, L. A., Tanr´e, D., Ginoux, P., and Fan, S., 2005: Dust transport and deposition observed from the Terra-Moderate Resolution Imaging Spectroradiometer (MODIS) spacecraft over the Atlantic Ocean, J. Geophys. Res., 110, D10S12, doi:10.1029/2003JD004436.

REVISTA BOLIVIANA DE FÍSICA 20s, 30-32, 2011
ISSN 1562-3823. INDEXADA EN: SCIELO, LATINDEX, PERIÓDICA

Remote control and telescope auto-alignment system for multiangle lidar under development at CEILAP, Argentina

Juan V. Pallotta, Pablo Ristori, Lidia Otero, Francisco Gonzalez, Juan Carlos Dworniczak, Raul D'Elia, Ezequiel Pawelko, Eduardo Quel.
CEILAP (CITEDEF-CONICET), UMI-IFAECI-CNRS 3351
Juan B. de La Salle 4397, B1603ALO Villa Martelli – Buenos Aires, Argentina.
E-mail: jpallotta@citedef.gob.ar
Alberto Etchegoyen
ITeDA (CNEA – CONICET - UNSAM)
Av. Gral. Paz 1499 - 1650 San Martín – Buenos Aires, Argentina.

SUMMARY

At CEILAP (CITEDEF-CONICET), a multiangle Raman lidar is under development to monitor aerosol extinction in the frame of the CTA (Cherenkov Telescope Array) Project. This is an initiative to build the next generation of ground-based instruments to collect very high energy gamma-ray radiation. It will serve as an open observatory for a wide astrophysics community and will explore the Universe in depth in Very High Energy (> 10 GeV) gamma-rays. The atmospheric conditions are is a major interest for CTA, and this instrument plays a major role measuring the atmospheric optical depth.

The reception system is made by six 40 cm in diameter Newtonian telescopes, totally exposed to the hard environmental condition during the shifts. These working conditions could produce misalignments between laser and telescopes, losing the required overlap. To avoid that, a telescope controlled by a self-alignment system is under development to solve this problem. This is performed by PC software running from the acquisition module which is connected via ethernet to a microcontroller. This paper, describes the self-alignment method and hardware work in progress.

Key words: multiangle lidar, Raman, CTA observatory, aerosols.

INTRODUCTION

The Cherenkov Telescope Array Consortium (CTA) contemplates the design, construction and the operation of two observatories for the detection of gamma-ray produced by extraterrestrial sources at energies range between 10^{10} eV to 10^{14} eV. These observatories will be deployed at each hemisphere for full sky-map coverage. Each Observatory will consist of a telescope array sensitive to the atmospheric generated Cherenkov radiation that will improve the performance of the actual detectors. The objectives proposed for CTA will be attained using an array of multiple telescopes distributed over a surface of 1 km^2, located at sites with excellent optical and atmospheric conditions at a height of 2000 to 3500 mts above the sea level. The comprehension of the atmospheric conditions during the measurements is extremely important for the CTA Observatory. In fact, the atmosphere acts as the first detector at which the air showers are developed. The array of detectors observe the gamma ray induced cascades by measuring the Cherenkov light produced by their charged particles moving above the speed of light of the surrounding atmosphere. The emitted light is attenuated from the source to the telescope due to molecular, aerosol and cloud extinction. Lidars play a leading role in monitoring of sky conditions, by both detecting the overall cloud coverage and measuring the atmospheric opacity due to aerosol and clouds over the Observatory. The location of this astronomical facility will be selected after a careful study of the preselected zones, regarding the latitude, altitude, the atmospheric conditions, and the available local infrastructure. At the Southern hemisphere, Argentina is one of the candidate countries for the installation of the CTA Observatory. The places proposed are "El Leoncito", located in San Juan state and "El CASLEO", in Salta.

LIDAR HARDWARE

LIDAR telescope is planned to be mounted on a steerable frame, and moved using two DC servomotors, reading its position by two relative encoders.

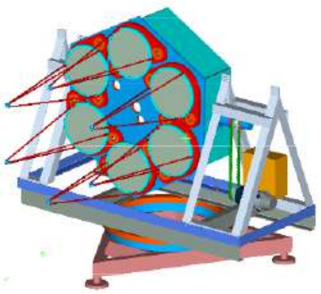

Figure 1. A preliminary sketch of the multiangle lidar under construction.

Movements are handled by a microcontroller that communicates with the lidar PC through an ethernet connection. Each LIDAR is equipped with a Nd:Yag laser, that generates laser pulses at 355, 532 and 1064 nm at a repetition rate of 50 Hz and a pulse energy of ~20 mJ @ 355 nm. The backscattered light is collected by six Newtonian telescopes with 40 cm diameter, 1 m focal length. A multiwavelength spectrometer separates the backscattered wavelengths and concentrates the light into several Hamamatsu H6780 photomultipliers. A Licel TR20-160 module is used to digitalize and store the lidar profiles

This lidar has special requirements:

- It has to be able to be operated remotely. The lidar operator may not have an a priori knowledge on lidar techniques.
- Telescopes, mechanics and electronics, will be exposed during nighttime to extreme environmental conditions (wind burst, temperature span, etc.), which could produce lidar misalignments

These are the main reasons that encourage the development of a fully automatic alignment system is to keep the telescopes aligned during the acquisition period.

LIDAR COMUNICATIONS

The lidar system under development has two operational modes: *local mode* and *remote mode*. *Local mode* was developed for maintenance procedures. The presence of a lidar technician is required on site to perform hardware improvements and specific tests. *Remote mode* was programmed to perform shift operations. In this case the lidar will be remotely operated and monitored from the control center. The lidar computer was designed to communicate with control center server wirelessly via a WiFi link, creating a local lidar network under the TCP/IP protocol.

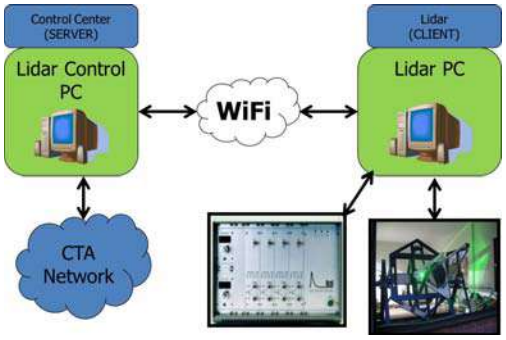

Figure 2. A general schematic layout of the lidar communication system. If remote mode is set, the shifter can monitor and control all the operations.

At the link endpoints, several processes communicate with each other to send/receive control and monitoring messages.

LIDAR SOFTWARE

A more detailed view of the process at each lidar PC can be seen on Figure 3. Each computer works under Linux operating system and all the software was developed in C/C++. A socket-based IPC (Inter Process Communication) was programed to communicate the local with the remote process. To increase their efficiency, each process is totally independent, and communicates to the other via control messages.

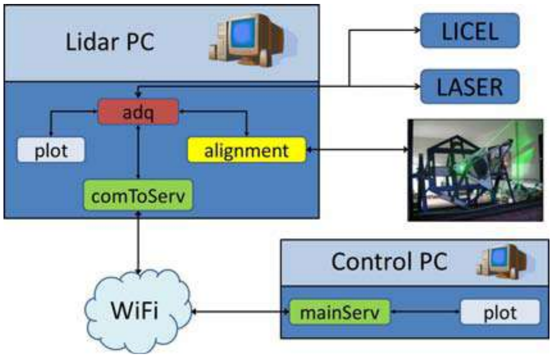

Figure 3. A general diagram about connections in both sides of the lidar system.

A brief description of each process at both sides of the link is described below:

Lidar PC side (client):
adq: Is the main process at the client (lidar) side. It controls the acquisition timing, it communicates with the laser, it triggers the Licel, it sends the acquired new file to the *plot* process, and, if necessary, to the *alignment* process.
plot: Waits messages from the *adq* process, conformed mainly by the new acquired file path and shows it on the display.
comToServ: This process handle all the messages from/to the client/server side.
alignment: This process receive the path to the acquired file from *adq* and process this signal to obtain the alignment parameters to determine the telescope position.
Control PC side (server):
mainServ: Handle the communication between the shifter and the client PC.
plot: Shows the lidar signal from the last saved file.

MICROCONTROLLER-CONTROLLED TELESCOPES

The tilt angle of the telescopes is driven by a set of stepper motors, handled by a RCM2200 Rabbit System microcontroller. This is Z80 family-based high-performance 8 bit microcontroller. It has a built-in Ethernet interface with an integrated TCP/IP stack, making it a good choice for interconnectivity. This interface is used to link the microcontroller with the lidar PC. The instruction set is based on the original Z80 microprocessor, with some additional instructions.
The aims of the Rabbit microcontroller algorithm is to decode the Ethernet information received from the lidar PC *alignment* process, and to handle the signals to correct the stepper motor drivers. The message from the lidar PC to the Rabbit microcontroller has 3 parameters: motor to be controlled, direction and number of steps. Therefore, the firmware of the Rabbit microcontroller is a “dummy terminal” that only receives message and drives the motor. After that, it sends an acknowledge message back to the *alignment* process.

ALIGNMENT ALGORITHM

The alignment algorithm is a cooperative procedure between the *adq* and the *alignment* processes, both running on the lidar PC, and a firmware recorded in the Rabbit microcontroller.
When the alignment mode is set at the *adq* process, each path of the acquired file is sent to *alignment*. Moreover, after

saving a new file at the lidar PC, this file is transferred to the control PC for a backup. A summarized procedure flowchart can be seen on Figure 5.

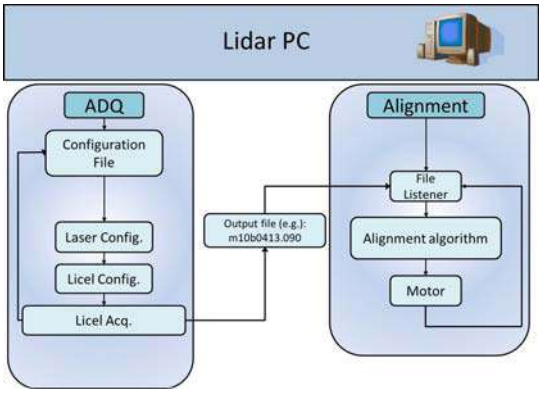

Figure 4. Communication Diagram between the *acquisition* and the *alignment* processes. Both are fully independent, and they communicate via the IPC socket, implemented under C/C++.

The aim of the alignment algorithm is to quantify the alignment state of the recently acquired file and to save it with its tilt position in a table. After that, *alignment* tilts the telescope to a new position and sends an acknowledge message to *acq*, to trigger new acquisition.

The alignment state quantification is obtained by accumulating the lidar signal over certain range, as it seen on the next figure:

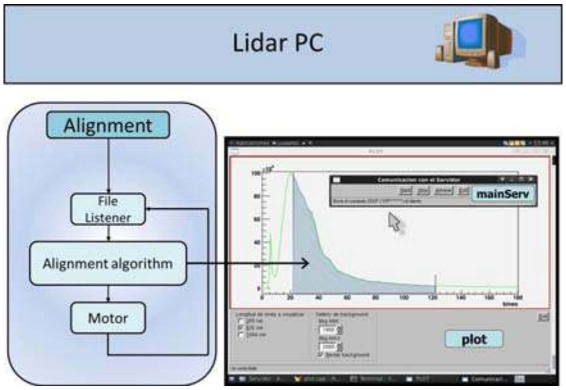

Figure 5.

After finishing the scanning process, the microcontroller sets the telescope position to the one at wich the maximum value was attained. This procedure tends to increase the lidar signal in a wide dynamic range.

FIRST RESULTS

This algorithm was successfully tested, comparing the vertical lidar signals obtained with the ones obtained by the MWRL lidar at CEILAP (CITEDEF-CONICET). The test was done for a vertical fixed position, as can be seen on Figure 4.

The CEILAP's telescope was manually aligned to provide the reference signal. The tested telescope was left intentionally misaligned to test the optimization algorithm.

Figure 4. Picture of the setup of lidar intercomparison.

After turning on the alignment mode, the algorithm exhibited good results, approaching the telescope's signal under test to the reference lidar signal. The next figure shows the lidar signals after the alignment process.

Figure 5. Picture of the lidar signals intercomparison after alignment algorithm success.

The differences seen on the last figure are due to the different distance to the laser source of the systems. Figure 5 shows the long range agreement of the signals.

CONCLUSIONS

The system is ready to be tested in a slant path fixed angle. The lidar is actually being installed inside a container to perform this new test. A new enhanced version of the controlled telescope actuators is under construction. First measurements indicate that it will be possible to achieve the expected auto-optimizations goals during the scanning procedure. The new software for a multiangle lidar prototype is fully operational.

ACKNOWLEDGMENTS

Authors wish to thank JICA, ANCyPT, the CITEFA main workshop's technicians and José Luis Luque from the CEILAP workshop for their support on this development.

REFERENCES

Otero, L. A. *et al.* (2004). First Aerosol Measurements with a Multiwavelength LIDAR System at Buenos Aires, Argentina Proceedings of the Conference of the ILRC2004.

http://www.digi.com/
http://www.cta-observatory.com/,
http://astrum.frm.utn.edu.ar/CTA-Argentina/
Licel programing examples and documentation: http://www.licel.com/soft_tcp.html

REVISTA BOLIVIANA DE FÍSICA 20s, 33-35, 2011
ISSN 1562-3823. INDEXADA EN: SCIELO, LATINDEX, PERIÓDICA

Rayleigh lidar temperature profiles between 15 - 60 km during OZITOS campaign in Río Gallegos (51° 55'S, 69° 14'W), Argentina

Salvador, J., Wolfram, E., Orte, F., Bulnes D., D'Elia, R., Quel, E.
CEILAP (CITEDEF-CONICET), UMI-IFAECI-CNRS 3351, Juan B. de La Salle 4397, B1603ALO Villa Martelli, Argentina.
Tel: +54-02966-15655090, E-mail: jsalvador@citedef.gob.ar
Zamorano, F., Casiccia, C.
Universidad de Magallanes (UMAG),
Punta Arenas, Chile

SUMMARY

The determination of temperature measurements from the Rayleigh scattering is an important remote sensing technique for obtaining stratospheric profiles. This technique is applied to signals acquired by a Rayleigh lidar (Light Detection and Ranging). Currently the Observatorio Atmosférico de la Patagonia Austral (51° 55'S, 69° 14'W) in Río Gallegos, Argentina is part of the UVO3Patagonia project in collaboration with the laboratory of Ozone and UV Radiation in the city of Punta Arenas, Chile distant 200 km, for more information www.uvo3patagonia.com. In this paper we showed the technique to measure temperature profiles in the stratosphere between 15-60 km altitude. We compared the temperature profiles obtained of the second ozone sounding campaign called OZITOS (**OZ**one profi**l**e a**T** Rí**O** Galleg**OS**) carried out in March 2011 in Río Gallegos with the temperature profile retrieved by the Rayleigh lidar using the line of 355 nm, in the same period. The results presented in this paper are validated through intercomparisons with measurements made by MLS instrument (Microwave Limb Sounder) onboard the NASA AURA satellite platform and NCEP data.

Key words: Rayleigh lidar, temperature profile, radiosounding measurements

INTRODUCTION

The lidar emerged as a powerful technique for the remote sensing of the atmosphere. The Rayleigh scattering due to air molecules has been widely used over the past 20 years to determine the temperature profile of the atmosphere between 30 and 90 km altitude. This method allows to study the dynamics of the middle atmosphere with high vertical resolution and temporal evolution. The extension of this technique to the lower atmosphere below 30 km is limited by aerosol scattering, ozone absorption, and dense atmospheric attenuation. To overcome these difficulties, the wavelength dependent non-elastic Raman scattering technique has been employed recently (Gross *et al.,* 1997) (Gu *et al.,* 1997) (Nedeljkovic *et al.,* 1993). However, Raman lidar requires a high-power laser transmitter to improve the low-level signal conditions because the Raman scattering cross section is about 3 orders of magnitude smaller than that of the Rayleigh scattering. Balloon borne instruments, rocket sounding, and satellite observations have been the main sources of information of this region. However, these datasets show many discrepancies and contain deficiencies due to poor vertical resolution and discontinuities. In this respect, the use of lidar, complements the other techniques, since the unique feature of lidar is its capability to make measurements of a number of important atmospheric parameters with excellent space and time resolution.

Since 2007, CEILAP group has installed the Observatorio Atmosférico de la Patagonia Austral. Actually we have a binational project with the laboratory of ozone and UV radiation (LabO_3RUV) from Magallanes's University called UVO3 Patagonia, supported by Japanese Cooperation Agency (JICA). Both groups are specialized in measured the depletion ozone using differents techniques. In CEILAP group basically can obtain ozone profile using a DIAL system described (Wolfram *et al.,* 2008). The LabO_3RUV measured using ECC balloon sonde (Electrochemical Concentration Cell), developed by Komhyr (Komhyr 1969, 1971).

The final objective of this paper is to do an introduction to temperature profiles using a Rayleigh lidar which will be describe below. Also a campaign of ozonesounding made in Río Gallegos in March 2011, called OZITOS II (OZone profile aT RíO GallegOS) will be used to compare temperature profiles between 10 up to 32 km.

The analysis that we will make below is important to know since the campaign OZITOS II was principally designed for the validation of ozone profile. This paper try to use the temperature from radiosounding aboard the balloon sonde to compare the temperature profile obtained by the Rayleigh lidar temperature, and this way increase the capability of the instrument. Also we use the data from the National Centers for Environmental Prediction (NCEP) and the MLS instrument aboard satellite AURA-NASA (Acker and Leptoukh, 2007).

METHODOLOGY

The methodologies described in this section were separated in two parts: the first one describe how obtain a temperature profile from a Rayleigh lidar as a part of the DIAL system. The second one, tried describe the sensor used for the validation of temperature profile from Rayleigh lidar.

Rayleigh lidar temperature profiles

Lidar temperature measurements require that only molecular Rayleigh scattering contributes to the return signal and Mie scattering from aerosols is negligible. This is usually the case above 30 km, even after a volcanic eruption such as Mt. Pinatubo (Steinbrecht and Carswell, 1995). When the Mie scattering is not negligible which occurs typically below 30 km, the temperature value is lower than the real one due to the effects of aerosols.

The temperature algorithm only Rayleigh-scattered light signals produced by the atmosphere from the third harmonic of Nd-YAG laser at 355 nm were used. During the lidar measurements, the output of the multi-channel counters (MCS) provides the raw data as single ASCII files, with an integration time of 1 minute. The retrieval algorithm reads two raw data sets at 355 nm (high and low sensitivity), then performs a data integration variable from 1 to 3 hours. In the next step, two corrections are applied to remove systematic errors in the signals: background signals, Signal-Induced Noise (SIN). The objective of these corrections is to obtain a pure lidar backscattering signal. Then both corrected signals are merged by means of linear fitting in the 20-25 km range.

After this corrections, we retrieved the temperature profile from the lidar signal.

ECC sondes

The balloon sondes used during OZITOS II campaign are configured by a radiosounding and an ECC which is the responsible for the detection of ozone concentration. In our experiment the ECC sonde launched has also a radiosounding which can measure temperature, humidity and pressure.

The radio receptor is a Lockheed Martin LMG6. It was used for store all data emitted by the sonde. As sensor we used a meteorological radiosounding LMS6. An ECC model EN-SCI Corporation was used for measure the ozone concentration.

OZITOS II CAMPAIGN

In December 2008, the instrument DIAL for the measurements of stratospheric ozone profile deployed in the Patagonian city of Río Gallegos was accepted as part NDACC (Network for the Detection Atmospheric Composition Change). This new stage of the instrument must satisfy new requirements as intercomparisons with other kind of sensor to check the stability and guarantee a quality in the measurements. Very often different groups around the world used ECC balloon sondes for measured ozone concentration in a region between the surface up to 30 km aprox.

Though the principal objective was to make validations between DIAL and ECC balloon sondes, this paper showed the comparison between temperature profile derived with the 355 nm line as described above and the temperature profile measured with the radiosounding, during OZITOS II campaign.

Experimental design

The night March 17, 2011 both groups decided to lunch in a same night three balloon sonde in coincidence with the DIAL operation. The aim was study the minimum time of integration in the data files acquired by DIAL systems. The schedule of the experimental design is showed in Figure 1.

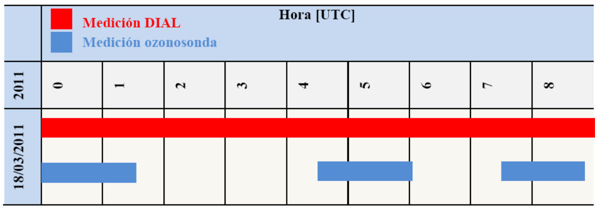

Figure 1. Schedule of measurement made in the OAPA during OZITOS II campaign in March 17, 2011. The red bar is the time that the lidar were measuring and blue bar the period of flight of each ozonesounding.

Where the horizontal red bar indicate the total time of measurement of the DIAL system and the blue bar indicate the time of flight of the ozonesounding. Can you show that the DIAL systems was operating more than nine hours. If we select a time of integration of three hours we can obtain three independent measurements that each one can be compared with each balloon sonde launched (same period time of flight). Now we can decrease the time of integration, and we can derivate for example more profiles.

The advantage using signals obtained by a DIAL system, is that we can use the signals in 355 nm from the Nd:YAG laser for retrieved a temperature profile without produced any interference on the ozone measurements.

Results and discussion

We have taken from the total measurement about nine hours from Rayleigh, three independent period of time which we calculated the temperature profile using a time of 180 minutes of integration. This time is quasi-coincident with the time of flight of the ozonesounding launched beside, 1 km away of the DIAL system in Río Gallegos. This means that we can compare temperature derived from both instruments.

In Figure 2, we showed the comparison of the temperature profile between the Rayleigh lidar temperature and the radiosounding.

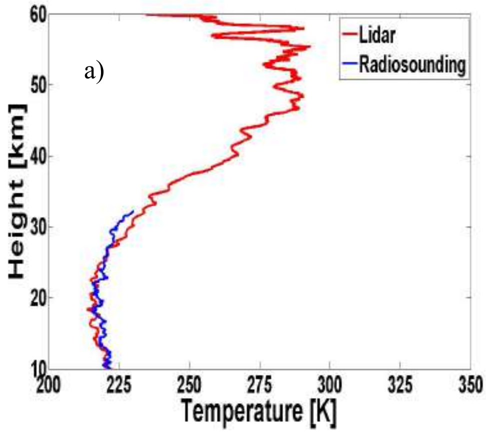

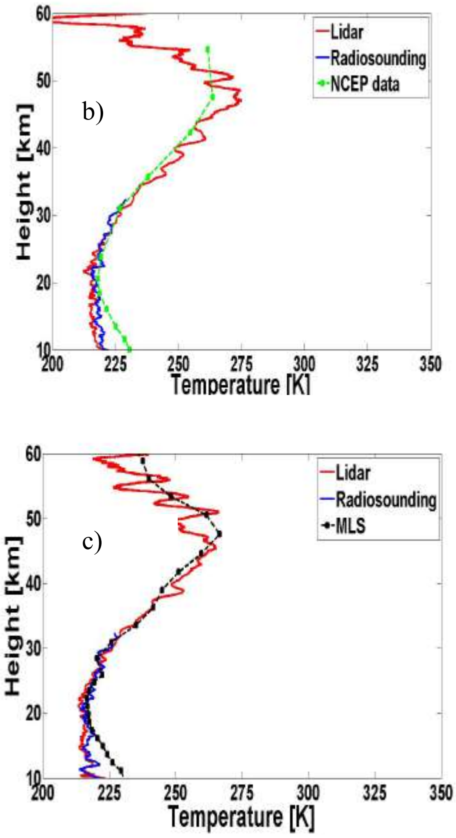

Figure 2. Comparison of the temperature profiles; a), b), c) are the temperature profile by the Rayleigh lidar (red line) compared with radiosounding (blue line). b) show the comparison with NCEP data (dashed green line with square) for March 17, 2011 in Río Gallegos and c) show the comparison with a MLS sensor(dashed black line with square) aboard AURA-NASA in March 17, 2011 lat=-51.74 °, lon= -75.23 °, time: 06:03:09 (UTC).

The region of comparison between both instruments is a disvantage due they have different heights of cover.
In the case of the Rayleigh lidar we can obtain temperature profile from aprox. 10 km up to 60 km. While in the balloon sonde only we can measured temperature profile between the surface up to 32 km. The effective zone where both instruments can be compared, cover the range 10 to 32 km, aprox, limited in the lower part for the lidar and in the higher part for the balloon burst altitude.
The Figure 2 has shown the good agreement between the diferent profiles, having a relative error lidar - radiosounding lower than 4 %. Additional in b) we superposed the NCEP data for the same day of measurement, and c) show the comparison with the data provided by the MLS instrument aboard the plataform AURA-NASA.

CONCLUSION

This paper has shown three independent temperature profiles derivated with a Rayleigh temperature lidar for one day (March 17, 2011). These profiles were obtained as a part of the OZITOS II Campaign described above. In each measurement the Rayleigh temperature profiles were compared with the radiosounding aboard the balloon sonde. The effective region for the comparison can be established due figure 2 in the region between 10 up to 30 km aprox. Both instruments have shown good agreement in this region, with a typical relative error lower than 4 %. We have observed also that in this night the three lidar profiles are similar, indicating that the atmospheric conditions were stable. As a comparison with other instrument as the NCEP data and MLS instrument aboard the AURA-NASA satellite has been to do it. It measurements were superposed in the profiles b) and c) (figure 2) showing very good agreement in the region above 20 km. For the region below both measurements (NCEP data and MLS) indicate a discrepancy very similar when are compared with the radiosounding and temperature lidar profiles.

ACKNOWLEDGMENTS

The authors would like to thank JICA (Japan International Cooperation Agency) by financial support of UVO$_3$ Patagonia Project; the CNRS in France for their collaboration in facilitating the shelter and part of the electronic instruments of DIAL.
Analyses used in this paper were produced with the Giovanni online data system, developed and maintained by the NASA GES DISC.

REFERENCES

Acker and, J. G., G. Leptoukh, (2007), Online Analysis Enhances Use of NASA Earth Science Data", Eos, Trans. AGU, Vol. 88, No. 2, pages 14 and 17.

Gross, M.R., McGee, T.J., Ferrare, R.A., Singh, U.N., Kimvilakani, P, (1997), Temperature measurements made with a combined Rayleigh–Mie and Raman lidar, Applied Optics ,36, pp, 5987–5995.

Gu, Y.Y., Gardner, C.S., Castleberg, P.A., Papen, G.C., Kelley, M.C, (1997), Validation of the lidar in-space technology experiment: stratosphere temperature and aerosol measurements,Applied Optics, 36, pp, 5148–5157.

Komhyr, W.D., (1969), Electrochemical concentration cells for gas analysis, *Ann. Geoph., 25,* 203-210.

Komhyr, W.D., (1971), Development of an ECC-Ozonesonde, *NOAA Techn. Rep. ERL 200-APCL 18ARL-149*.

Nedeljkovic, D., Hauchecorne, A., Chanin, M.L, (1993), Rotational Raman lidar to measure the atmospheric-temperature from the ground to 30 km, IEEE Transactions on Geoscience and Remote Sensing, 31,pp, 90–101.

Steinbrecht, W., and A.I. Carswell, (1995), Evaluation of the effect of Mount Pinatubo aerosol on differential absortion lidar measurements of stratospheric ozone. J.Geophys. Res.100, 1215-1233.

Wolfram, A. E., J. Salvador, R. D'Elia, C. Casiccia, N. Paes Leme, A. Pazmiño, J. Porteneuve, S. Godin-Beekman, H. Nakane and E. J. Quel, (2008), New Differential absorption lidar for stratospheric ozone monitoring in Patagonia, south Argentina, J. Opt. A: Pure Appl. Opt. 10, 104021 (7pp). oi:10.1088/1464-4258/10/10/104021.

REVISTA BOLIVIANA DE FÍSICA 20s, 36-38, 2011
ISSN 1562-3823. INDEXADA EN: SCIELO, LATINDEX, PERIÓDICA

Optical study of the laser beam propagation on Nd:YAG crystal slab for space LIDAR missions

Kosmas Gazeas, George Tzeremes and Errico Armandillo
European Space Agency, ESTEC, Mechatronics and Optics Division
Keplerlaan 1, 2200AG, Noordwijk, The Netherlands
Tel: +31 71 5656743, Fax: +31 71 5655430, E-mail: Kosmas.Gazeas@esa.int, kgaze@physics.auth.gr

SUMMARY

The present paper reports on the development of a simulation and modeling tool which allows to estimate the propagation effects on a laser beam passing through a laser-diode-pumped Nd:YAG slab amplifier. This in-house research work is motivated by current ESA spaceborne LIDAR programs (ADM, Earth Care) as a mean to provide understanding of the LIDAR beam pointing stability as results of thermal and mechanical stresses. A dynamic model has been generated that can simulate the optical characteristics of the laser beam propagation, as a result of the various thermal and mechanical processes occurring inside the laser Pumping Unit and the thermal lensing occurring along the crystal slab. The simulation results and their comparison with actual laboratory tests are being presented and discussed. The model developed is based on the Finite Element Model (FEM) methodology, where the slab as an active element is "broken" down into interdependent segments, each simulated as being heated by an individual LD source. The light beam is propagated along the slab using dynamically varying boundary conditions, to the next so to account for the cumulated thermal and mechanical loads.

Key words: Nd:YAG laser, thermal lensing, LIDARS

INTRODUCTION

LIDARs in space require reliable operation of high power laser transmitters. It is the case for ESA ADM and EarthCare missions where high power UV lasers are being used in an oscillator-multipass amplifier configuration to reach the required energy level and characteristics (Figure 1). ESA space LIDAR programs use both high power Nd:YAG slab, with diode-laser (LD) pumped. In these configurations, thermo-mechanical behavior of the slab can affect seriously the output laser beam characteristics, specifically the most critical variables which can play an important role in the output laser beam are the:

- Coldplate temperature (TCP)
- Laser Diode physical characteristics and location
- Slab geometry
- Input beam characteristics
- Collimating optics
- Operating conditions (air/vacuum, ambient temp.)

To model such processes, it is to be noted that since the number of variables is too large to allow a closed form solution for the thermal lensing of the crystal slab, Finite Element Method (FEM) is proposed and used to compute the combined thermal, mechanical and optical effects.

MOTIVATION OF THIS WORK

The final goal is to achieve fully controlled boundary conditions and direct view of the outgoing laser beam. This way we can predict the necessary modifications needed to preserve the laser energy and amplification efficiency reducing energy loss at minimum. Also we will have the ability to predict the outgoing laser beam profile and divergence. This will give direct information for the actual lenses need to be applied before and after the PU, in order to focus the beam and preserve its shape and energy density.

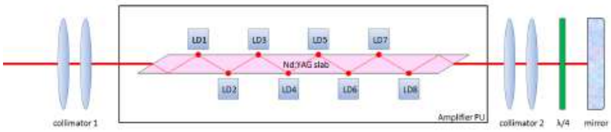

Figure 1. A schematic of the amplifier PU.

Nd:YAG CRYSTAL SLAB GEOMETRY

The crystal slab geometry is shown in Figure 2. A laser beam with a Gaussian profile at 1064 nm enters the crystal parallel along the long axis and bounces 5 times on the top and 5 on the bottom inner surfaces. The other two side surfaces are attached to the cold plates, pumping out the accumulated heat. Boundary conditions are controlled by heat drain from the two cold plates and the energy emitted from the 8 pumping laser diodes at 808 nm.

THERMAL LENSING

Thermal lensing effects take place along the crystal slab, as the thermal profile is variable. As a consequence, the refractive index is variable, following the thermal profile, as described by Shellmeier equations. For every finite cross section of the slab, a thermal profile is calculated, following boundary conditions. Each cross section is converted to a “refractive index matrix”, acting as lens for the laser beam. The number of thermal lenses is a variable parameter in the performance model for fine tuning and resolution control. Laser beam “interacts” with “thermal lenses”, as a normal lens. We assume ray optics (geometrical/linear optics) for the beam propagation and no scatter through diffraction through OPD. Refraction is taken into account via the beam’s angle of incidence on the thermal lenses (Snell law).

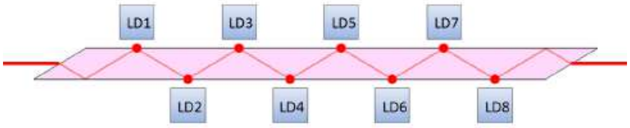

Figure 2. The 1064 nm laser beam is travelling along the Nd:YAG slab, bouncing 10 times on the inner slab surface, while the laser diodes are pumping energy from top and bottom, producing 8 hot spots on the crystal slab. The laser beam enters the crystal from left, exits from the right and its turned backwards with a mirror, causing the beam to enter the slab again, following the same path.

THE DEVELOPED SIMULATION GUI

Our simulations resulted in a graphical user interface (GUI) control panel, where the user can insert all variables necessary for the crystal slab geometry and boundary conditions (TCP and LD boundary temperatures, slab geometry, number of LDs, slab’s refractive index, etc), as shown in Figure 3. The incoming beam is assumed to have a Gaussian profile (could be an input variable in a forthcoming version) with a user-defined divergence and the outgoing beam is given for both single and double laser beam pass through the crystal slab. Beam can be shifted up-down-left-right in order to examine the effect of poor optical alignment.

MECHANICAL DEFORMATION – STRESS

Deformation through expansion is taken into account in calculations. This effect does not have any significant direct optical effect. Indirectly, however, it affects conductivity of the crystal slab with the CP, changing boundary conditions. Expansion leads to stress of slab and conductivity variability. This in turn leads in new thermal profile, which can be input as step 1 in our study. Variations of the initial parameters (geometry and environmental effects) as well as the boundary conditions result in a laser beam deformation pattern, according to the input parameters. An example is given in Figure 4.

SIMULATIONS – EXPERIMENTAL TESTS

It is observed that the boundary temperature variations affect drastically the outgoing laser beam shape, resulting in an unfocused and highly divergent non-Gaussian beam. Recent experimental tests demonstrated that small environmental temperature changes as small as 1° C can drastically affect the performance of the PU. This is a result of multiple physical factors being affected simultaneously from temperature (such as the LD’s wavelength of operation, the LD’s optical to optical efficiency, the absorption profile of the Nd:YAG crystal, the crystal boundary temp. conditions, ASE etc.). Our simulations can resample the existing experimental results and can predict the laser beam profile as a function of the boundary conditions, giving accurate quality results (Figure 5). Moreover, additional results have to be collected for the algorithm calibration. This will be done by in-situ experimental tests performed on a Nd:YAG crystal slab and its amplification performance as a function of temperature perturbations. These final results will provide the actual images required for accurate calibration of our algorithms.

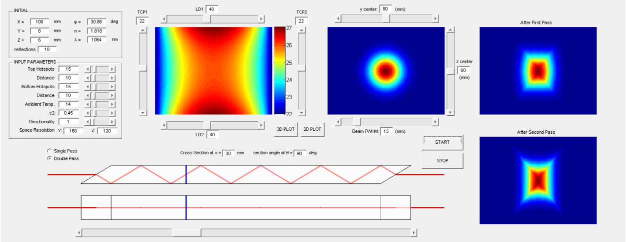

Figure 3. The developed GUI can simulate the thermal profile inside the crystal slab and predict the outgoing laser beam deformation after a single and double pass through the slab. All boundary conditions can be controlled (LD temp., CP temp., laser beam offset, ambient temp., input laser beam profile (assumed Gaussian here), crystal geometry etc).

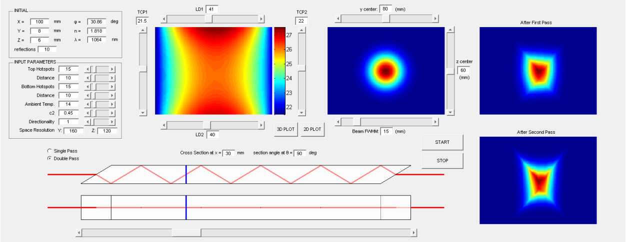

Figure 4. Small asymmetries of the boundary conditions result in a asymmetric laser beam deformation, visible in both single and double pass through the slab (panels on the right). Note that even 0.5° C difference between the TCP and 1° C between the LD heating cause a significant asymmetry on the outgoing laser beam at the bottom-right panel.

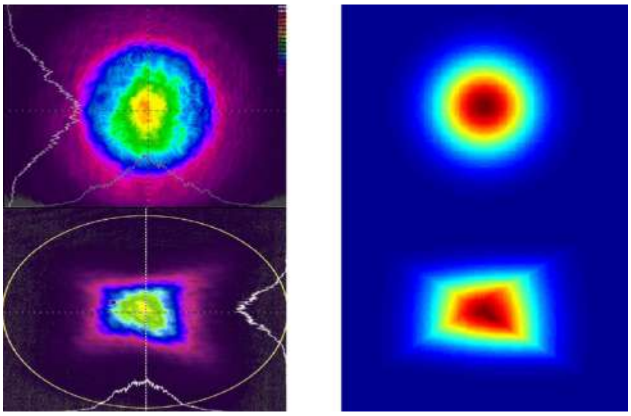

Figure 5. A comparison of actual experimental tests, provided by Selex Galileo (left two panels) with our simulations (right two panels). The results are significantly similar. Precise model calibration and fine tuning of the parameters will allow us to predict the shape of the outgoing beam from the amplifier PU.

CONCLUSIONS

Experimental tests are currently undertaken at ESA/ESTEC establishment, in order to validate the thermal lensing performance model and calibrate/quantify/validate the thermal lensing effect. However, tests already performed by Selex Galileo in Italy show that CP temperature mainly drives the laser beam divergence and focusing ability (shape and profile), while temperature uniformity is the key answer to laser amplification optimization (as well as minimization of the laser beam dimensions). Our results are successful and the developed performance model is a promising tool for studying the thermal lensing effect, caused by a given thermal profile along the Nd:YAG slab.

.

REVISTA BOLIVIANA DE FÍSICA 20s, 39-41, 2011
ISSN 1562-3823. INDEXADA EN: SCIELO, LATINDEX, PERIÓDICA

Imaging LIDAR performance model development and simulation

Kosmas Gazeas, João Pereira do Carmo
European Space Agency, ESTEC, Mechatronics and Optics Division
Keplerlaan 1, 2200AG, Noordwijk, The Netherlands
Tel: +31 71 5656743, Fax: +31 71 5655430, E-mail: Kosmas.Gazeas@esa.int, kgaze@physics.auth.gr

SUMMARY

LIDARS involved in space applications are mainly used as atmospheric monitoring sensors or as altimeters (i.e. ALADIN, ATLID, LOLA, MOLA or BELA). In future exploration missions, like the Mars Sample Return mission, LIDARs shall be implemented as imaging and ranging devices for different applications: in the support of the autonomous landing of a spacecraft on a planetary surface; during the deployment of rovers provided with autonomous navigation and hazard avoidance capabilities; and for the support of rendezvous and docking operations between spacecrafts in orbit. The ability to rapidly derive 3-D topographic information is vital for the realization of these missions. We present a recently developed Imaging LIDAR (IL) performance model, which was created in order to simulate and optimize Imaging LIDAR instruments, under various scenarios and applications. The IL performance model is based primarily on the LIDAR equation and takes into account all basic parameters of a LIDAR device, which apparently affect the overall instrument performance, such as the laser power, telescope aperture, detection method, background illumination, range gating etc.

Key words: Imaging LIDARS, performance model

INTRODUCTION

Several commercial laser-based LIDARS exist in the market, some of which were developed for Space Applications mainly used as altimeters (i.e. ALADIN, ATLID, LOLA, MOLA or BELA). An Imaging LIDAR will give the traditional 2D image information, but in addition with the 1-dimentional ranging measurements will create 3D target images. Some ILs are currently under development and testing at the Agency. They can be used in several ways in space and they are a key technology for space missions, which include robotic operations with visualization techniques. The upcoming Exploration missions shall utilize such technologies. They will require the autonomous landing of a spacecraft on a planetary surface (Lander), the deployment of a rover with the additional autonomous surface navigation (Rover) and the return of samples from the planetary surface, which will require complex orbital rendezvous and docking (RvD) maneuvers. The ability to rapidly derive 3D topographic information is vital for the realization of these missions.

IMAGING LIDAR GEOMETRY

Figure 1 shows a simplified block diagram of a typical Imaging LIDAR setup. The system consists of a laser source, an optical system and a detector. Every sub-system includes a power supply, and its necessary electronics. A scanning system might be used, in order to illuminate a larger surface, depending on the detector's design and/or the laser optical power. The requirements for the development of an Imaging LIDAR system for the orbital rendezvous and docking, the soft landing and rover operation in the context of the upcoming Exploration missions like the Mars Sample Return mission include a wide FOV (of the order of 20×20 deg), fast scanning and image processing, and should give ranging accuracy of about 0.1% at any given distance. All this setup should be fit in a light and compact device, weighting less than 10 kg and consuming approximately 50 W of energy.

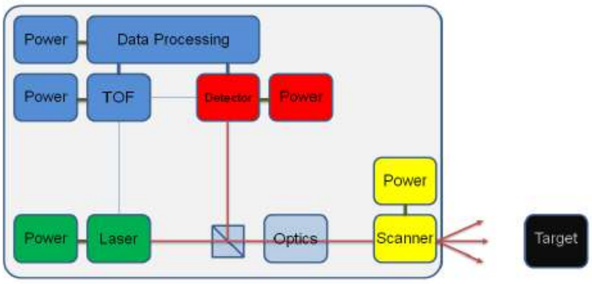

Figure 1. The simplified block diagram of a typical Imaging LIDAR system.

MATHEMATICAL FORMULATION

The model is based primarily on the LIDAR equation. The secondary key factor that must be considered is the operation of the detector, which could be based either in Geiger or in Linear detection modes. The detection method affects the overall performance of the instrument. Therefore the model must first compute the probability of observing a signal photons and background photons. The detection method also reflects the errors in the measurement associated with the pulse length of the laser and, if applicable, the size of the range gate. For all the following simulations presented within this report, the surface is always assumed to be within a range gate. Background photons can arrive at any time within the range gate across the full FOV, whereas the signal photons will only backscatter off the target.

THE DEVELOPED SIMULATION GUI

The primary purpose of the LIDAR performance model is to determine the performance of the LIDAR instrument. This allows the design to be optimized in terms of identifying the major sub-system level parameters that influence the instrument performance. The model calculates both the signal and background flux rate in photons observed by the instrument. Apart of the LIDAR instrument setup, the target size and environmental parameters have to be taken into account. The current version of the IL performance model is shown in Figure 2. It consists of five main panels, including the input instrumental and environmental parameters, and the necessary 2D, 3D and quality plots for visual inspection of the results. Statistics of image recovery is also provided.

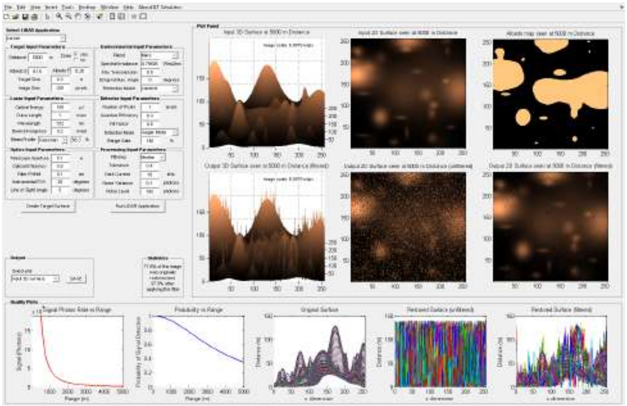

Figure 2. The layout of the Imaging LIDAR Simulator performance model. Input parameters are inserted in the top-left panels, while the input and output 2D and 3D images are created on the top-right. Quality plots and data exporting information are available on the bottom of the interface.

METHODOLOGY

Once the target surface and its reflecting properties are inserted into the model, the ideal image is produced representing the “perfect LIDAR return”, with resolution given by the user, referring to the final detector format (detector array or single-element scanned array). For the sake of uniformity, the detector array is assumed to be square, with uniform properties across all its pixels (similar QE, FF etc). The signal and background photon arrival rates are then computed from the input instrument parameters. The probability of observing a signal photon or a background photon can then be computed. The ground is then located within the range gate. A background and a signal image are then constructed with the range value of all returned photons. These two images are combined and the raw LIDAR image is constructed (Figure 3). This image can be post-processed using a smoothing algorithms and special filtering.

SIMULATIONS – EXPERIMENTAL TESTS

It is observed that the boundary temperature variations affect drastically the outgoing laser beam shape, resulting in an unfocused and highly divergent non-Gaussian beam. Recent experimental tests demonstrated that small environmental temperature changes as small as 1° C can drastically affect the performance of the PU. This is a result of multiple physical factors being affected simultaneously from temperature (such as the LD’s wavelength of operation, the LD’s optical to optical efficiency, the absorption profile of the Nd:YAG crystal, the crystal boundary temp. conditions, ASE etc.). Our simulations can resample the existing experimental results and can predict the laser beam profile as a function of the boundary conditions, giving accurate quality results (Figure 5). Moreover, additional results have to be collected for the algorithm calibration. This will be done by in-situ experimental tests performed on a Nd:YAG crystal slab and its amplification performance as a function of temperature perturbations. These final results will provide the actual images required for accurate calibration of our algorithms.

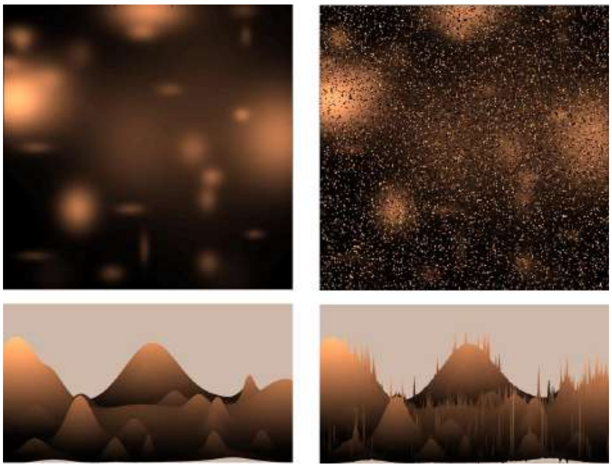

Figure 3. An example of input and output from the Imaging LIDAR performance model. An artificial surface is inserted in the simulator, as a 2D matrix or a 3D map, as shown on the two left panels. The panels on the right show the output 2D and 3D color indexed maps, of the same surface, as seen from a LIDAR device, using a certain set of parameters.

CONCLUSIONS

Experimental The developed Imaging LIDAR Simulation model designed especially to test the performance of the Imaging LIDAR can be used as a virtual LIDAR device, where the user will be able to test potential novel technologies in the frame of imaging and ranging devices. These results will support the future Imaging LIDAR technology developments by providing key information on sub-system level design parameters and there impact on the system performance. It gives a variety of input parameters and their combinations, where one can choose a wide variety of parameters, applications, target specifications and be as flexible as possible, covering all major LIDAR applications and working environments. The output 2D and 3D plots allow a visual inspection of the LIDAR return image, while the quality plots and statistical information quantify the results. Post-processing may be applied to the final LIDAR return image, in order to improve the quality of the image and increase the overall restoration. Optimization of the model is practically unlimited. The GUI can always be updated in the future versions may come out in the future. Some of the future modifications and possible updates may include a fully controlled detailed target surface, create custom surface or input a 3D map from available archival data (or software produced, i.e. PANGU). The output of the IL Simulation Model can be used as the input for other applications, while the output of other applications can be used as an input of the current software. This will create a functional model, flexible enough to work in cooperation with other commercially available software and hardware products.

REVISTA BOLIVIANA DE FÍSICA 20s, 42-44, 2011
ISSN 1562-3823. INDEXADA EN: SCIELO, LATINDEX, PERIÓDICA

Aerosol transport to the Andean region: A new GAW station

Andrade M., R. Mamani, F. Velarde, D. Biggeman, F. Zaratti y R. Forno
Laboratorio de Física de la Atmósfera, Instituto de Investigaciones Físicas, Universidad Mayor de San Andrés
Campus Universitario, Cota-Cota, La Paz, Bolivia
Tel/Fax: +591-2-2799155, E-mail: mandrade@fiumsa.edu.bo

SUMMARY

The importance of particulate matter transport over the Andean glaciers has recently grown because new studies have suggested that at least part of the local warming at the Himalayas might be due to transport of particles to this region. In the Andean region the rapid retreat of glaciers and a moderate increase in temperature suggest that particulate matter product of biomass burning could also be playing a role in the observed glacier recession. Satellite imagery from MODIS, measurements from photometers as well as in-situ measurements were used to try to characterize some optical and chemical properties of particulate matter arriving to the Andean region. Backward trajectories and electronic microscopy were also used for this purpose. Preliminary results are reported here. In addition, the implementation of a new GAW station at Chacaltaya (5200 masl; 16°21'S, 68°07'W) is discussed in this context.

Key words: aerosol, aerosol transport.

INTRODUCTION

The effects of anthropogenic atmospheric aerosols upon glaciers have been object of great interest due to the observed rapid melting of the latter in different parts of the world (Hansen and Nazarenko, 2003, Hegerl et al., 2007). Studies in Asia, especially over the Himalayas (Xu et al., 2009; Lau et al., 2010) suggest that aerosols transported to this region might be playing an important role both in changing albedo properties of snow and ice as well as increasing local temperature of the atmosphere, contributing in this way to the rapid receding of the Himalayan glaciers.

Similarly, a fast decrease in area and volume of the ice mass in the Andean glaciers has been reported by different studies (Francou et al., 2003; Vuille et al., 2008). Regular field measurements at Bolivian glaciers began at the beginning of the 1990's. These measurements showed a rapid decrease of all glaciers where studies were conducted. At the moment some of these glaciers have already disappeared completely (Chacaltaya, for example). Despite some controversy about their contribution, the importance of these ice masses is directly related to the water supply of both humans and ecosystems, especially in the dry season when glaciers act as water reservoirs.

Although a positive trend in both the seasonal mean aerosol optical depth (AOD) and fire data recorded by satellite instruments has been reported between 1998 and 2005 (Koren et al., 2007), the observations showed a decline between 2006 and 2009. This decline has been linked to policy shifts (Koren et al., 2007) especially because the analysis of particular years show no especial conditions that could explain the reduction of biomass burning and its associated production of smoke (Torres et al., 2010). In contrast to this latest trend, biomass burning has been particularly intense in 2010.

REMOTE OBSERVATIONS

Observations of aerosol optical depth (AOD) using a sunphotometer CIMEL obtained at the Atmospheric Physics Laboratory, APL, (3420 masl; 16º32'S, 68º04'W) in the city of La Paz, Bolivia show that during biomass burning season AOD could reach unusual high values for this region (~0.80 at 340 nm; yearly mean values are on the order of 0.15). Satellite imagery from MODIS (Moderate Resolution Imaging Spectroradiometer) show that smoke produced at the Bolivian lowlands and neighbor countries can reach high altitude locations over the Bolivian Andes. Carbon monoxide measurements by the MOPITT (Measurements of Pollution in the Troposphere) sensor flying aboard NASA's Terra spacecraft show large concentrations at the surface east of the Andes and give some indication of possible transport to the high lands as well.

Figure 1. Smoke transported over the Andes mountains on September 29, 2010. Image obtained by a MODIS sensor onboard of NASA's Terra satellite.

IN-SITU OBSERVATIONS

With the aim of studying transport of aerosol particles produced by biomass burning east of the Andes, a set of experiments have been conducted. Using a MOUDI cascade impactor to examine surface air aerosols with different aerodynamic sizes, samples were collected under clean conditions (June, 2010) and in the middle of the biomass burning season (September, 2010) at Chacaltaya (5200 masl; 16°21'S, 68°07'W) and Cota-Cota, La Paz (3420 msal; 16°32'20.71"S, 68° 3'58.69"W)..

Figure 2. GoogleEarth images show the locations on the Andes mountains where samples were collected. Cota-Cota is located in the outskirts of La Paz, whereas Chacaltaya is on a relatively pristine environment. Air masses arriving from the Amazon basin, the Altiplano, and also from La Paz metropolitan region are observed at Chacaltaya..

In order to better understand the type of particles collected at high altitude locations, samples at regions near the biomass fires (522 masl; 16°16'S, 62°30'W) were also collected. The analyses show a small increment in PM2.5 concentration at Chacaltaya between clean and smoky conditions. In contrast, the concentration was almost 5-times larger in regions near the fires (Table I). Analyses performed by X-Ray techniques as well as by electronic microscopy on the samples collected at stages 6 to 8, where aerodynamic size particle varies from 0.56 μm to 0.18 μm, show that under clean conditions there is no trace of potassium whereas during biomass season traces of potassium are present not only in La Paz and Chacaltaya (the Andean region) but near the area where fires are produced. The presence of potassium has been reported in aerosols from biomass burning (Andreae, 1983). More analyses are needed in order to identify other elements, size and shape of the aerosols as well as other physical and chemical properties.

Site	Period (2010)	Conditions	Sampling Time	$PM_{2.5}$ (μg/m^3)	PM_{10} (μg/m^3)
Chacaltaya	June	Clean	5d,3h,50m	6.6±0.1	19.2±0.2
Chacaltaya	August	Smoky	4d,3h,30m	9.4±0.1	16.3±0.1
San Javier	September	Smoky	5h,10m	58±1	72±1

Table 1. Summary of results obtained from mass analysis.

In addition, HYSPLIT (Hybrid Single Particle Lagrangian Integrated Trajectory Model) a computer model for computing simple air parcel trajectories was used to estimate the possible sources of the air sampled at different locations by tracing its backward trajectories. As expected, the results suggest that air masses arriving at the surface or passing near the surface have their origin not far from the sampling sites, whereas air transported at higher altitudes usually travels much larger distances and could have its origin in regions completely free of influence of biomass burning.

A NEW GAW STATION

After submission of a project by a consortium of European institutions and Universidad Mayor de San Andres to the World Meteorological Organization, Chacaltaya has been designated a Global Atmosphere Watch (GAW) regional station. This high altitude station is located in a strategic place because air masses from distinct origin arrive at different times of the year. For instance, air masses from the Amazon region are typically transported from the eastern side of the continent during (Southern Hemisphere) summer time but air masses are transported from the Altiplano region during winter time.

The new station will begin taking measurements of optical properties, size distribution and other properties of aerosols arriving to this site as well as measuring concentrations of CO_2, surface ozone and carbon monoxide. In addition chemical properties of aerosols will also be studied at Chacaltaya. In this case, sampling will be performed at the mountain summit (5380 masl) using a high-volume sampler.

At the same time, the recently implemented LIDAR system at the APL will be upgraded in order to study the boundary layer around or above Chacaltaya. In this case, simulations are being performed in order to optimize the system.

The new station is expected to begin regular operations by December of 2011.

CONCLUSIONS

We presented results of a preliminary study showing transport of particulate matter produced by biomass burning to the Andean region. Remote and in-stu observations show that smoke goes across the Andean mountains and is likely deposited over the glaciers present on that region. The net effects of such process will be object of study by the new GAW station at Chacaltaya.

ACKNOWLEDGMENTS

This work has been partially funded by the Danish cooperation through a project carried out by Universidad Mayor de San Andrés. We thank SwissContact Bolivia for its strong support during the field campaigns.

REFERENCES

Andreae, M.O. (1983), Soot carbon and excess fine potassium: Long-range transport of 13 combustion-derived aerosols, Science, 220, 1148-1151.

Francou, B., Vuille, P. Wagnon, J. Mendoza, and J. Sicart (2003), Tropical climate change recorded by a glacier of the central Andes during the last decades of the 20th century: Chacaltaya, Bolivia, 16°S, J. Geophys. Res., 108 (D5), 4154, doi:10.1029/2002JD002959.

Hegerl, G.C., F. W. Zwiers, P. Braconnot, N.P. Gillett, Y. Luo, J.A. Marengo Orsini, N. Nicholls, J.E. Penner and P.A. Stott, 2007: Understanding and Attributing Climate Change. In: Climate Change 2007: The Physical Science Basis. Contribution of Working Group I to the Fourth Assessment Report of the Intergovernmental Panel on Climate Change [Solomon, S., D. Qin, M. Manning, Z. Chen, M. Marquis, K.B. Averyt, M. Tignor and H.L. Miller (eds.)]. Cambridge University Press, Cambridge, United Kingdom and New York, NY, USA.Hansen J, Nazarenko L (2004) Soot climate forcing via snow and ice albedos. Proc Natl Acad Sci USA 101:423–428.

Koren, I., L. A. Remer, and K. Longo (2007), Reversal of trend of biomass burning in the Amazon, Geophys. Res. Lett., 34, L20404, doi:10.1029/2007GL031530.

Lau ,W. K. M., Maeng-KiKim, Kyu-MyongKim and Woo-Seop Lee, Enhanced surface warming and accelerated snow melt in the Himalayas and Tibetan Plateau induced by absorbing aerosols, Environ. Res. Lett. 5, 2010.

Vuille M., B. Francou, P. Wagnon, I. Juen, G. Kaser, B. Mark, and R. Bradley. Climate change and tropical andean glaciers: Past, present and future. Earth-Science Reviews, 89(3-4):79–96, August 2008.

REVISTA BOLIVIANA DE FÍSICA 20s, 45-47, 2011
ISSN 1562-3823. INDEXADA EN: SCIELO, LATINDEX, PERIÓDICA

Determination of the seasonal variation of the nitrogen dioxide and ozone vertical column density at Río Gallegos, Santa Cruz province, Argentina, using a zenith-sky DOAS system

Marcelo Raponi, Elian Wolfram, Eduardo Quel,
Centro de Investigaciones en Láseres y Aplicaciones, CEILAP (CITEDEF-CONICET), UMI-IFAECI-CNRS 3351
Juan B. de La Salle 4397, B1603ALO, Villa Martelli, Buenos Aires, ARGENTINA
Tel: +541147098100 ext 1410, Fax: +541147098122, E-mail: mraponi@citedef.gob.ar
Rodrigo Jiménez
Grupo de Investigación en Calidad del Aire, Departamento de Ingeniería Química y Ambiental, Universidad Nacional de Colombia
Bogotá, COLOMBIA
Jorge Tocho
Centro de Investigaciones Ópticas, CIOp (CONICET La Plata-CIC)
Buenos Aires, ARGENTINA

SUMMARY

Stratospheric ozone (O_3) plays a critical role in the atmosphere by absorbing most of the biologically damaging solar UV radiation before it reaches the Earth's surface. Nitrogen dioxide (NO_2) is a key trace gas in the ozone photochemical. The systematic sensing of NO_2 and other minority gases is essential in order to understand the stratospheric O_3 destruction and formation processes. We present the study carried out on the seasonal variation of the O_3 and NO_2 vertical column density (VCD), using a zenith-sky DOAS (Differential Optical Absorption Spectroscopy). This system is composed of a spectral analyzer (portable spectrometer HR4000, Ocean Optics), two optical fibers (400 µm of core, 25 cm and 6 m of longitude) and an automatic mechanical shutter. NO_2 and O_3 VCD are derived from solar spectra acquired during twilights (87° - 91° zenithal angles). The data retrieved by our instrument are compared with those coming from the SAOZ spectrometer (Systeme d'Analyse par Observation Zenithale, Laboratoire Atmosphères, Milieux, Observations Spatiales (LATMOS), France). Both systems are located in Rio Gallegos, Santa Cruz province, Argentine (51° 36' S; 69° 19' W, 15 m asl), in the CEILAP-RG remote sensing station.

Key words: zenith-sky DOAS, NO2, O3, OMI, SAOZ

INTRODUCTION

Stratospheric ozone (O_3) plays a critical role in the atmosphere by absorbing most of the biologically damaging solar UV radiation before it reaches the Earth's surface. The most important nitrogen species emitted to the atmosphere are nitrous oxide (N_2O), nitrogen oxides ($NO_x = NO+NO_2$) and ammonium (NH_3). N_2O is an important greenhouse gas which is naturally emitted by earth and sea bacteria, and also produced by human activities, mainly agriculture. It is a very stable molecule which is transported to the stratosphere. In the middle and upper stratosphere N_2O is converted to NO by reaction with excited oxygen atoms O (^1D) produced mainly by UV photolysis of O_3 (Fish and Jones, 1995).

During daylight a balance between NO and NO_2 concentrations is established through the reaction of the former with O_3 and the rapid photolysis and reaction with atomic oxygen of the latter. At night, NO_2 is converted first to NO_3 and via a three-body reaction to the N_2O_5 reservoir. This causes a build-up of N_2O_5 during the night followed by a slow release during the following day through photolysis. The diurnal variation of NO_2 therefore comprises a maximum immediately after sunset, followed by a slow decrease throughout the night and a sharp drop to minimum at sunrise. As well as the diurnal variation there is a seasonal variation in stratospheric NO_2 at mid-latitudes due to the combined effects of photochemistry and atmospheric transport (Gil et al., 2007).

The development of remote sensing systems for monitoring of trace gases is fundamental to understand the dynamic processes that occur in the stratosphere. The LIDAR Division (CEILAP-CITEDEF) has in Río Gallegos, Santa Cruz province (51° 36' S; 69º 19' W; 15 m asl) a remote sensing station (CEILAP-RG) where systematically are carry out measurements of several atmospheric parameter (www.division-lidar.com.ar), as for example: the concentration in vertical column O_3 and of NO_2, the O_3 concentration discriminated in height (O_3 profile obtained by LIDAR, between 15 and 45 km), aerosol optical thickness, solar irradiance (UV-A, UV-B, NIR), etc. It is necessary to highlight that Río Gallegos city is affected every spring by a significant decrease of the stratospheric O_3 that produces an increment of the UV solar radiations that arrive to the surface.

MATERIALS AND METHOD

We present the development of a compact atmospheric remote sensing system, able to determine the VCD (Vertical Column

Density) of multiple trace gases. It is a low-cost and portable zenith-sky DOAS system (Figure 1) - hereafter referred to as ERO-DOAS - composed of a mini-spectrometer (HR4000, Ocean Optics), two optical fibers (400 µm of core, 6 m and 25 cm of longitude) and a home-made external shutter (Raponi et al., 2011).

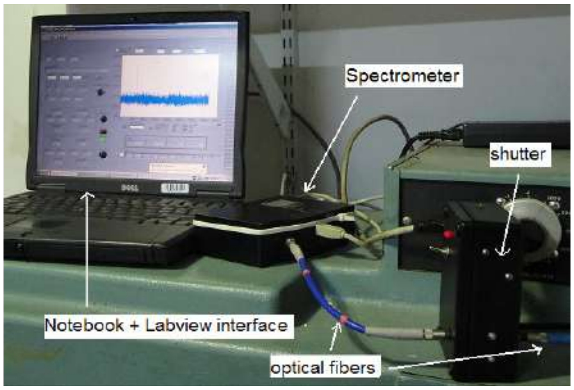

Figure 1. The zenith-sky DOAS system's components: a notebook, the software designed using Labview®, the spectrometer (HR4000), an automatic shutter and the optical fibers.

HR4000 allow us to+ measure solar spectral irradiance in the UV-visible range (290-650 nm). It is a simple spectrograph equipped with a fixed diffraction grating (600 grooves/mm blazed at 400 nm) and a 3648-pixel lineal array CCD. We developed an automatic shutter to determine the dark current of each measurement, and to remove this noise to the twilight spectra. A software development using Labview® controls the start and the end of spectral measurements, the retrieval of acquired spectra and the shutter. The computer internal clock is daily updated to avoid possible time shifts and to maintain accuracy on zenithal and azimuth angles calculations.

The software sets the CCD integration time to maximize signal/noise ratio. The dark (current) spectra are measured with the same integration time than the twilight spectra measured immediately before. This ensures that the subtracted dark noise is similar to the one actually measured over the illuminated period.

The instrumental function and the system resolution were determined using low pressure lamps spectra provided by the Physics Laboratory of Instituto Tecnológico de Buenos Aires (ITBA). We retrieved the spectrometer instrument function from a helium lamp. The full width at half maximum (FWHM) of the Voigt profile fitted to the He line was 1.03 nm at ~447 nm. The lamp spectra were also used to recalibrate ERO's wavelength mapping. This recalibration shows a shift of about -1.55 nm from the original (nominal) manufacturer calibration.

The analysis of visible spectra based on the DOAS concept presents the advantage of allowing for simultaneous retrieval of VCDs of different species, over a wide range of meteorological conditions. NO_2 and O_3 VCDs are retrieved from zenithal solar spectra (in the visible range) acquired on "twilight" conditions (zenithal angle between 87° and 91°) applying the DOAS (Differential Optical Absorption Spectroscopy) technique.

RESULTS

We present a study on the O_3 and NO_2 VCDs seasonal variation at Río Gallegos. In Figure 2 we can observe the NO_2 VCD seasonal variation at Río Gallegos during 2004-2011, retrieved by OMI/AURA. The concentration ranging from $6x10^{15}$ molec/cm^2 in summer to $1.6x10^{15}$ molec/cm^2 in winter and early spring.

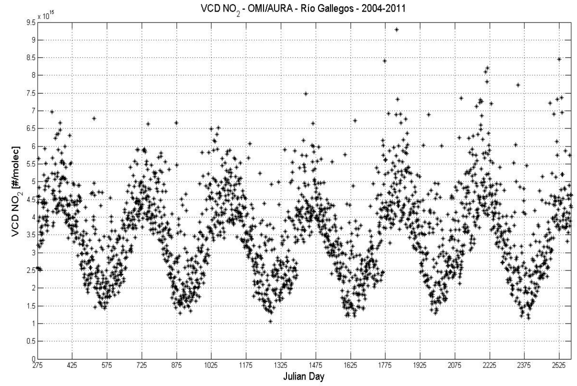

Figure 2. NO_2 VCD variability at Río Gallegos, Santa Cruz province, Argentina, retrieved by OMI-AURA, from 2004 to 2011.

Figure 3 show the NO_2 and O_3 vertical column densities obtained with a SAOZ spectrometer (Système d'Analyse par Observation Zenithale), LATMOS (Laboratoire Atmosphères, Milieux, Observations Spatiales), France, located in the CEILAP-RG station, during 2009.

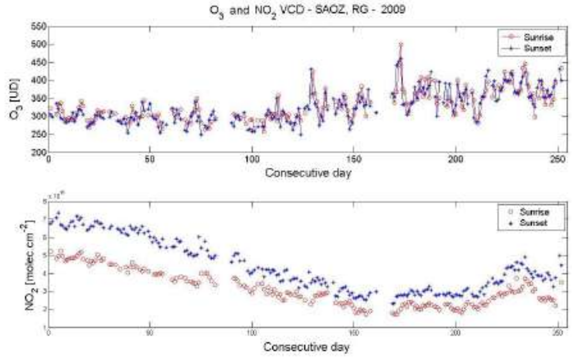

Figure 3: NO_2 and O_3 VCD seasonal variation during 2009, retrieved by SAOZ spectrometer at Río Gallegos.

In the case of the O_3 VCD significant differences are not observed among the concentrations at sunrise and at sunset, as us we waited. In the case of NO_2, to be a gas with a comparatively short photochemical time of life, it presents a significant variability during the day. For that reason, an important difference among the concentrations measured during the twilights, exist.

In Figure 4 we compare the O_3 and NO_2 VCD retrieved by ERO-DOAS and SAOZ spectrometer (both of them located in CEILAP-RG station), during September/December 2009.

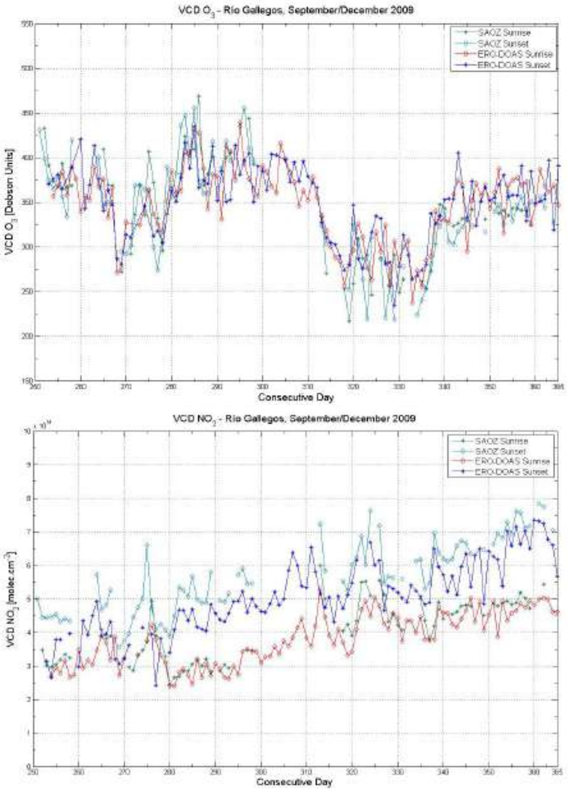

Figure 4. O_3 and NO_2 VCD retrieved by ERO-DOAS and SAOZ instruments at Río Gallegos, during September/December 2009.

For the ozone there is a good agreement among the instruments with an average relative difference about 13%. In the case of NO_2, we observe a better agreement among results at sunrise than at sunset between SAOZ and ERO-DOAS data.

CONCLUSIONS

Our zenith-sky DOAS system has the capability of sensing automatically several chemical species and the advantage of being portable (which offers the possibility to move the instrument to carry out measurements campaigns). We observe in both ground-based instruments a strong daily variability of the NO_2 VCD (sunrise vs. sunset). This variability is probably associated with the NO_x vertical distribution, the temperature in the high layers of the atmosphere and maybe the variability of other active species. In the case of the O_3 the daily variability of the gas is low, reason why the comparison between the sunrise and sunset data is very good.

ACKNOWLEDGMENTS

The authors acknowledge to the Japanese International Collaboration Agency (JICA) for funding the acquisition of the HR4000 spectrometer and to SAOZ network and OMI/AURA for the data at Río Gallegos.

REFERENCES

Fish, D., and R. Jones (1995), Rotational Raman scattering and ring effect in zenith sky spectra, *Geophys. Res. Lett.,* 22 (7), 811-14.

Gil, M., M. Yela, L. Gunn, A. Richter, I. Alonso, M. Chipperfield, E. Cuevas, J. Iglesias, M. Navarro, O. Puentedura and S. Rodríguez (2007), NO_2 climatology in the northern subtropical region: diurnal, seasonal and interannual variability, *Atmos. Chem. Phys. Discuss.* 7, 15067-103.

Raponi M., R. Jiménez, E. Wolfram, J. Tocho, E. Quel (2011), Remote sensing of stratospheric NO_2 over the Argentinean Antarctica using a DOAS mini-spectrometer, *Óptica Pura y Aplicada*, 44 (1), 77-82.

REVISTA BOLIVIANA DE FÍSICA 20s, 48-50, 2011
ISSN 1562-3823. INDEXADA EN: SCIELO, LATINDEX, PERIÓDICA

Using Space-Borne Lidar to Identify Tropospheric Aerosols

Patrick Hamill and Araceli Lopez-Garibay

Department of Physics and Astronomy
San Jose State University
San Jose, California, USA
Tel: 1+408 924 5241, E-mail: patrick.hamill@sjsu.edu

SUMMARY

An important contemporary problem is the identification of aerosols from space. Ground based lidar systems can use correlative measurements to determine aerosol types but spaceborne lidar systems (such as CALIPSO) rely on models for this identification. Most spaceborne systems (including CALIPSO, MODIS, and OMI) use models based on observations by AERONET, a world-wide network of ground based sun photometers. The aerosol parameters determined by AERONET include the real and imaginary refractive indices, the single scattering albedo and the extinction and absorption Angstrom coefficients. We compare the predictions of the satellite models with AERONET measurements by evaluating the Mahalonibis distances from the model prediction to clusters of aerosols of specific types (such as Urban-Industrial, Biomass Burning, and Dust). We show that some regions do not fit any of the traditional categories; consequently, aerosol identification is problematic. We discuss some of the difficulties associated with aerosol identification from space, specifically considering the CALIPSO system

Key words: Aerosols, Lidar, Aeronet, Modis, Omi, Calipso.

STATEMENT OF THE PROBLEM

It is well known that tropospheric aerosols are an important factor affecting climate change. The Intergovernmental Panel on Climate Change (IPCC) states that the aerosol contribution to anthropogenic climate change has a large degree of uncertainty. Consequently, it is of particular interest to be able to give a quantitative accounting of the amount and type of aerosols on a global basis. Only satellite borne sensors (such as the CALIOPE lidar or the OMI or MODIS sensors) can generate the density of measurements on a global scale that is required to understand the role of aerosols.

In this paper we describe the models used by three satellite groups (CALIPSO, MODIS, OMI) to identify aerosols, and we compare the results obtained from these models with the data obtained by AERONET. We find that in general there is a weak agreement between models and observations, as quantified by the Mahalanobis distances from known aerosol types.

Although it is not discussed in this extended abstract, we have found that the degree of linear polarization (a quantity that can be obtained from other aerosol parameters) can also be used as a means of aerosol identification.

AERONET

AERONET (AErosol RObotic NETwork) is an aerosol monitoring network consisting of about 200 solar-powered CIMEL Electronique spectral radiometers that measure sun and sky radiances at several different wavelengths (normally 440, 670, 870 and 1020 nm). The data obtained are inverted to give aerosol optical depths, size distributions, and diverse optical parameters such as refractive index, single scattering albedo and phase function at several different wavelengths. (Holben et al., 1998)

The AERONET archive is a valuable resource for determining properties of aerosols. Cattrall *et al.* (2005) in a preliminary study for CALIPSO used the AERONET archive to define a number of different types of aerosols, based on location and time of year. For example, measurements made at the NASA Goddard Space Flight Center (GSFC) during the period June through September were classified as "Urban Industrial". (We have modified the Cattrall categorization somewhat because we are using Version 2 of the AERONET data and some of the types based on the earlier version are not appropriate.)

In Figure 1 we show scatterplots of extinction angstrom exponent (EAE) *vs.* single scattering albedo (SSA) for the Aeronet data from a number of different sites characterized as urban-industrial, biomass burning, dust, and a "mixed-industrial" category which was observed in Mexico City and Beijing. There are two distinct types of biomass burning aerosols, those found in Africa and those found in South America. In this analysis we used five different parameters (single scattering albedo, extinction angstrom exponent, absorption angstrom exponent, real index of refraction and imaginary index of refraction) at four different wavelengths. Plots such as Figure 1 show that different aerosol types are reasonably well differentiated, and suggests that these parameters could be used to identify aerosols from space.

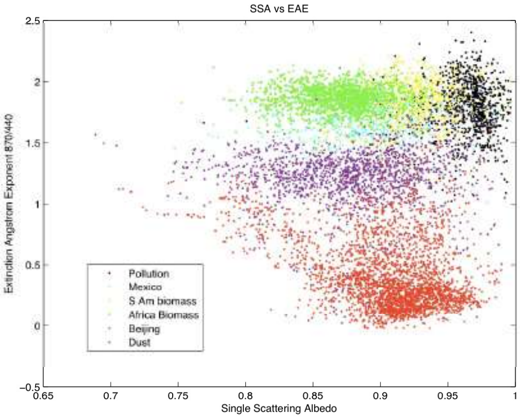

Figure 1. Scatterplot of extinction angstrom exponent (EAE) *vs.* single scattering albedo (SSA) for various aerosol types.

MAHALANOBIS DISTANCE

The Mahalanobis "distance" (which is measured in terms of the standard deviation of a data set) is an efficient and reasonable measure of the probability that a specific measurement belongs to that data set. Consequently, we evaluated the Mahalanobis distances from a set of selected measurements to the various clusters that we consider as "canonical" aerosol types, namely, Urban-Industrial, Biomass-South America, Biomass-Africa, Dust, and Mixed-Industrial. We determined which cluster is "closest" to the selected measurement and as long as it is less than 3 standard deviations from the cluster, we assume the aerosol is of that type.

The Mahalanobis distance can be evaluated using any number of parameters. We normally used five parameters at a single wavelength, but we have carried out calculations using 26 parameters, including values from four different wavelengths. The results are not significantly different from what is presented here.

The Mahalanobis distance is defined as follows: Let $\mathbf{x}=(x_1,x_2,\ldots,x_N)^T$ be an N dimensional vector representing the values of N parameters for a "test point" x. Consider a cluster of values with means given by the vector $\mathbf{m}=(m_1,m_2,\ldots,m_N)^T$. The Mahalanobis distance from the test point to the cluster is

$$D_M=[(\mathbf{x}-\mathbf{m})^T S^{-1}(\mathbf{x}-\mathbf{m})]^{1/2}$$

Where $S=\mathrm{cov}(x_i,x_j)$ is the covariance matrix whose elements are defined by $S=E[(\mathbf{x}-\mathbf{m})(\mathbf{x}-\mathbf{m})^T]$. Here E is the "expectation" which in our case is just the mean value.

THE SATELLITE MODELS

MODIS, OMI and CALIPSO scientists identify aerosol types based on models involving parameters obtained from their measurements. These differ for different sensors. For example, the CALIPSO instrument measures backscatter whereas MODIS and OMI are spectral radiometers. It should be kept in mind that these instruments are extremely good at carrying out their principle tasks; the identification of tropospheric aerosols is not their main purpose. Nevertheless, it is of interest to determine how well one can determine aerosol type from satellite data, so we have carried out an analysis of the models used by the three satellite groups to see how they compare with the AERONET data.

The MODIS models are divided into models for aerosols observed over land and aerosols observed over oceans. We only used AERONET data from land based photometers, so we present here the MODIS land models for comparison with AERONET retrieved quantities. The parameters used in the MODIS models were taken from the MODIS ATBD (Remer, 2004). These parameters (indices of refraction, mode radius, standard deviation, etc.) are presented as functions of the optical depth. In the figures, the nine heavy diamonds represent MODIS model results for optical depths ranging from 0.1 to 5.0 for dust and to 3.0 for other models. For example, in the EAE *vs.* SSA plot, the dust models are represented by red diamonds for τ ranging from $\tau = 0.1$ (at the lower end of the red diamonds) to $\tau = 5$ (at the upper end).

The parameters for our evaluations of the OMI models are taken from the OMI ATBD and Curier (2008). The OMI models do not include variations in size distribution or index of refraction with wavelength except for desert dust. As shown in the plots below, the

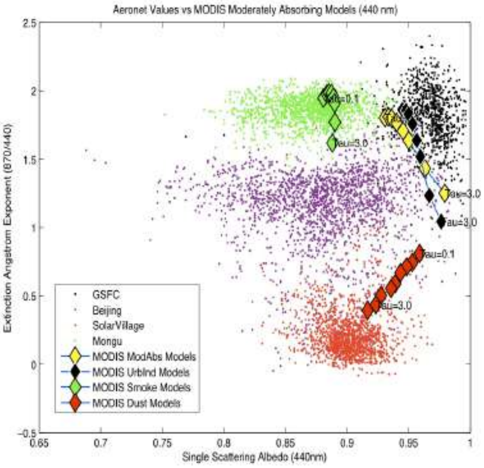

Figure 2. EAE *vs.* SSA for four characteristic aerosol types compared to MODIS models

agreement between OMI models and AERONET retrieved values is reasonable. We did not use all the OMI dust models, only those assuming spherical particles. The imaginary indices of refraction used in our calculations for dust were obtained by a large extrapolation from the UV values of Colarco (2002) and of Sinyuk (2002).

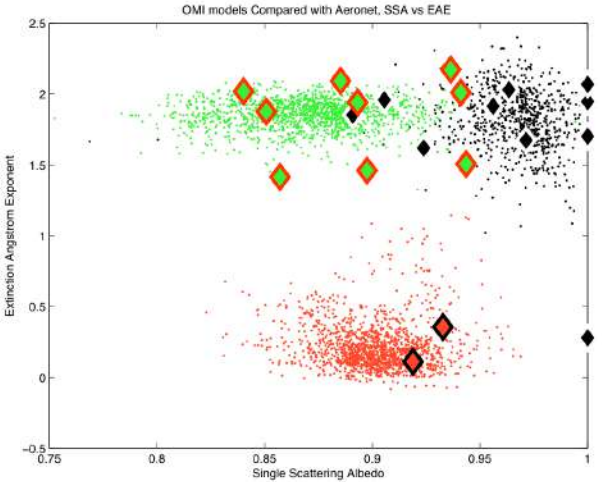

Figure 3. EAE *vs.* SSA for four characteristic aerosol types compared to OMI models.

The AERONET retrieved quantities are reported at 440, 630, 870 and 1020 nm. The CALIPSO models are for 532 and 1064 nm. Thus we can either interpolate and extrapolate the CALIPSO values to the AERONET wavelengths, or interpolate and extrapolate the AERONET retrieved values to the CALIPSO wavelengths. We chose to do the latter. The lack of agreement between the models and AERONET might be a consequence of these interpolations and extrapolations. Parameters for the CALIPSO models are from Omar (2009).

CONCLUSIONS

The Mahalanobis distance is a useful quantity for identifying aerosol types by determining its value from clusters of aerosols whose type is known with some degree of certainty. Using the Mahalanobis distance we can identify regions of parameter space for different types of aerosols and the boundaries between one type of aerosol and another. Our analysis demonstrated that Mexico City and Beijing aerosols are not similar to the Urban Industrial aerosols of Eastern USA and France. Mexico City and Beijing aerosols have properties lying between biomass burning and dust. Models used to identify aerosols from MODIS, CALIPSO and OMI are not always nearest (in terms of Mahalanobis distance) to the aerosol types they represent.

The Mahalanobis distances for the various satellite models compared to the aeronet clusters are given in the following tables.

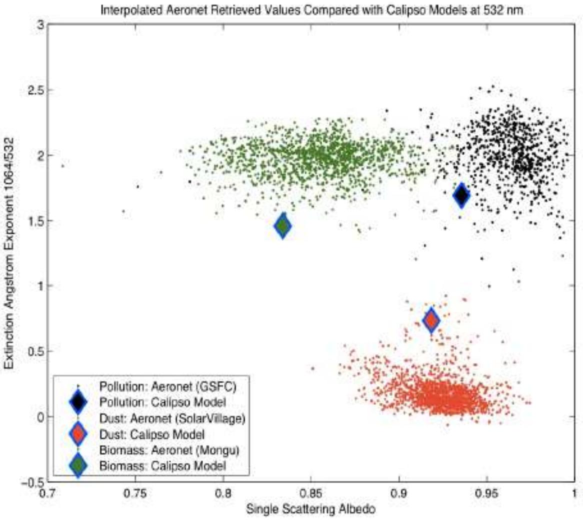

Figure 4. EAE *vs.* SSA for four characteristic aerosol types compared to CALIPSO models.

MODIS MODELS

	Urb/Ind	Mex	S.Am	Afr	Beij	Dust
Urb/Ind	2.67	2.29	2.03	4.75	2.71	5.87
Biomass	3.89	2.62	2.00	1.74	4.15	6.24
Dust	9.06	7.05	8.07	14.9	2.65	1.95

OMI MODELS (τ=0.5)

	Urb/Ind	Mex	S.Am	Afr	Beij	Dust
Pol1101	2.07	3.94	3.71	7.27	4.32	6.85
Biomass	2.80	3.80	2.99	4.07	5.76	7.07
Dust	16.5	15.6	14.7	28.2	6.51	3.46

CALIPSO MODELS

	Urb/Ind	Mex	S.Am	Afr	Beij	Dust
Urb/Ind	0.81	1.93	1.54	4.21	3.09	5.37
Biomass	5.65	2.75	3.36	4.74	2.45	5.40
Dust	8.62	4.76	5.55	10.1	3.09	2.55

REFERENCES

C. Cattrall *et al.,* J. Geophys.Res., doi:10.1029/2004 JD005124, 2005.

P. R. Colarco, O. B. Toon, O. Torres and P. Rasch, J. Geophys. Res., doi:10.1029/2001JK000903, 2002.

R. L. Currier *et al*., J. Geophys. Res., doi:10.1029/ 2007JD008738, 2008.

Dubovik (2002): O. Dubovik *et al*., J. Atmos. Sci, 59, 590, 2002.

Holben, B. *et al.* Rem. Sens. Env. 66, 1-16, 1998.

Omar, A. *et al*., Journal of Atmospheric and Oceanic Technology, doi:10.1175/2009 JTECHA1231.1, 2009.

L. Remer, D. Tanre and Y. Kaufman. Algorithm for Remote Sensing of Tropospheric Aerosols from MODIS. Collection 05. Product ID MOD04/MYD04

A. Sinyuk, O. Torres and O. Dubovik, Geophys. Res. Lett., doi:10.1029/2002GL016189

REVISTA BOLIVIANA DE FÍSICA 20s, 51-53, 2011
ISSN 1562-3823. INDEXADA EN: SCIELO, LATINDEX, PERIÓDICA

Aerosols measurements with a CIMEL CE-318 sun photometer in Camagüey, Cuba

René Estevan(1), Yasmine Benouna(2), Benjamín Torres(2), Juan. C. Antuña(1), Boris Barja(1), Carlos E. Hernández(1), Carlos Toledano(2), David Fuertes(2), Ramiro González(2), Victoria E. Cachorro(2), Ángel M. de Frutos(2)

(1)Grupo de Óptica Atmosférica de Camagüey, Centro Meteorológico de Camagüey, INSMET,
Camagüey, CUBA
Tel: +53 32 262397, E-mail: rene@cmw.insmet.cu
(2)Grupo de Óptica Atmosférica, Universidad de Valladolid,
Valladolid, ESPAÑA
Tel: +34983423270, E-mail: chiqui@goa.uva.es

SUMMARY

Aerosol Optical Depth (AOD) measurements, carried out with a sun photometer CIMEL CE-318, installed in Camagüey, Cuba, are reported. More than 700 days of measurements are analyzed, of them 400 days corresponds to level 2.0 of Aerosol Robotic Network (AERONET) dataset. These data cover from October 7, 2008 to April 22, 2010. To the level 1.5 corresponds more than 300 days from June 3, 2010 to June 17, 2011. The average value of AOD for the first period (level 2.0) is $\tau_a(500\text{ nm}) = 0.14$, while for the second $\tau_a(500\text{ nm}) = 0.17$, both cases with relatively high values. These AOD values confirm preliminary results about the Maritime Mixed characteristic for the Camagüey site. Several Saharan dust events are reported during the analyzed period.

Key words: CIMEL, sunphotometer, AOD, Saharan dust, aerosol.

INTRODUCTION

Many techniques and instruments has been developed for aerosols measurements, these includes both, passive and active methods. Camagüey, a former lidar site, have been using different techniques and instruments, including the lidar (Estevan *et al.*, 1998; Fonte and Antuña, 2011). Some years ago a sun photometer was installed as result of a scientific agreement between the Grupo de Óptica Atmosférica from Valladolid University, Spain (GOA-UVA) and the Grupo de Óptica Atmosférica de Camagüey (GOAC-INSMET) belonging to Meteorological Institute of Cuba. The instrument is operated as part of RIMA (Red Ibérica de Medición de Aerosoles). The first results of this joint research on tropospheric aerosols, with a preliminary characterization, were exposed by Estevan *et al*. (2011). From this study, the characteristic of a maritime mixed environment was evidenced, as well as, the similarity between our conditions, as island, and others islands in the Atlantic region (Smirnov *et al.*, 2002).

The international community interest about tropospheric aerosols and their influence over solar radiation, the environment and the human being, have also motivated our interest. An important topic in these studies is constituted by the Saharan dust, originated over the North African continent and dragged through the Atlantic Ocean until the Americas over the Trade winds (Prospero and Lamb, 2003). One of the most important interests is to determine the space-temporal characteristics of these events and magnitude of its influence over local conditions, as well as, the contribution of industrial polluted aerosols over background conditions.

MATERIALS AND METHODS

The instrument employed at the Camagüey site is a sun photometer CIMEL CE-318, an automatic multi-spectral sun tracking photometer, designed for very accurate sun measurements. Since the beginning of measurements, October 7, 2008, up to the present, four instruments were operated at Camagüey location. The RIMA- number of these instruments, as well as, the exploitation period, is shown in table 1.

Number	Dates	
	Initial	Final
#425	10/07/2009	05/28/2009
#353	06/04/2009	04/23/2010
#419	06/03/2010	06/17/2011
#424	07/21/2011	current

Table 1. List of instruments used at Camagüey site to the present, also both installation and removal dates listed.

The methods, measurement protocols, data processing, cloud-screening algorithm and inversion techniques employed by AERONET, to derive the aerosol optical properties for measurements, carried out with sun photometer, has been broadly reported (Dubovik and King, 2000; Smirnov *et al.*, 2000; Holben *et al.*, 2001). All dataset employed in the present study has been downloaded from the AERONET web site (AERONET). The variables used in present study are the Aerosol Optical Depth (AOD) and the Ångström Parameter (AP), commonly also named alpha parameter (α).

Datasets

For the all period, since October 10, 2008 to June 17, 2011 a total of 825 days of raw measurements (Level 1.0, according with the AERONET standards), were carried out. From these days, 779 reach the Level 1.5, the cloud screened level, representing the 94.4% of the all measurements days. The maximum stage of AERONET standard (Level 2.0) is the consequence of the instrument post calibration. A total of 401 days achieve this level, covering since October 7, 2008 to April 23, 2010. The photometers #425 and #353 are involved in this period, in which 462 days of raw measurements were carried out, from a total of 563 possible days, which it means a 82.1% of completion. A total of 435 days passed to the next AERONET level (cloud screened), this means that a 94.2% of the measurements days achieve the Level 1.5 while a 86.8% reach the Level 2.0.

In the present study we analyze the period corresponding with the Level 2.0, in the range of dates mentioned above. During this period two months are missing, April and May of 2009, because a failure in the motorized system of the first installed photometer and delays in the arrival of the replacement.

RESULTS

The monthly mean AOD at 500 nm (τ_a) and the corresponding standard deviation (σ^a) for the boarded period, are shown in figure 1. The maximum values for both, monthly mean and standard deviation, take place in July 2009. These maximums, τ_a = 0.26 and σ^a = ±0.14, respectively; are related with several episodes of Saharan dust arriving to the Caribbean region and to the Camagüey measurement site consequently. These aerosols are added to base "line" conditions (maritime and urban and industrial polluted aerosols). Saharan events, as well as, the analysis of 6 months (considered as background period), were accounted for in a preliminary study employing only values of AERONET Level 1.5 (Estevan *et al.*, 2011).

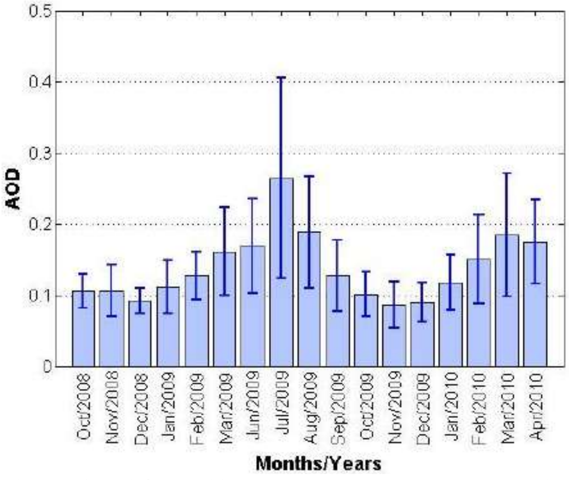

Figure 1. AOD (500 nm) monthly mean values with standard deviation (error lines), corresponding to all period of AERONET Level 2.0 dataset.

The AOD mean value for the actual analysis is τ_a = 0.14, a little higher than the preliminary study but, in this analysis the occurrence of Saharan dust events are included. Secondary maximums were found, mainly, within the summer season (June – August), although important values were found around March for both year 2009 and 2010, respectively. The minimum values of both, monthly means and standard deviation values occur during the winter season (approximately between October and January), when background conditions are established and not disturbances, by the presence of Saharan dust, take place.

The characteristic of maritime mixed conditions for the Camagüey site, obtained in a preliminary study (Estevan *et al.*, 2011), are corroborated in he present analysis. It is shown in the scattergram of AOD versus Ängstrom Parameter (AP, α) shown in figure 2. The values of AP over one are related with continental or urban-polluted aerosols. In the case of maritime aerosols, these can be located in the region with τ_a below to 0.15 and AP below one. On the other hand, presence of Saharan dust is also evident, within the analyzed period, owing to the high values of AOD (τ_a > 0.15) versus the small AP (α < 0.5), associated with the existence of large particles, process consistent with such phenomenon.

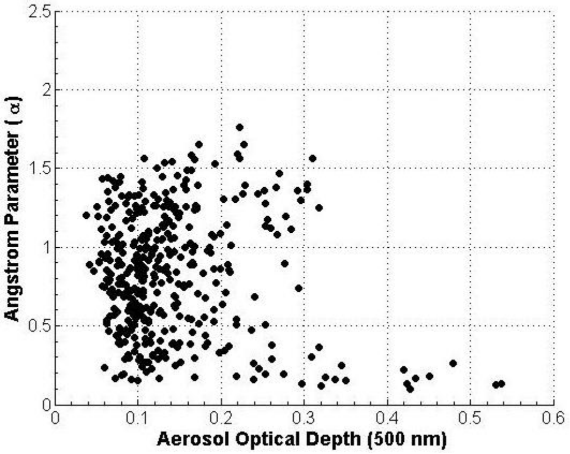

Figure 2. Scattergrams of daily means values of Ångström exponent (440-870nm) versus Aerosol Optical Depth (500nm).

Daily means values of AOD (500 nm) and the Ängstrom Parameter (440-870 nm), are show in figure 3, at the top and bottom, respectively. The disturbance caused by the Saharan dust over the background conditions can be appreciated clearly in this figure. The aerosol background conditions are characterized for this period at Camagüey site, by a mode value (τ_{am}) for AOD at 500 nm of τ_{am} = 0.1 with more than 40% of occurrence.

In the months around July 2009 it could be appreciated (at the top of figure 3) the load of Saharan dust aerosols, with a significant increase of AOD values, which disrupt the pattern of background conditions. Consequently, the effects of such aerosols are clearly registered in the AP behavior (bottom of same figure). With a values scattering, concentrated fundamentally between 0.5 > α < 1.5, characteristic of the maritime mixed environment, the presence of these north African aerosols cause a significant decrease of all AP values, bellow 0.5, during these months. The increase of AOD between February and April, 2010 is not related with Saharan dust events. In these cases the source of aerosols is related, mainly, with industrial and urban polluted air mass from the North American continent.

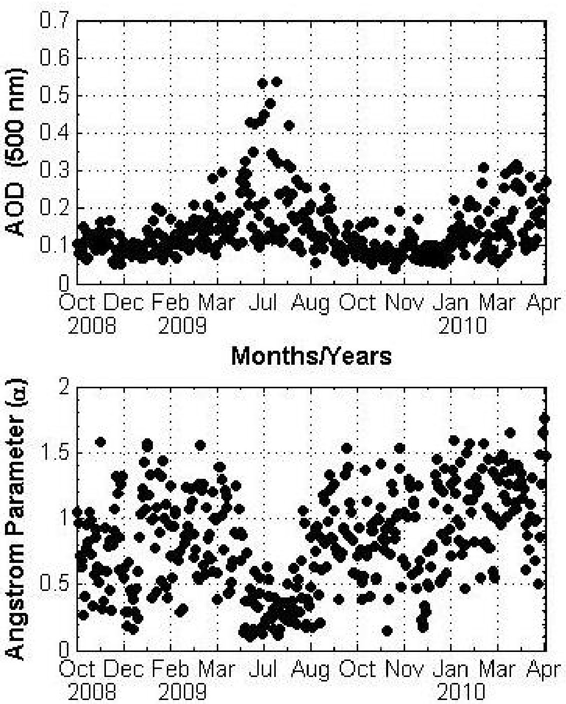

Figure 3. Daily mean values of Aerosol Optical Depth (top) at 500 nm and Angstrom Parameter (bottom) for 440-870 nm.

Practically one year cover the second period analyzed on the present study corresponding to Level 1.5, since June 3, 2010 to June 17, 2011. The AOD values, showed here, have a preliminary character, until that the post calibration procedure for the CIMEL #419 take place. The AOD mean value for this period is 0.17 while the maximum value of 2.36, because the presence of a strong Saharan dust event affecting our site in July 5, 2010, as could be appreciated in the figure 4, through MODIS Terra and Aqua daily level-3 data, produced with the Giovanni online data system.

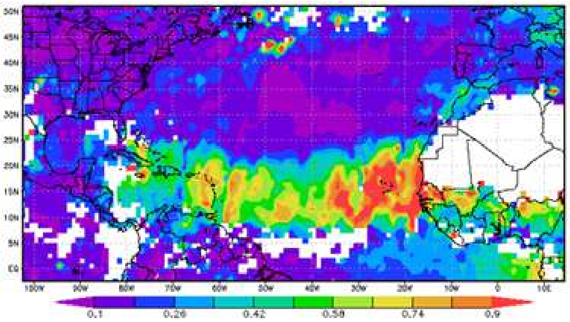

Figure 4. AOD at 550 nm from MODIS Terra and Aqua daily level-3 data, integrating days since July 1 to 6, 2010.

CONCLUSIONS

The preliminary results about the maritime mixed characteristics of Camagüey site, derived with the Level 1.5 of the AERONET data, has been corroborated in the present research. The AOD mean value ($\tau_a = 0.14$) is higher than the obtained in the previous study but in the same order of magnitude and the frequency distribution is centered at $\tau_{am} = 0.1$. The arrival of Saharan dust aerosol to Camagüey site during the summer season, is also clearly demonstrated with the Level 2.0 AERONET dataset, but in this case, with a AOD maximum value of 0.54, lower than reported in the previous preliminary results.

ACKNOWLEDGMENTS

Authors from GOAC-INSMET want to thank to GOA-UVA team by the support and logistic. To AERONET NASA our gratitude for including Camagüey site on the AERONET web site. To NASA GES DISC for providing data produced with the Giovanni online data system. This work has been supported by the Cuban National Climate Change Research Program and by the Collaboration Agreement between the Grupo de Óptica Atmosférica (GOA-UVA) and the Grupo de Óptica Atmosférica de Camagüey (GOAC-INSMET).

REFERENCES

AERONET, (http://aeronet.gsfc.nasa.gov)

Dubovik O., and M.D. King (2000), A flexible inversion algorithm for retrieval of aerosol optical properties from sun and sky radiance measurements, *J. Geophys. Res., 105*, D16, 20,673-20,696, doi:10.1029/2000JD 900282.

Estevan, R., R. Aroche, I. Pomares, S. Cervantes, and J. C. Antuña (1998), Aerosols, cirrus and temperature measurements with lidar at Camagüey, Cuba, *NASA/CP-1998-207671/PT1*, 173-176.

Estevan, R., J. C. Antuña, B. Barja, V. E. Cachorro, Á. M. de Frutos, A. Berjón, C. Toledano, B. Torres, R. Rodrígo, T. A. Hernández and C. E. Hernández (2011), Preliminary results of aerosols measurements with sun photometer at Camagüey, Cuba, *Opt. Pura Apl., 44* (1), 99-106.

Fonte, A. and J.C. Antuña, (2011) Caracterización del espesor óptico de banda ancha de los aerosoles troposféricos en Camagüey, Cuba, *Revista Cubana de Meteorología*, Vol. 17, No. 1, pp. 15-26.

Holben, B.N., D.Tanré, A. Smirnov, T.F. Eck, I. Slutsker, N. Abuhassan, W.W. Newcomb, J.S. Schafer, B Chatenet, F. Lavenu, Y.J. Kaufman, J. Vande Castle, A. Setzer, B. Markham, D. Clark, R. Frouin, R. Halthore, A. Karneli, N. T. O'Neill, C. Pietras, R.T. Pinker, K. Voss, G. Zibordi (2001), An emerging ground-based aerosol climatology: Aerosol Optical Depth from AERONET, *J. Geophys. Res.*, *106*, 12067-12097.

Prospero, J.M., and J.P. Lamb (2003), African droughts and dust transport to the Caribbean: Climate change and implications, *Science, 302*, 1024-1027.

Smirnov, A., B.N. Holben, T.F. E, O. Dobovick, I. Slutsker (2000), Cloud Screening and quality control algorithms for the AERONET database, *Rem. Sens. Env., 73*, 337-349.

Smirnov, A. B. N.Holben, Y.J.Kaufman, O. Dubovik, T.F.Eck, I. Slutsker, C. Pietras, and R.N. Halthore (2002), Optical Properties of Atmospheric Aerosol in Maritime Environments, J. Atmos. Sci., 59, 501–523.

REVISTA BOLIVIANA DE FÍSICA 20s, 54-56, 2011
ISSN 1562-3823. INDEXADA EN: SCIELO, LATINDEX, PERIÓDICA

THERMAL ANALYSIS OF LD PUMPED ND:Yag LASER SLAB AND FAILURE ANALYSIS

Dimitrios T. Kokkinos, Georgios Tzeremes
Opto-Electronics Section, ESA ESTEC
Keplerlaan 1, 2200AG, Noordwijk, NL
E-mail: ag_kokkinou@yahoo.com, Georgios.Tzeremes@esa.int
Errico Armandillo
Head of Opto-Electronics Section, ESA ESTEC
Keplerlaan 1, 2200AG, Noordwijk, NL
E-mail: Errico.Armandillo@esa.int

SUMMARY

As part of the R&D effort conducted within the Laser Laboratory of the European Space Agency, various simulation tools are being developed to understand and correct the thermal effects of side pumping an Nd:YAG slab with multiple individual High Power Laser Diodes. The scope of the present activity, which complements the work reported elsewhere at this workshop, is to emulate the thermal effects of a real amplifier and study the effects of various combinations of laser diode stacks with different characteristics, such as operational wavelength, temperature of operation, transmitted energy and pumping efficiency on the dynamic temperature distribution inside the slab. The motivation of this analysis is to work towards a simplification of the phenomena of heat generation and convection inside the crystal which account for the thermal lensing effect. Transient analysis is performed at different pump intensities under variable boundary conditions and the results are compared with experimental data as well as other software such as Zemax and LASCAD. Also the effects of laser diode stack failures are investigated and reported. The algorithm developed is based on the finite element method using tetrahedral elements for the adjustable meshing.

Key words: space Lidar, thermal simulation, thermal lensing effect, Nd:Yag laser slab

INTRODUCTION

A critical parameter of the overall instrument performance for lidar missions and especially for space applications is the performance of the laser during operation. The high power amplifier is the center of this study based on diode pumping at 808 nm. This theoretical research was based on an 8-diode pumped Nd:YAg slab under variable operation conditions. For MOPA Lidar missions the beam quality plays a critical role and the major objective of this study is to introduce the impact on the beam quality and shape when the laser slab is heated under different heat distributions [Siegman 1998]. The main reasons for the decrease of optical output quality (M^2, divergence) are the effects caused by the inhomogeneous thermal gradient inside the slab, such as thermal lensing and thermal induced birefrigerence [Mansell 2001]. Secondary objective of this study is the determination of the thermal behaviour of the slab in case of failure of one or several diodes. The modes of failure studied are instant failure and gradual degradation. The main phenomena that are affecting the thermal gradient inside the slab are the volumetric heat generation due to the absorption of the pumping light, the surface heating caused by convection through air and the cooling from the cold plates.

THE MODELED CONFIGURATION

The setup consists of a zig-zag Nd:Yag slab pumped by 8 diodes positioned as shown in Figure 1. The two operational configurations considered are the 74 Hz repetition rate of pumping by the 8 diodes simultaneously and a 37 Hz repetition rate of pumping by 4 diodes at a time, namely a 4+4configuration.These two configurations where the original configurations for the ATLID PU. The input current for each diode is set at 66 A for emission and 10 A ± TBD for self heating to maintain the preferred temperature for optimal wavelength emission for the case of 8 LD's illuminating the slab simultaneously. In the case of 4+4 configuration there are separate input currents for each diode stack side. The upper one has 82 A total input and the lower 80 A current input, from which 10 A are consumed for self heating. The crystal is also heated by the operational high power laser diodes through convection since air is inhabitant inside the amplifier and transfers heat through conductance to the slab [Wynne 1999]. For cooling two heat sink plates made from Copper with Indium interfaces were simulated. The temperature of the diode stacks are matched for optimum wavelength emission. The center wavelength of emission and the optical power are subject to the input current amplitude for each diode and the design electro-optical efficiency. The temperature of each diode will be highly affected by the input electrical current as known by literature.

THE HEATING EFFECTS

The major procedures that cause heating of the material are the diode heating, the heat conductivity of the material and the heat conductance in respect to the boundary surfaces. The diode pump intensity is absorbed inside the slab causing the molecules of ND to excite and occupy the 4F5/2 Energy level. The energy difference between the absorbed photon and the fluorescent photon increases the kinetic energy of the molecules and therefore the temperature of the material is increased. The heat distribution (Figure 1 left) is dependent on the exponential absorption in the penetration direction and is modelled according to [Lascad Tutorial]:

$$\exp(2r^2/w^2)$$

The second phenomenon of heating is due to convective air currents that transfer heat between the hotter diodes and the slab in cases where there are no vacuum conditions. This phenomenon follows the law of fluid convection Q=h*(T0-T), where T0 is the temperature at the diode stacks and T the temperature among the slabs surface and h is the conductance of air [Heat Transfer Textbook]. The reason that the heat is not homogeneous is that the temperature below the diode stacks is hotter than on other locations and coldest near the boundaries (Figure 2 right). The assumption of steady state operation leads to the constraint that the pumping intensity and frequency will not cause depletion of molecules residing in the ground Energy state and also that the spontaneous emission is neglectable. For calculating the temperature field that is governed by the phenomena of heating, conductance and internal material conductivity the heat PDE was solved with FEM using the appropriate tetrahedral elements. The size of the elements is determined by the waist size of the diode pump emission and has to be dx<beamwaist/2.

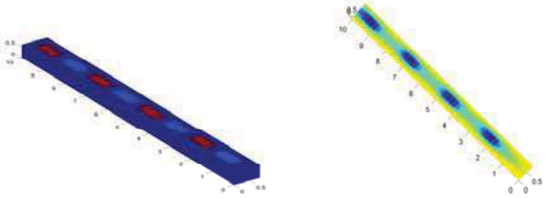

Figure 1: Left: The heat profile caused by diode pumping. Right: The convective heat exchanged with air in a.u.

RESULTS

To asses the impact of the boundary conditions and the diode temperature in the temperature distribution inside the slab some key cases where studied and reported. Secondarily two cases of diode failure where studied and compared with the other results. Figures 2 and 4 show the temperature distribution inside the slab under configuration 8 pumping for the cases of homogenous boundary conditions at 42 C and inhomogenous at 42 C and 45 C respectively. The two profiles show visible difference in the temperature distribution on the beam propagation path that is also visualised and compared in figure 3. In case 2 the wavefront is not exposed to symmetrical gradients at the edges as in case 1.

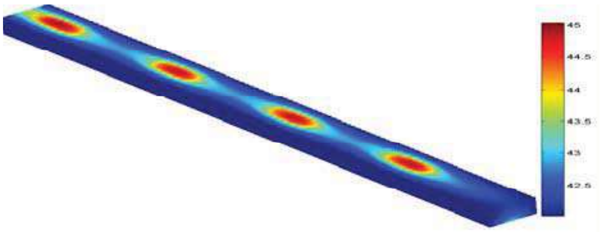

Figure 2: The temperature profile of the slab with homogenous boundary conditions

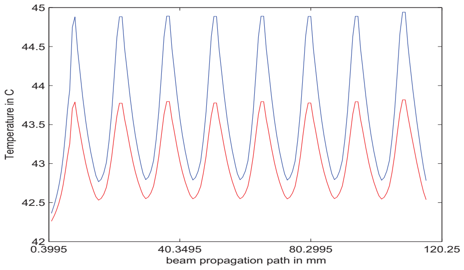

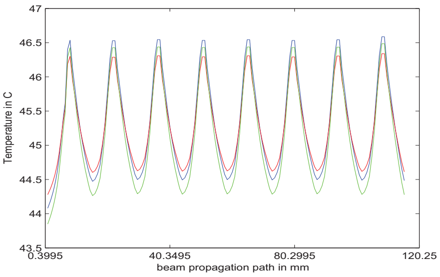

Figure 3: Left: Temperature distribution among the beam propagation path for the case of homogeneous boundary conditions. The blue line represents the temperature at the centre of the beam and the red represents the temperature at 2 mm distance from the centre along the x axis.
Right: Temperature distribution among the beam propagation path for the case of inhomogeneous boundary conditions. The blue line represents the temperature at the centre of the beam, the red represents the temperature at 1 mm distance from the centre along the x axis towards the hotter boundary and the green line represents the temperature at 1 mm distance from the centre towards the colder boundary.

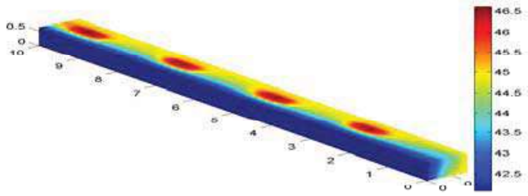

Figure 4: Temperature distribution inside slab using inhomogenous boundary conditions (42 C left boundary and 45C right boundary).

Further the process of heating through air convection was implemented for cases that diode operating temperature is considerably different than that of the slab and of course there is a heat convection carrier. This surface heating mechanism reduces the temperature gradient on the surface and the same time tends to make the local temperature distribution smoother [Koecher 1970]. This is illustrated in figure 5 for the whole body and in figure 6 (up) for the beam propagation path. It is visible that the peak temperature becomes marginally equal for all positions on the wavefront. The same cases were studied for the 4+4 configuration. Both configurations show identical response to the temperature changes of the environment apart from the fact that the temperature peaks differ according to the input current per side, which as mentioned defines the emitted optical power and the center wavelength and as a result also the absorption cross section (figure 6 down).

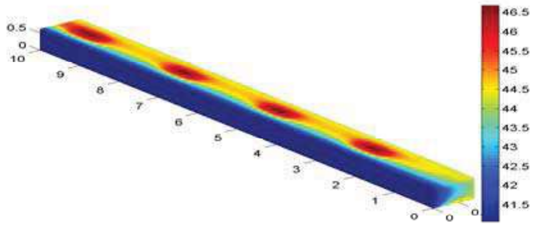

Figure 5: This case has also taken into consideration the heating from the hot air coming from the diodes. Although the maximum temperature has not changed a lot the temperature variation is different. As a consequence the hotspot temperature is close to the temperature of the rest of the upper surface but in the interior there is a larger temperature gradient. This is visualised in next figure were the upper peaks are at the same temperature but the lower peaks have a visible difference.

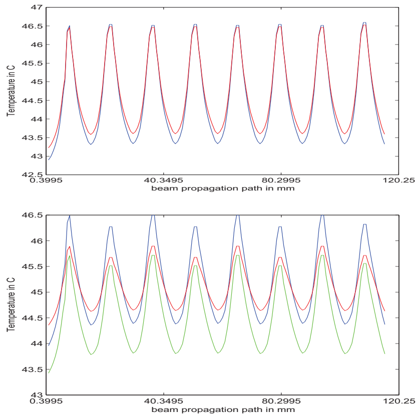

Figure 6: Left: Temperature distribution among the beam propagation path in case of inhomogeneous boundary conditions in 8 configuration. The blue line represents the temperature at the centre of the beam and the red represents the temperature at 1 mm distance from the centre along the x axis towards the hotter boundary. Right: Temperature distribution among the beam propagation path in case of inhomogeneous boundary conditions in 4+4 configuration. The blue line represents the temperature at the centre of the beam spot, the red represents the temperature at 1.3 mm distance from the centre along the x axis towards the hotter boundary and the green 1.3 mm towards the colder respectively.

Last to be presented are the thermal effects of diode failure. The first case with diode failure is under homogeneous boundary conditions. The 'dead' diode will stop emitting optical power and ideally will also not emit infrared or exchange heat with the environment. The effect of the temperature distribution on the beam propagation path can be observed in figure 7 up. In the second example of failure there are also non-homogeneous temperature gradient effects on the wavefront of the beam. At the region of the failed diode the temperature on one side of the wavefront (towards the hotter boundary) will be higher than that in the center (figure 7 down). An overview of the temperature results can be seen in table 1 and the temperature gradients on figure 8.

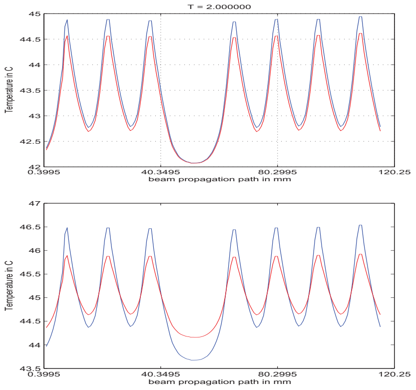

Figure 7: Left: Temperature distribution among the beam propagation path for the case of homogeneous boundary conditions with a failed diode. The blue line represents the temperature at the centre of the beam and the red represents the temperature at 2 mm distance from the centre along the x axis. Right: Temperature distribution among the beam propagation path for the case of inhomogeneous boundary conditions and a failed diode. The blue line represents the temperature at the centre of the beam, the red represents the temperature at 1 mm distance from the centre along the x axis towards the hotter boundary.

	Case 1	Case 2	Case 3	Case 4 (4+4)	Failure 1	Failure 2
Boundary 1	42	42	42	42	42	42
Boundary 2	42	43.5	45	45	42	45
Max Temp	44.9	46	46.8	46.8	44.7	46.5

Table 1: summary results from the cases presented

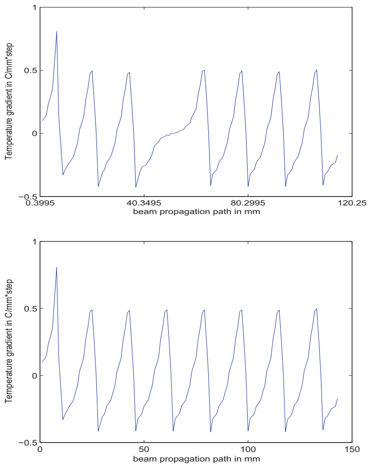

Figure 8: Up: Temperature gradient distribution among the beam propagation path for the case of homogeneous boundary conditions with a failed diode. Down: Temperature gradient distribution among the beam propagation path for the case of inhomogeneous boundary conditions.

CONCLUSIONS

The key achievement of this work is the modelling of the temperature fluctuation along the beam propagation path in regard to the boundary conditions, the material properties of the pu slab and the performance of the diodes. Some interesting cases applicable to the purpose of this work were studied and compared. The inhomogenous boundary conditions cause non uniform temperature gradient in the wavefront propagation path, which affects the beam quality of the output beam. The convective currents can partially counter this effect for the surface area of the slab. For the failure analysed cases the conditions on the boundaries play again an important role, since as illustrated they can significantly change the ratio of the temperature in the center of the wavefront to the temperature on the edge of the wavefront.

REFERENCES

"Evaluating the effect of transmissive optic thermal lensing on laser beam quality with a Shack-Hartmann wave-front sensor", Justin D. Mansell et al., Applied Optics/vol. 40.No.3, 2001

"Thermal lensing in a ND:Yag Laser Rod", W Koecher, Applied Optics/ vol. 9,No. 11, 1970

"How to measure Laser Beam Quality", AE Siegman et al, Stanford University issue, 1998

"Thermal coefficients of the expansion and refractive index in YAG", Rosalind Wynne et al, Applied Optics/ Vol 38, No 15, 199

"The FEA code of Lascad", Konrad Altman, Lascad tutorial

"A Heat Transfer Handbook", John Lienhard, Phlogistron Press, Cambridge

First LIDAR system in Concepción, Chile

A. Silva, E. Montilla, C. Saavedra, R. Hernández
Center for Optics and Photonics (CEFOP), Universidad de Concepción, Chile

Center for Optics and Photonics

Abstract

A single wavelength tropospheric LIDAR has been developed by the Optical Instrumentation and Teledetection Technologies Division at Center for Optics and Photonics (CEFOP), to study the evolution of the atmospheric boundary layer and vertical profiles of aerosol optical properties over Concepcion city (36º 47´S, 73º7' W, 12m amsl). The system is located in the Transportable Integrated Geodetic Observatory (TIGO) of the University of Concepción and it has been set up on transportable facility to carry up field measurement campaigns at any place across the country. The LIDAR system has been developed to measure with range resolution of 7.5 m; this system uses a wavelength of 532 nm and has a 310 mJ/pulse. In this work, a complete system description of the first LIDAR are presented.

Introduction

Concepcion is located in the south of Chile and it is the capital of Bio Bio region. The city hosts several industries, including fishing, steel and plastic companies. Taking into account all of this industrial activity and its location near the coast, the concentration measurement of pollutants over this area is very important. Currently, there are no such measurements in the city.

To understand the temporal evolution, transport and impact of the urban pollution, i.e., urban and industrial aerosols, the Center for Optics and Photonics (CEFOP) has implemented a elastic LIDAR system.

Experimental Site

The LIDAR system is housed in a transportable station located at Transportable Integrated Geodetic Observatory (TIGO) Consortium formed by the University of Concepcion, the Military Geographic Institute of Chile (IGM) and the Federal Agency for Cartography and Geodesy of Germany (BKG). TIGO is located at University of Concepcion (180m amsl). This is the cleanest place in the city, for it is located far away from direct emissions. The observatory host measurement systems such as Very Long Baseline Interferometry (VLBI), a Satellite Laser Ranging (SLR), Global Navigation Satellite Systems (GNSS), Gravimeter and Meteorological Sensors.

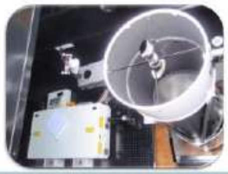

Lidar Set-up

Emission	**Laser**	• 532 nm with pulses of 320 mJ. • Pulse duration: 7 ns. • Beam divergence: 0.5 mrad • Pulse repetition rate: 10 Hz
	Beam Expander	• Magnification: 5x
	Periscope	• Elliptical mirror with 2,5" of minor axis.

Reception	**Output Mirror**	• Elliptical mirror with 2,5" of minor axis.
	Telescope	• Newtonian telescope. • Primary mirror: 16" diameter. • Focal length: 72". • FOV: 1,2".
	Reception Optics	• Spatial filter • Interference filter centered at 532nm (±3nm)

Data Acquisition	**Photosensor**	• 300-900nm • Rise time: 1,3ns • Gain: 10e5-10e6
	Transient Recorder	• 20MHz A/D, 12 bit • Spatial resolution: 7,5m • Maximum high detection: 61km • Two memories banks: photocounting and analog detection

Data Processing

Input data	Pre-processing	Algorithm	Output data

• Constant parameters
• Atmospheric data
  • Pressure
  • Temperature
  • Density
  • Humidity
• Molecular data
	• Acquisition
	  • Reading raw files
	  • Data cleaning
	• Range corrected signal
		• Data analysis involves the inversion method:
		Klett inversion
			• Visualization of time series data registered
			  • Boundary layer determination
			• Retrieve extinction and backscattering coefficients

Laser characterization

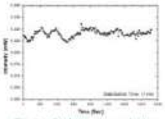

Fig.1: Stabilization of the laser output power.

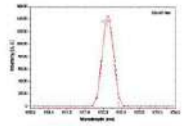

Fig.2: Nd:YAG laser spectra.

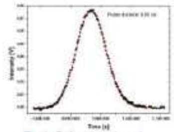

Fig.3: Pulse duration of Nd:YAG laser.

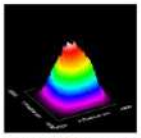

Fig.4: Nd:YAG laser profile.

Discussion and Outlooks

After spending the past few months building the new LIDAR laboratory at University of Concepcion, our current work consists of the calibration and alignment of the complete system to obtain the first LIDAR signals.

To improve the information retrieved by the system, a multi-wavelength LIDAR for measurement of non-elastic scattering will be implemented in the next stage. Finally, the Raman LIDAR will be set up to measure local water vapor content

References

Argall P.S., Siga R.J., *«Encyclopedia of Atmospheric Sciences»*, Elsevier Science, 2002, p.869-889.
Carvacho O.F, Trzepla-Nabaglo K., Ashbaugh L.L., Flocchini R.G., Melin P., Celis J. (2004), *«Technical Note: Elemental composition of springtime aerosol in Chillán, Chile»*, Atmospheric Environment 38, 5349-5352.
Eichinger W.E., Holder H.E., Cooper D.I., Hipps L.E., Knight R., Kustas W.P., Nichols J., and Prueger J. H. (2005), *«LIDAR measurement of boundary layer evolution to determine sensible heat fluxes»*, J. Hydrometeorology – Special Section, 840–854.
Klett, J.D *«Lidar calibration and extinction coefficients»*, Applied Optics, 22, Nº24,1983.
Kovalev, V., W. Eichinger, *«Elastic Lidar: Theory, Practice and Analysis Methods»*, Ed. John Wiley & Sons, 2004".
Measure Raymond, *«Laser Remote Sensing: Fundamentals and Applications»*, John Wiley & Sons, 1984.

Acknowledgements

The authors would like to thank to TIGO staff for their technical support. This work was supported by grant PFB0824. A. Silva acknowledges CONICYT for the scholarship, and Dr. Whiteman for the VI WLMLA travel grant .

REVISTA BOLIVIANA DE FÍSICA 20s, 58, 2011
ISSN 1562-3823. INDEXADA EN: SCIELO, LATINDEX, PERIÓDICA

Development of a Tropospheric Lidar for Observations of the Planetary Boundary Layer above Medellín, Colombia

NISPERUZA Daniel[1], BASTIDAS Alvaro[2]

1,2 Physics School, Universidad Nacional de Colombia, Medellín Calle 59A No 63-20, Colombia)
Author e-mail: djnisperuzat@unal.edu.co – dnisper6@gmail.com

Abstract

In the Universidad Nacional de Colombia, Sede Medellín, the Lasers and Spectroscopy Group (GLEO) has been designed and manufactured a tropospheric LIDAR station based on a pulsed Nd:YAG laser operating at 532-nm wavelength. The main scientific objective has been to evaluate the vertical structure of the Planetary Boundary Layer (PBL) in urban sites of Medellín-Colombia, South America, (Longitude 75 º 34 '05" West, Latitude 6 º 13' 55" North), using suspended aerosols as tracers of the atmospheric motion. This paper report the design, manufactures and performance of an elastic lidar system, which was operated under varying air pollution and meteorological conditions and the observations presented here were performed in early 2010, over the metropolitan area of Medellín, city included in the Andean region of Colombia.

Key words: Tropospheric LIDAR; Planetary Boundary Layer – PBL.

Experimental Set-up

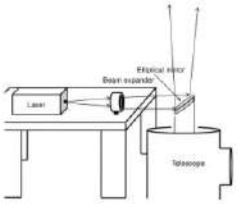

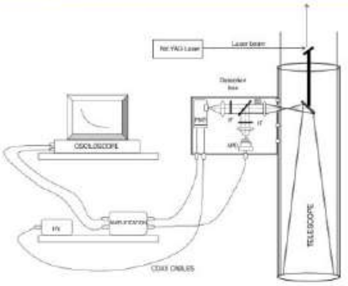

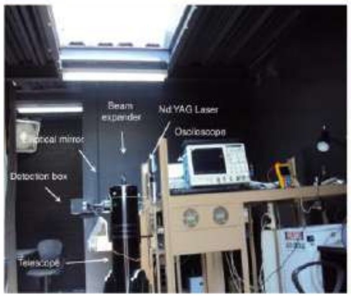

The LIDAR system, operated in the city of Medellin, has a coaxial configuration with two wavelengths backscatter system pointing vertically to the zenith. The light source is a pulsed Nd:YAG laser, donated by the IFAC, Italy, operating, by means of frequency doubling using KD*P crystals, are obtained two wavelengths simultaneously (1064 and 532 nm). The maximum energy per pulse is 400 mJ at 1064 nm and 200 mJ at 532 nm respectively. The emitted laser beam to the atmosphere, it has been expanded from 6 to 12 mm of diameter, reducing the divergence to 0.3 mrad. The emitter system is a modified Newtonian telescope of 1.2 m focal length.

Results

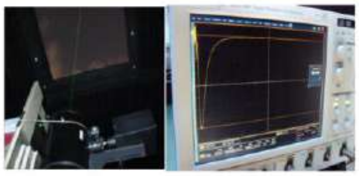

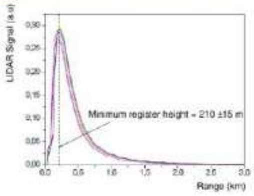

Clear sky measurements were made in the full week from 22 to 30 January 2010, during three daily periods of approximately 30 min each, at 10:00 Am, 12:00 to 15:00 (local time). The profiles of signal lidar are shown in the figure above.

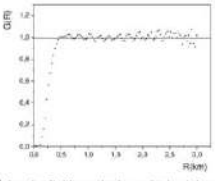

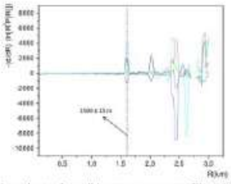

By applying the Doh's method we obtained the geometrical form factor from lidar measurement. The PBL height above Medellin city was retrieved applying the logarithm derivate method.

Currently

AERONET –Colombia Project: Remote siensing of tropical aerosols at Medellin Colombia

- Detection of the topical aerosol events with different instruments/methods.
- Characterization of physical, radiative and optical properties of tropical aerosols.
- Determination of single scattering albedo and aerosols radiative forcing with inversion procedures.

Conclusions

With our tropospheric backscattering lidar we have been able to monitor the height of the PBL and its diurnal evolution. Different meteorological conditions resulted into different patterns. The altitude of the PBL over the city of Medellin was found to be above 1.5 km range, and inferring that the aerosol load has a high variability.
In the future, more complete lidar aerosol datasets will be available, and the correlation between lidar and radiosonde data, with the purposes of determining the boundaries of the aerosol layers and the vertical structure of the atmosphere, with both lidar channels (1064 nm and 532 nm), over Medellin city.

References

- STULL R. B., An Introduction to Boundary Layer Meteorology (Kluwer Academic Publishers, Dordrecht) 1988.
- PELON J. and MEGIE G., Ozone monitoring in the troposphere and the lower stratosphere: evaluation and operation of a ground-based lidar station, J. Geophys. Res., 87 (1982) 4947-4955.
- MILTON M., WOODS P. T., JOLLIFFE B., SWANN N. and MCILVEEN MC., Measurements of Toluene and other Aromatic Hydrocarbons by Differential-absorption LIDAR in the near-ultraviolet, Appl. Phys. B, 55 (1992) 41-45.
- SANG WHOE DHO, YOUNG JE PARK, and HONK JIN KONG, Experimental determination of a geometric form factor in a lidar equation for an inhomogeneous atmosphere, APPLIED OPTICS y Vol. 36, No. 24 y 20 August 1997.
- FERDINANDO DE TOMASI, MARIA RITA PERRONE, PBL and dust layer seasonal evolution by lidar and radiosounding measurements over a peninsular site, Elsevier doi:10.1016/j.atmosres.2005.06.010.
- V. KOVALEV, W. EICHINGER, Elastic Lidar: Theory, Practice, and Analysis Methods, Ed. John Wiley & Sons, 2004.

REVISTA BOLIVIANA DE FÍSICA 20s, 59, 2011
ISSN 1562-3823. INDEXADA EN: SCIELO, LATINDEX, PERIÓDICA

Study on aerosol properties over Madrid (Spain) by multiple instrumentation during SPALI10 lidar campaign

F. Molero[1*], M. Sicard[2], F. Navas-Guzmán[3], J. Preißler[4], A. J. Fernandez[1], S. Tomas[2], M.J. Granados[3], F. Wagner[4], M. Pujadas[1], A. Comeron[2], L. Alados-Arboledas[3], J.L. Guerrero-Rascado[3,4], D. Lange[2], J.A. Bravo-Aranda[3], D. Kumar[2], J. Giner[2], C. Muñoz[2], F. Rocadenbosch[2]

[1]Centro de Investigaciones Energéticas, Medioambientales y Tecnológicas (CIEMAT), Avda Complutense, 22. Madrid, 28040. Spain. [2]Department of Signal Theory and Comunications, Remote Sensing Lab., Universitat Politècnica de Catalunya/Institut d'Estudis Espacials de Catalunya, Barcelona, Spain. [3]Andalusian Center for Environmental Research (CEAMA). University of Granada – Autonomous Goverment of Andalusia, Av. del Mediterráneo s/n, 18071, Granada, Spain. [4]Évora Geophysics Centre (CGE), University of Évora, Rua Romão Ramalho 59, 7000, Évora, Portugal

Introduction:

Understanding the effect of aerosols upon radiative forcing requires information about vertical profiles [Clarke, 2010]. Lidar techniques represent a powerful tool for studies of the vertical structure of aerosols. During the SPAin Lidar Intercomparison 2010 (SPALI10) campaign, several multiwavelength Raman lidar systems measured simultaneously in order to assess their performances. Multiwavelength lidars can provide relevant vertically-resolved information on aerosol optical properties [Müller, 2001]. The products provided by the lidar systems were compared with ancillary data. At ground level, aerosol size distribution were continuously monitored between 15 nm and 20 µm by merging two particle counters. Additionally, the column-integrated characterization of the atmospheric aerosol was performed by means of a sun photometer. The extensive dataset obtained during SPALI10 field campaign enables to compare ground-level in-situ measurements with remote sensing techniques. Several relevant features shown in the comparison of the results obtained by the different instruments are discussed in this work.

Experimental deployment:

- SPALINET [Sicard, 2009] & EARLINET [Bösenberg, 2003] lidar instruments from Madrid (ma), Barcelona (ba), Granada (gr), Évora (ev) and Potenza (po) were compared in order to assess their performance. Profiles from Madrid station were inverted to provide backscatter profiles at 355, 532 & 1064 nm
- Automatic sun tracking photometer Cimel CE-318-4 provided aerosol optical depth (AOD) at several wavelengths and column-integrated size distributions among other products
- Aerosol size distribution at ground level was obtained by merging data from a TSI SMPS 3936 (14.6 – 661 nm) and a GRIMM 1108 (0.3 – 20 µm).

Figure 1. Lidar stations and ancillary instrumentation that participated in the SPALI10 campaign at CIEMAT site, Madrid (Spain) (40.45ºN, 3.73ºW, 663m asl) from 18 Oct to 5 Nov 2010

Results and discussion:

The aim of the campaign was to compare simultaneous lidar range-corrected signals (RCS, raw signals multiplied by the square power of the range) from several SPALINET network stations (Madrid, Granada, Barcelona and Évora) with a EARLINET reference lidar system from Potenza in order to assess their performances measuring the same atmosphere during the same time periods.

Although all network stations routinely perform internal quality checks, an intercomparison campaign was compulsory since some stations recently upgraded the systems (ma & ba) and other joined the network (ev).

In order to avoid differences in the raw signal processing by different data analysis, all systems delivered the several-hours datasets of successive one minute averaged signals without any preprocessing to a common data base server, where all signals were then preprocessed by a Single Calculus Chain (SCC) software. The SCC pre-processing calculus module performs trigger delay shift, dead time correction, atmospheric background and dark measurement subtraction, range correction, vertical smoothing up to a fixed height resolution, cloud screening, handling of signals measured at angle different from zenith and, after selection of a comparison period, the time integration of appropriate lidar signals over the selected time window.

Fig. 2 shows the comparison of the elastic wavelengths' RCS averaged nearly one hour for 3 November nighttime session, at the end of the campaign after several system optimizations. Signals have been truncated at the full-overlap height, that changes from station to station. All systems correctly resembles the reference profile with deviations smaller than 20% for 355 and 532 nm and slightly larger for 1064 nm.

Madrid did not measure at 355 nm and Évora at 1064 nm due to changes in the system configuration. The large noise of Granada 1064 nm signal was due to a partial masking of the telescope in order to correct a problem related to the position of the pinhole.

The results of the campaign can be considered satisfactory as the campaign allowed to check the performances of the systems and when they were not fully satisfactory, the reasons of the failure were understood and a way to solve them could be defined.

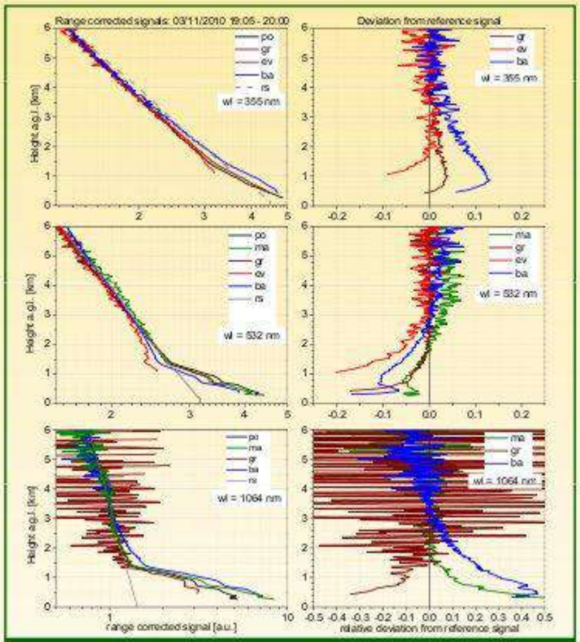

Figure 2: Comparison of RCS obtained on 3 Nov evening. Left panels: RCS for the Potenza (po, Black), Madrid (ma, Green), Granada (gr, Wine), Évora (ev, Red) and Barcelona (ba, Blue) lidar systems. Right panels: Deviations from the reference system (po).

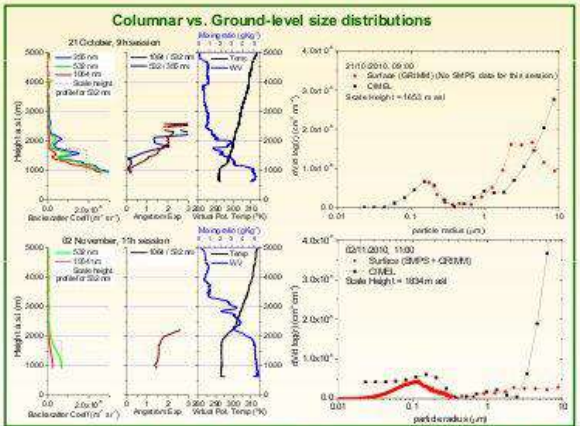
Columnar vs. Ground-level size distributions

Figure 3.- Comparison of volume size distributions. Top panels correspond to the 21 Oct, 9h session and bottom panels to the 2 Nov, 11h session. Left panels: Height-resolved aerosol properties from lidar measurements (backscatter coefficient, backscatter-related Angström exponent (BAE)) and radiosounding parameters (virtual potential temperature and water vapor mixing ratio). Right panels: Semilog plot of the columnar volume size distribution calculated from CIMEL (black squares) and converted from ground-level measurements (red circles) by means of the scale height (H) provided by lidar system.

Figure 3 shows the column-integrated volume size distributions provided by the sun-photometer (sensitive to the aerosol optical properties of the entire column) and derived from ground-level in-situ measurements (which may not be representative of the distributed aerosol in the entire boundary layer).

The distributions obtained by in-situ instrumentation at surface level (in $\mu m^3\ cm^{-3}$) are converted into columnar distribution ($cm^3\ cm^{-2}$) for comparison with sun-photometer retrievals, by means of a scale height that corresponds to the altitude where the area of a vertically-constant extinction profile is equal to the retrieved AOD for a given lidar profile, with a lowest level extinction value calculated to maximize the overlap between both profiles.

The observed size distributions are typically bimodal, with the first modal radius between <0.015 and 0.4 µm, and the second between 0.5 and >10 µm. Between these modal values generally there is a minimum (inflection point), corresponding to a radius of about 0.4 µm.

Top panels (21 Oct): Non-homogeneous atmosphere, with two aerosol layers above the mixing layer. BAE values indicate different aerosol properties on those layers. The presence of lofted layers with a different type of aerosol, although with very low backscattering values, might influence the comparison.

Bottom panels (2 Nov): Well-developed mixing layer up to 2 km, constant virtual potential temperature and mixing ratio and roughly constant aerosol backscatter coefficient. A nearly constant BAE value of 1.5 is obtained, indicating same type of aerosol in the entire mixing layer.

Conclusions:

During the SPALI10 lidar intercomparison campaign at Madrid, the products provided by multiwavelength lidar systems were compared with ancillary instrumentation data, such as the aerosol size distribution at ground level and the column-integrated characterization of the atmospheric aerosol. A comparison of columnar versus ground-level aerosol size distribution was performed by converting ground-level in-situ measurements into column-integrated values using the retrieved scale height values provided by lidar profiles. Both techniques yield bimodal aerosol size distribution, with an inflection point around 0.4 µm, with better agreement in the size range between 0.2 and 2 µm, where the inversion algorithm for sun-photometer data is more reliable. The vertically-resolved aerosol optical properties at three wavelengths provide information about the type of aerosol present in the different layers observed. Height-resolved backscatter-related Ångström exponents provided by lidar profiles indicate different aerosol properties in aloft layers in some cases. The stratified atmosphere detected by the lidar system might explain some of the discrepancies observed in the size distributions. Further investigations are ongoing to obtain relevant vertically-resolved aerosol optical properties from multiwavelength Raman lidar systems.

References:

Bösenberg, J. et al., "EARLINET: A European Aerosol Research Lidar Network to establish an aerosol climatology", Rep. 348, Max-Planck Inst. Für Meteorol., Hamburg, Germany, (2003)
Clarke, A. & Kapustin, V. "Hemispheric aerosol vertical profiles: Anthropogenig impacts on optical depth and cloud nuclei", Science, 329 1488-1492 (2010)
Müller, D. et al., "Comprehensive particle characterization from 3-wavelength Raman-lidar observations: Case study", *Appl. Opt.*, 40(27), 4863–4869 (2001)
Sicard, M. et al., "Aerosol Lidar Intercomparison in the framework of SPALINET–The Spanish Lidar Network" *IEEE Trans. Geosci Rem Sens* 47 (10) 3547-3559 (2009)

ACKNOWLEDGMENTS

The work was supported by the European Union under the EARLINET-ASOS project (contract nº 025991 (RICA)), by the MICINN (Spanish Ministry of Science and Innovation) under the project CGL2010-17777 and Complementary Actions CGL2008-01330-E/CLI & CGL2010-09225-E and by the ESA-CEOS Intercalibration of Ground-Based Spectrometers and Lidars (CEOS-IC-PR01) project.

VI Workshop on lidar measurements in Latin America 2011.

*Contact e-mail = f.molero@ciemat.es

GOBIERNO DE ESPAÑA
MINISTERIO DE CIENCIA E INNOVACIÓN

Ciemat
Centro de Investigaciones Energéticas, Medioambientales y Tecnológicas

Aerosols measurements with a CIMEL CE-318 sun photometer in Camagüey, Cuba

R. ESTEVAN, J. C. ANTUÑA, B. BARJA, C. E. HERNÁNDEZ
Grupo de Óptica Atmosférica de Camagüey (GOAC), CMPC – INSMET, Cuba

Y. BENOUNA, B. TORRES, C. TOLEDANO, D. FUERTES, R. GONZÁLEZ, V. E. CACHORRO, A. M. de FRUTOS
Grupo de Óptica Atmosférica (GOA-UVA), Universidad de Valladolid, España

Summary

Aerosol Optical Depth (AOD) measurements, carried out with a sun photometer CIMEL CE-318, installed in Camagüey, Cuba, are reported. More than 700 days of measurements are analyzed, of them 401 days corresponds to Level 2.0 of Aerosol Robotic Network (AERONET) dataset. These data cover from October 7, 2008 to April 22, 2010. To the Level 1.5 corresponds more than 300 days from June 3, 2010 to June 17, 2011. The average value of AOD for the first period (Level 2.0) is τ_a(500 nm) = 0.14, while for the second τ_a(500 nm) = 0.17, both cases with relatively high values. These AOD values confirm preliminary results about the Maritime Mixed characteristic for the Camagüey site. Several Saharan dust events are reported during the analyzed period.

Numbers	Dates	
	Initial	Final
#425	10/07/2009	05/28/2009
#353	06/04/2009	04/23/2010
#419	06/03/2010	06/17/2011
#424	07/21/2011	current

Instruments used at the Camagüey site.

A total of 825 days of raw measurements (Level 1.0) were carried out since October 10, 2008 to June 17, 2011; 779 days reach the Level 1.5, the cloud screened level, representing the 94.4%. A total of 401 days achieve The AERONET Level 2.0, covering since October 7, 2008 to April 23, 2010.

The photometers #425 and #353 are involved in this period, in which 462 days of raw measurements were carried out, from a total of 563 possible days, which it means a 82.1% of completion. A total of 435 days passed to the next AERONET level (cloud screened), this means that a 94.2% of the measurements days achieve the Level 1.5 while a 86.8% reach the Level 2.0.

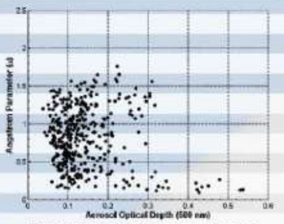

Scattergram of daily means values of Angstrom Parameter (AP, 40-870nm) versus Aerosol Optical Depth (500nm).

The characteristic of maritime mixed conditions for the Camagüey site has been corroborated in he present study. The values of AP over 1 are related with continental or urban-polluted aerosols. Maritime aerosols, can be located in the region with τ_a below to 0.15 and AP below 1. Presence of Saharan dust is also evident within the analyzed period, owing to the high values of AOD ($\tau_a > 0.15$) versus the small AP ($\alpha < 0.5$), associated with the existence of large particles, process consistent with such phenomenon.

The background aerosol are characterized for this period at Camagüey site by a mean value of 0.14 and mode value (τ_{am}) for AOD at 500 nm of τ_{am} = 0.1 with more than 40% of occurrence. Around July 2009 a significant increase of AOD values, disrupt the pattern of background conditions. The effects of such aerosols are clearly registered in the AP behavior.

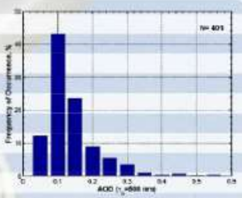

Frequency of Occurrence (%) of AOD values at 500 nm.

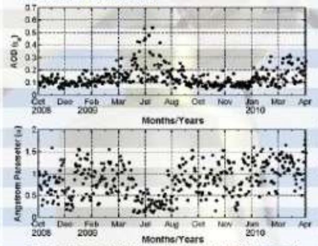

Daily mean of both, AOD (top) at 500 nm and Angstrom Parameter (bottom) to 440-870 nm.

Aerosols with AP values between 0.5 and 1.5, are characteristic of maritime mixed environment. The presence of North African aerosols cause a significant decrease of all AP values, bellow 0.5. The increase of AOD between February and April, 2010 is not related with Saharan dust events. In these cases the source of aerosols is related with industrial and urban polluted air mass from the North American continent fundamentally.

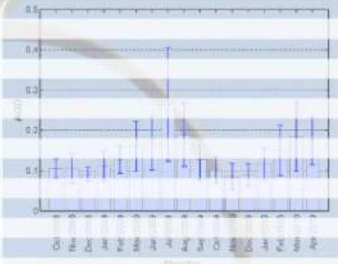

AOD (500 nm) monthly mean values (τ_a) with standard deviation (σ^a), corresponding to all period of AERONET Level 2.0 dataset.

Maximum values τ_a = 0.26 and σ^a = 0.14 took place in July 2009, related with several episodes of Saharan dust over Caribbean region and to the Camagüey site consequently.

The AOD mean value for all period is τ_a = 0.14, a little higher than a preliminary study (*Estevan et al., 2011*), because the Saharan dust events are included in the present analysis. Exists secondary maximums within the summer season (June – August), although important values were found around March for both year 2009 and 2010. The minimum values occur during the winter season (approximately between October and January), when background conditions are established and not disturbances, by the presence of Saharan dust, take place.

Several Saharan dust events took place during July 2009, with a maximum daily mean AOD of 0.696 on July 6. This value did not suffer change respect to the obtained in a previous preliminary study.

Time evolution of AOD (500 nm) raw data, AERONET Level 2.0 corresponding to July 2009.

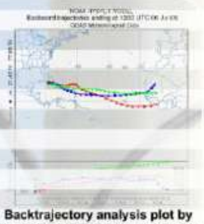

Backtrajectory analysis plot by the HYSPLIT (NOAA) model with GDAS dataset at 12 UTC, July 6, 2009, run backward up to 7 days.

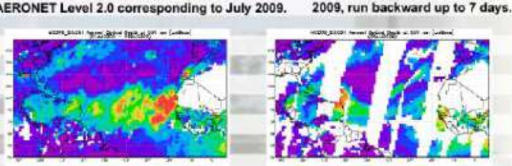

AOD at 550 nm from MODIS Terra and Aqua daily level-3 data (from Giovanni online system), integrating days since July 1 to 6, 2009 (left) and July 6, 2009 (right).

Practically one year cover the period corresponding to Level 1.5, since June 3, 2010 to June 17, 2011. AOD values have a preliminary character, until the post calibration procedure for the CIMEL #419. The mean AOD value for this period is 0.17 while the maximum value of 2.36, is because the presence of a strong Saharan dust event affecting our site in July 5, 2010, (image right) produced with the Giovanni project.

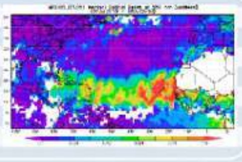

Conclusions

The preliminary results about the maritime mixed characteristics of Camagüey site, derived with the Level 1.5 of the AERONET data, has been corroborated. The AOD mean value (τ_a = 0.14) is higher than obtained in the previous study with frequency distribution centered at τ_{am} = 0.1. The arrival of Saharan dust aerosol to Camagüey site, is also demonstrated with the Level 2.0 AERONET dataset, but in this case, with a AOD maximum value of 0.54 for daily means.

Acknowledgments

Authors from GOAC-INSMET want to thank to GOA-UVA team by the support and logistic. To AERONET NASA our gratitude for including Camagüey site on the AERONET web site. To NASA GES DISC for providing data produced with the Giovanni online data system. This work has been supported by the Cuban National Climate Change Research Program and by the Collaboration Agreement between the Grupo de Óptica Atmosférica (GOA-UVA) and the Grupo de Óptica Atmosférica de Camagüey (GOAC-INSMET).

VI Workshop on Lidar Measurements in Latin America, La Paz, Bolivia.
September 26 - October 1, 2011

REVISTA BOLIVIANA DE FÍSICA 20s, 61, 2011
ISSN 1562-3823. INDEXADA EN: SCIELO, LATINDEX, PERIÓDICA

Characterization of the local boundary layer from measurements on anomalously polluted days

Forno R., Andrade M., Velarde F., Lazcano O., Zabala P., Vargas M.
Laboratorio de Física de la Atmósfera, Universidad Mayor de San Andrés, La Paz - Bolivia

Introduction

An old tradition in Bolivia states that the 23rd of June (San Juan's eve) is the coldest night of the year. Bonfires and fireworks were common as a way of keeping people warm on that night. However, with the growth of population these bonfires became a health issue and now many of these activities have been forbidden. In spite of this, people continue making fires and using fireworks during San Juan. Because of this particulate matter and smog are common around that day (although at much lower frequency than before). The Laboratory of Atmospheric Physics (LFA) has been monitoring gases and particulate matter the last few years in order to characterize events like this. Now with the new Lidar system, implemented with collaboration of ESA and NASA, new information is available for this purpose.

Goals of this study

To characterize the behavior of the boundary layer by monitoring particulate matter trapped within the boundary layer using the LIDAR system at Cota-Cota, La Paz, Bolivia (16.5°S, 68.1°W, 3420 masl)).

Rationale

By the end of June there are usually few biomass burning events in Bolivia. Typically the maximum of biomass burning fires occur around September. As a consequence, there is almost no smoke over the Andes during June. In this sense, particles produced during San Juan make monitoring the behavior of the boundary layer and pollution produced by the city without "interference" of free tropospheric smoke produced by biomass burning in the lowlands.

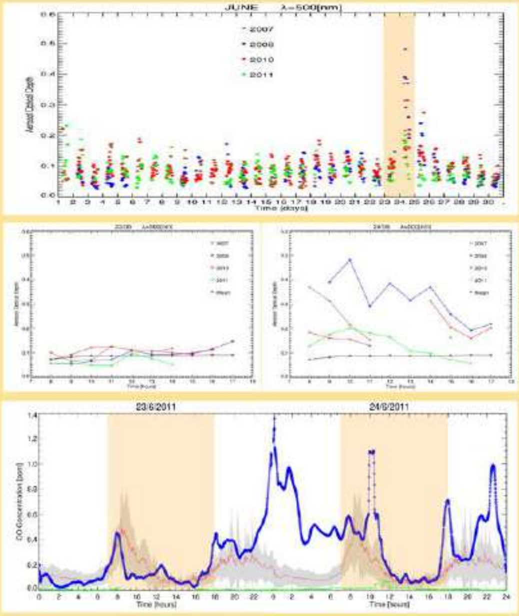

Figure 1: a) Daily mean of aerosol optical depth (AOD) at 500 nm for June 2011 as measured by sunphotometer CIMEL 133 located on the roof of the LFA. b) AOD at 500 nm for the 23 and 24 of June for years 2007 to 2011. c) Carbon monoxide concentration measured by Horiba analyzers during the 23 and 24 of June, 2011 at Cota-Cota (blue line) and Chacaltaya (green line). The daily "climatological" values of CO concentration are shown in the background. The shaded region indicates variability observed from May to July of 2011. The mean value is depicted by the weak red line.

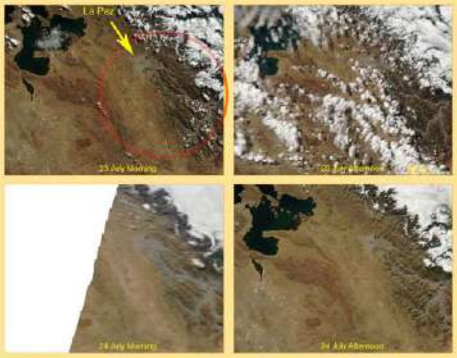

Figure 2: True color images taken by MODIS instruments aboard of Terra (overpass around 10:30 am) and Aqua (overpass 1:30 pm) satellites. The images show the metropolitan area of La Paz (yellow arrow) between the morning of the 23 and the afternoon of the 24. Smoke is visible on the morning of 24, after San Juan´s eve.

Measurements

The LFA has been monitoring particulate matter and surface gases during the last San Juan events through:

- A LIDAR system at Cota-Cota. Measurements are obtained at some specfic times. The Lidar is usually operated on a fixed weekly schedule.
- A cascade impactor (MOUDI). Samples were collected at specific times (data still in process).
- A CIMEL sunphotometer. Data is collected during the day.
- Two HORIBA carbon monoxide analyzers, one at Chacaltaya and one at Cota-Cota. Both instruments measure data continuously.

Results and conclusions

Events like San Juan, when a large injection of particulate matter from the surface occurs over a relatively short period of time, are useful for analyzing the behavior of the boundary layer.

Although the sunphotometer measurements indicate that the amount of particulate matter this year (2011) was lower than previous years, the behavior of the boundary layer at Cota-Cota, is clearly observed.

Measurements of the CIMEL sunphotometer as well as of the CO analyzer show an anomalous increase of both particles and CO during the 23rd and 24th of June.

During the evening of 23 of June there is a stable residual layer with smoke trapped below 1.5 Km and evidence of buoyancy oscillation.

During the morning of 24 of June there is evidence of convective development and increase of the boundary layer height with time.

These Lidar profiles have permitted us to understand better the influence of locally produced aerosols and the boundary layer structure. It also demonstrates the general capability to study aerosols such as those also produced by biomass burning and transported by winds. This will be the focus of upcoming measurements.

Acknowledgements

We are thankful to Dr. Errico Armadillo from ESA and Dr. David Whiteman from NASA for their strong support to our laboratory. Part of the funding for this project was provided by the Swedish International Cooperation Agency (SIDA) through the Departamento de Investigación, Postgrado e Interacción Social (DIPGIS) of Universidad Mayor de San Andrés (UMSA).

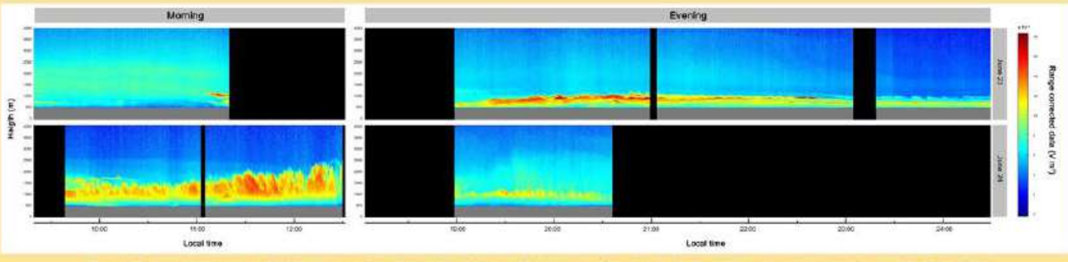

Figure 3: Data collected by the LIDAR system located at Cota-Cota (3420 masl) during June 23 and June 24. The Lidar system characteristics are: Nd:YAG QUANTEL-BRIO laser at 532nm, Newtonian telescope (primary mirror ϕ =250 mm y f= 700mm), PMT Hamamatsu H6573, Tektronix TDS350 osciloscope - PCI-GPIB.

Laboratorio de Física de la Atmósfera - IIF - UMSA www.lfabolivia.org

Misión

La Revista Boliviana de Física (RBF) es el órgano oficial de la Sociedad Boliviana de Física (SOBOFI) y se publica semestralmente en forma conjunta con el Instituto de Investigaciones Físicas y la Carrera de Física de la Universidad Mayor de San Andrés (IIF-UMSA).

La RBF busca difundir la producción científica de la comunidad de físicos y profesionales de ciencias afines, especialmente dentro de Iberoamérica.

Secciones

Los artículos, revisiones y colaboraciones se distribuyen en las siguientes secciones:

A. **Artículos**: Son trabajos que presentan material nuevo y original. Para su publicación, deben ser revisados y aprobados por árbitros del Consejo Editorial. Los artículos deberán tener un resumen no mayor a 200 palabras y secciones de Introducción, Métodos y Procedimientos, Resultados y/o Discusión de datos, Conclusiones y Referencias.

B. **Contribuciones y Revisiones**: Estos trabajos no presentan, necesariamente, material original sino que definen la posición del (de los) autor(es) sobre un determinado tópico de debate (en el caso de Contribuciones) o bien, son una revisión de temas conocidos en algún área de la física (en el caso de Revisiones). Las contribuciones deberán estar orientadas hacia la difusión de algún problema o debate interpretativo. Las revisiones estarán orientadas a exponer temas de trascendencia para el desarrollo de las ciencias relacionadas con la física, o exponer en forma didáctica algún tema que los autores encuentren que no ha sido tratado en forma adecuada en la literatura asequible en lengua castellana.

C. **Memorias de la Reunión Anual de la SOBOFI u otras reuniones de física**: Esta sección reúne los resúmenes de los trabajos presentados durante la última Reunión Nacional Anual de la SOBOFI o de otras reuniones científicas importantes sobre física.

D. **Enseñanza de la Física**: Esta sección está dedicada a artículos que tratan sobre problemas relacionados a la enseñanza de la física o a la promoción del estudio de la física entre los jóvenes estudiantes. Se incorporan regularmente en esta sección los exámenes de las Olimpiadas de Física y las Olimpiadas de Astronomía y Astrofísica. Las contribuciones a esta sección son seleccionadas exclusivamente por el Comité Editorial.

E. **Historia**: Esta sección se dedica a la conmemoración de hechos importantes en la historia de la Física Boliviana e Iberoamericana. De igual manera, se orienta a la recopilación de publicaciones relacionadas a la física que, por su importancia histórica, merecen ser nuevamente publicadas.

Instrucciones para los autores

Los trabajos enviados para su publicación deberán estar escritos preferentemente en castellano. Trabajos escritos en inglés podrán ser aceptados por el Comité Editorial y, pasado el proceso de aceptación, serán traducidos al castellano para su publicación en la RBF.

Los autores deberán enviar sus trabajos preferentemente en los formatos LaTeX 2_ε, *MS Word*, o *sólo texto* (con extensiones *.tex*, *.doc* y *.txt*, respectivamente), ya sea mediante una copia en dispositivo magnético o bien por correo electrónico. En este caso, deberán incluir una carátula donde se especifique el título del trabajo, los nombres de los autores, las direcciones (postal y/o electrónica) y el resumen del trabajo. Además, las figuras, tablas y notas de pie de página contenidas deberán estar indicadas en el texto, debidamente numeradas y referenciadas. Las figuras deberán tener una resolución razonable a fin de que puedan ser vistas con suficiente claridad por el lector.

Los artículos científicos serán revisados por el Comité Editorial y posteriormente por un par de árbitros anónimos quienes dan el veredicto sobre si el artículo es aceptado o no.

La comunicación de los autores con los árbitros se realiza únicamente a través del editor encargado del área.

Los trabajos y consultas sobre la RBF deberán enviarse a las direcciones del Comité Editorial indicadas arriba.

Conflicto de intereses: Los autores que envíen artículos para su publicación en la RBF admiten que no tienen conflicto de intereses en relación a los trabajos realizados y presentados.


VI WORKSHOP ON LIDAR MEASUREMENTS IN LATIN AMERICA
WORKSHOP ON LIDAR MEASUREMENTS IN LATIN AMERICA
& Training Course on Lidar
entel
uniendo

NÚMERO ESPECIAL DEDICADO A
LAS PRESENTACIONES Y POSTERS DEL
“VI WORKSHOP ON LIDAR MEASUREMENTS IN LATIN AMERICA”

Secciones

Los artículos en este número especial se distribuyen en las siguientes secciones:

I. **Presentaciones**: Estos trabajos muestran, en resumen, las presentaciones mostradas por los expositores del workshop.

II. **Posters**: En esta sección se presentan los posters presentados por los expositores, en la sessión de posters en el workshop.

Formato de este número

Los trabajos presentados en este número están escritos tanto en ingles como en castellano según las especificaciones del comité organizador.

Los artículos correspondientes a las presentaciones tienen como máximo tres páginas y fueron escritos con diferentes formatos y tipos de letra, según la preferencia de cada autor.

Los trabajos de la sección de posters tienen solo una página y tienen diferentes formatos, según la preferencia de cada autor.

Los trabajos fueron revisados por el Comité Organizador.

Conflicto de intereses: Los autores que envíen artículos para su publicación en la RBF admiten que no tienen conflicto de intereses en relación a los trabajos realizados y presentados.